creative commons

COMMONS DEED

저작자표시-비영리-변경금지 **2.0** 대한민국

이용자는 아래의 조건을 따르는 경우에 한하여 자유롭게

- 이 저작물을 복제, 배포, 전송, 전시, 공연 및 방송할 수 있습니다.

다음과 같은 조건을 따라야 합니다:

저작자표시. 귀하는 원저작자를 표시하여야 합니다.

비영리. 귀하는 이 저작물을 영리 목적으로 이용할 수 없습니다.

변경금지. 귀하는 이 저작물을 개작, 변형 또는 가공할 수 없습니다.

- 귀하는, 이 저작물의 재이용이나 배포의 경우, 이 저작물에 적용된 이용허락조건을 명확하게 나타내어야 합니다.
- 저작권자로부터 별도의 허가를 받으면 이러한 조건들은 적용되지 않습니다.

저작권법에 따른 이용자의 권리는 위의 내용에 의하여 영향을 받지 않습니다.

이것은 이용허락규약(Legal Code)을 이해하기 쉽게 요약한 것입니다.

Disclaimer

dCollection

이학박사 학위논문

A Study on Temporal Variability, Kinematics of AGN and Relation with Gamma-ray Flares

활동성 은하핵의 시간에 따른 변화 모습과 운동학, 감마선 방출과의 관계

2022년 8월

서울대학교 대학원

물리·천문학부 천문학전공

이 태 석

A Study on Temporal Variability, Kinematics of AGN and Relation with Gamma-ray Flares

활동성 은하핵의 시간에 따른 변화 모습과 운동학, 감마선 방출과의 관계

지도교수 Sascha Trippe

이 논문을 이학박사 학위논문으로 제출함
2022년 07월

서울대학교 대학원
물리·천문학부 천문학전공
이 태 석

이 태 석 의 이학박사 학위논문을 인준함
2022년 08월

위 원 장	박 용 선
부 위 원 장	Sascha Trippe
위 원	황 호 성
위 원	손 봉 원
위 원	변 도 영

A Study on Temporal Variability, Kinematics of AGN and Relation with Gamma-ray Flares

by

Taeseok Lee
(tlee@astro.snu.ac.kr)

A dissertation submitted in partial fulfillment of the requirements for
the degree of

Doctor of Philosophy

in
Astronomy

in
Astronomy Program
Department of Physics and Astronomy
Seoul National University

Committee:

Professor	Yong-Sun Park
Professor	Sascha Trippe
Professor	Ho Seong Hwang
Professor	Bong Won Sohn
Professor	Do-Young Byun

ABSTRACT

Active Galactic Nuclei (AGN) are amazing astronomical objects. They are the most powerful, brightest and persistent sources of electromagnetic radiation. AGN have jet structures extending to mega-parsec scale and have a power source of a supermassive black hole (SMBH) residing in their hearts. Their relativistic jets show apparent superluminal motions induced by Doppler boosting effect and radiate mostly non-thermal synchrotron emission and inverse Compton radiation. Though the formation of the jet, collimation and acceleration process have been well studied, there are still fundamental questions which need answers. There are various tools to investigate the AGN characteristics as temporal variability study, kinematics, polarization analysis, multi-wavelength analysis, at many times they are combined to assess more robust answers.

AGN are known for irregular variability on all time scales, down to intra-day variability with relative variations of a few percent within minutes to hours. On such short timescales, unexplored territory still exists. In the first step, we present the results of AGN single-dish fast photometry performed with the Korean VLBI Network (KVN). Observations were done in a “anti-correlated” mode using two antennas, with always at least one antenna pointing at the target. This resulted in an effective time resolution of less than three minutes. We used all four KVN frequencies, 22, 43, 86, and 129 GHz, in order to trace spectral variability. We were able to derive high-quality light curves for 3C 111, 3C 454.3, and BL Lacertae at 22 and 43 GHz, and for 3C 279 at 86 GHz, between May 2012 and April 2013. We performed a detailed statistical analysis in order to assess the levels of variability and the corresponding upper limits. We found upper limits on flux variability ranging from $\sim 1.6\%$ to $\sim 7.6\%$. The upper limits on the derived brightness temperatures exceed the inverse Compton limit by three to six orders of magnitude. From our results, plus comparison with data obtained by the University of Michigan Radio Astronomy Observatory, we conclude that we have not detected source-intrinsic variability which would have to occur at sub-percent levels.

Secondly, we present the results of 1.5-year-long KVN observations of a BL Lac object, 1749+096 from February 2018 to June 2019. In the radio band ranging from KVN 22 GHz to ALMA band 3 100 GHz, the radio lightcurves show concurrent flares with the characteristic time scale of 1.4 yrs. 1749+096 went through a gamma-ray outburst in mid-2016 and had one of few follow-up flares at the end of 2017. Studying the correlation between the ALMA band 3 and Fermi-LAT lightcurves, we found that gamma-ray flare precedes the radio flare by 1.26 year. From the archival VLBA 43 GHz observation data, small jet feature toward northern direction can be seen. We could identify and track four jet components and estimated apparent jet speeds are 4, 4.8, 5.8, and 9.7 c. The VLBA kinematics analysis revealed an evidence of an interaction between newly ejected jet component and the stationary component at the time of gamma-ray flare at the end of 2017. We also probed the physical information of synchrotron self-absorption region during the flaring activity. From the radio flare rising timescale, we derived the variability brightness temperature, $4.7 \times 10^{10} K$, Doppler factor, 1.3, and the emission region size, 0.024 mas. Associated magnetic field strength of 0.11 G was obtained assuming synchrotron cooling of the region.

Following step is to analyze how the jet motion varies on the sky and what physical mechanisms lie behind. We present the results of jet kinematics of the flat spectrum radio quasar (FSRQ) 4C +21.35 using time resolved KaVA very long baseline interferometry array radio maps obtained from September 2014 to July 2016. During two out of three observing campaigns, observations were performed bi-weekly at 22 and 43 GHz quasi-simultaneously. At 22 GHz, we identified three jet components near the core with apparent speeds up to $(14.4 \pm 2.1)c$. The timing of the ejection of a new component detected in 2016 is consistent with a gamma-ray flare occurred in November 2014. At 43 GHz, we found four inner jet (<3 mas) components with speeds from $(3.5 \pm 1.4)c$ to $(6.8 \pm 1.5)c$. Jet component speeds tend to be higher with increasing distances from the core. We compared our data with archival Very Long Baseline Array (VLBA) data from the Boston University (BU) 43 GHz and the Monitoring Of Jets in Active galactic nuclei with VLBA Experiments (MOJAVE) 15.4 GHz monitoring programs. Whereas MOJAVE data and our data are in good agreement, jet speeds obtained from the BU Program data in the same time period are about twice as high as the ones we obtain from the KaVA data. The discrepancy at 43 GHz indicates that radio arrays with different angular resolution identify and trace different jet features even when the data are obtained at the same frequency and at the same time. The flux densities of jet components decay exponentially, in agreement with a synchrotron cooling time scale of ∼1 year. Using known electron Lorentz factor values (∼9,000), we estimate the magnetic field strength to be ∼1–3 μT. When adopting a jet viewing angle of 5°, the intrinsic jet speed is of order 0.99c.

Keywords: galaxies: active – galaxies: jets – radio continuum: galaxies – individual: 4C +21.35, PKS 1749+096 – techniques: interferometric

Student Number: 2012-20399

Contents

Abstract **i**

List of Figures **ix**

List of Tables **xv**

1 Introduction **1**

1.1 Active Galactic Nuclei 1

1.1.1 AGN overview 1

1.1.2 Relativistic Jets 6

1.1.3 High Energy Radiation 11

1.2 Very Long Basline Interferometry 13

1.3 Thesis outline 16

2 A Search for Intra-day Variability with KVN **19**

2.1 Abstract 19

2.2 Introduction 20

2.3 Observations 21

2.4 Data Analysis 23

2.5 Results 29

2.5.1 3C 279 29

2.5.2 3C 111 31

2.5.3 3C 454.3 35

2.5.4 BL Lac 35

2.6 Discussion 35

2.7 Summary and Conclusions 38

3 The Radio and Gamma-ray Connection in the Jets of PKS 1749+096 41

3.1 Abstract 41

3.2 Introduction 42

3.3 Observations and Data Analysis 44

3.3.1 KVN 44

3.3.2 ALMA 45

3.3.3 Fermi-LAT 45

3.3.4 VLBA 43 GHz 46

3.4 Results 46

3.4.1 Multi-Wavelength Lightcurves 46

3.4.2 Correlation bewteen Radio and Gamma-rays 52

3.4.3 Synchrotron Self-Absorption region 52

3.4.4 VLBA 43 GHz 56

3.5 Discussion 58

4 Jet Kinematics of the Quasar 4C +21.35 from KaVA Observations 63

4.1 Abstract 63

4.2 Introduction 64

4.3 Observations and Data Analysis 67

4.4 Results 70

4.4.1 KaVA at 22 GHz 70

4.4.2 KaVA at 43 GHz 74

4.4.3 Intrinsic Jet Speeds and Doppler factors 78

4.4.4 Flux Evolution and Synchrotron Cooling 78

4.4.5 Spectral Index Maps 80

4.5 Discussion 82

4.5.1 Boston University Program Data 82
4.5.2 BU Program Data with KaVA ***uv***-coverage 82
4.5.3 MOJAVE Data 84
4.5.4 The 10-mas-blob 85
4.6 Conclusion 87

5 Conclusion **91**

Bibliography **94**

요 약 **103**

감사의 글 **107**

List of Figures

1.1 Schematic view of AGN structure. The classification according to the viewing angles and radio loudness are also illustrated. Colors are added and the original image by Fermi, NASA. 2

1.2 Blazar sequence by Ghisellini et al. (2017). *Top :* SEDs of FSRQs show stronger Compton dominance as luminosities become larger. *Middle :* SEDs of BL Lacs show smaller peak frequencies as the luminosity increases. *Bottom :* Combined SEDs of FSRQs and BL Lacs show more prominent features. 5

1.3 Simple jet formation mechanism with a spinning object and attached magnetic field lines. (a) A sphere is attached to the ambient medium with a poloidal field line. (b) Magnetic field lines are wound up like a coil. (c) The spring-like magnetic coil pushes the medium upward. (d) The jet is formed with the toroidal field loops. Original image by Davis & Tchekhovskoy (2020). 6

1.4 M87 radio jet observed with different VLBI arrays, frequencies at various scales. The smallest scale shows the black hole shadow, the intermediate scales show collimated jet features, the largest scale shows termination of the jet. Original image by ESO. 9

1.5 Schematic picture of Very Long Baseline Interferometry. A pair of antennas receiving signals from a source. A signal delay of τ and projected baseline, d, is indicated. Original image from Mahmoud et al. (2011). . . 14

1.6 uv-coverage of the KVN and VERA joint array (KaVA). Different colors correspond to the different array or observation frequencies. Image from Hada et al. (2020). 15

2.1 The 86-GHz lightcurve (left) and power spectrum (right) of 3C 279 as observed in May 2012. The dashed line in the power spectrum indicates the mean value; the sampling frequency is in units of s^{-1}. Note that the axis scales are logarithmic, leading to downward spikes being more pronounced that upward deviations. 29

2.2 The 22-GHz lightcurves and power spectra of 3C 111 observed during three consecutive days in November 2012. Dashed lines in the power spectra indicate mean values; the sampling frequency is in units of s^{-1}. 30

2.3 The 22-GHz lightcurves (left panels) and Scargle periodogram (right panels) of 3C 111 observed at three consecutive days (from top to bottom) in February 2013. The sampling frequency of the periodograms is in units of s^{-1}. 31

2.4 The 43-GHz lightcurves (left panels) and Scargle periodogram (right panels) of 3C 111 observed at three consecutive days (from top to bottom) in February 2013. The sampling frequency of the periodograms is in units of s^{-1}. 32

2.5 *Top left:* UMRAO lightcurve of 3C 111 observed at 14.5 GHz from 1975 to 2005. *Top right:* The associated power spectrum; the dashed line indicates a theoretical random walk noise spectrum ($A_f \propto f^{\beta}$, $\beta = -2$). *Center and bottom:* The Scargle periodogram from UMRAO data (black curve) along with periodograms from KVN 22-GHz data (gray curves) for three consecutive days in November 2012. The sampling frequency of the periodograms is in units of day^{-1}. Again, the dashed lines indicate theoretical random walk noise laws. 33

2.6 Lightcurves (left panels) and Scargle periodograms (right panels) of 3C 454.3 observed in April 2013. *Top:* 22 GHz. *Bottom:* 43 GHz. The sampling frequency of the periodograms is in units of s^{-1}. 34

2.7 Lightcurves (left panels) and power spectra (right panels) of BL Lacertae observed in April 2013. *Top:* 22 GHz. *Bottom:* 43 GHz. The sampling frequency of the periodograms is in units of s^{-1}. 34

3.1 KVN images of 1749+096 at 22,43,86,94 GHz. The contour levels start at three times the rms noise value and increase in steps of 2. 47

3.2 KVN lightcurves of 1749+096 at 22, 43, 86, 94, 139 GHz from top to bottom. 48

3.3 Spectral indices obtained from the four frequencies of KVN. 49

3.4 ALMA lightcurves of 1749+096 at band 3,6,7 from the top to bottom. . 50

3.5 Fermi-LAT lightcurves of 1749+096 from 2009 to 2020. *Top :* Adaptive binning, *Bottom :* Weekly binning. Image by Fermi-LAT. 50

3.6 The interpolated weekly binned Fermi-LAT lightcurve from 2017 to 2021. 51

3.7 The DCF result between the Fermi-LAT and ALMA band 3 light curves. the brown and orange dashed lines indicate 99 and 95 % significance level respectively. The DCF peak is located at the time lag of -1.26 yr. 51

3.8 ALMA band3 and Fermi-LAT correlation. The Pearson's correlation coefficient is 0.5. Note that Fermi-LAT light curve was shifted by the value of correlated time delay, 1.26 yr for the analysis. 53

3.9 Spectral energy distribution at six epochs of KVN quasi-simultaneous data. Curved power-law function is fitted for turnover frequency. The obtained turnover frequencies range from 25.1 to 32.2 GHz. 55

3.10 VLBA 43 GHz image in January 2020. The contour levels start at three times the rms noise value and increase in steps of 2. 56

3.11 The kinematics result of VLBA 10-year-long observations by Weaver et al. (2022). A1 is the stationary component and B3 is the fastest component with apparent speed of 25c. B10 component is identified and tracked as J1 component in our work. Figure from Weaver et al. (2022). 57

3.12 The radial distances of the jet components from VLBA observation. Four jet components, J1-J4, are identified and tracked. The light blue ones are the jet components which couldn't be traced. The jet components S and C denote the stationary and core component at the bottom. 58

3.13 VLBA 43 GHz flux density variation of the stationary component, S, at 0.2 mas. The flux density started to rise after the beginning of 2018 gamma-ray flaring activity 60

4.1 A 22 GHz KaVA image of 4C +21.35 in February 2016. The contour levels start at three times the rms noise value (0.64 mJy/beam), and increase in steps of 2. Circles labeled with letters mark identified jet components, the grey crossed circle is excluded from our analysis. The lightblue ellipse on the bottom left illustrates the CLEAN beam (1.27 mas × 1.13 mas). 71

4.2 Jet kinematics derived from the 22 GHz KaVA maps. *Top panel:* Projected distance from the core as a function of time for all five jet components, separately for the outer components in the 10-mas blob (upper diagram) and the three inner jet components (lower diagram). *Bottom panel:* Apparent speeds of the three inner components as a function of projected distance from the core. 72

4.3 22 GHz KaVA images from September 2014 to June 2016. The contour levels start at three times the rms noise value and increase in steps of 2. Jet component identification colors are same as Figure 4.1 LaTeX Error: Can be used only in preambleSee the LaTeX manual or LaTeX Companion for explanation.Your command was ignored.Type I ¡command¿ ¡return¿ to replace it with another command,or ¡return¿ to continue without it.4.1. 73

4.4 A 43 GHz KaVA image of 4C +21.35. The contour levels start at three times the rms noise value (1.14 mJy/beam), and increase in steps of $\sqrt{2}$. The two circles labeled with letters mark jet components that we were able to track reliably, the two grey crossed circles mark jet components we could not re-identity or track reliably. The CLEAN beam size is illustrated on the bottom left (0.79 mas × 0.63 mas). 75

4.5 Jet kinematics derived from the 43 GHz KaVA maps. *Upper panel:* Projected distance from the core as a function of time for the two components we could track reliably. *Lower panel:* Apparent jet speed as a function of projected distance from the core for the two components shown in the upper panel. 76

4.6 43 GHz KaVA images from May 2015 to June 2016. The contour levels start at three times the rms noise value and increase in steps of 2. Jet component identification colors are same as Figure 4.4 LaTeX Error: Can be used only in preambleSee the LaTeX manual or LaTeX Companion for explanation.Your command was ignored.Type I ¡command¿ ¡return¿ to replace it with another command,or ¡return¿ to continue without it.4.4. 77

4.7 Flux evolution of KaVA jet components. *Top panel:* For the three inner jet components at 22 GHz. *Bottom panel:* For the two components at 43 GHz. 79

4.8 KaVA spectral index map of 4C +21.35 from May 2015 data. 81

4.9 Jet kinematics derived from BU Program 43 GHz data. *Top panel:* Core distance as a function of time for four jet components. *Bottom panel:* Jet component speed as a function of core distance. Error bars represent 1σ uncertainties. 83

4.10 Jet component speeds as a function of core distance for three different 43 GHz datasets. Blue: VLBA; green: KaVA data; skyblue: VLBA with KaVA-like *uv* coverage. Error bars represent 1σ uncertainties. 84

4.11 Jet kinematics derived from MOJAVE 15.4 GHz data. *Top panel:* Core distance as a function of time for four jet components. *Bottom panel:* Jet component speed as a function of core distance. The 1σ error bars are smaller than the symbols. 86

List of Tables

2.1 Our taget sources. 22
2.2 Overview on observations in 2011 and 2012. 24
2.3 Overview on observations in 2012 and 2013 25
2.4 Overview on observations in 2013 26
2.5 The variability parameters. 36

4.1 Overview of our KaVA observations. 68
4.2 Best-fit parameters for each Gaussian jet component, for the period of April 21–22, 2016. 74
4.3 The KaVA jet parameters. 80

Chapter 1

Introduction

1.1 Active Galactic Nuclei

1.1.1 AGN overview

Among all other astonishing astronomical objects in the universe, there are Active Galactic Nuclei. They are located in the center of galaxies and outshine their host galaxies, emitting bolometric luminosity of $\sim 10^{42}$ erg s^{-1}.

Radio emissions from AGN were found to be the synchrotron emission by relativistic electrons gyrating along magnetic field lines. The origin of the enormous energy output was a controversial discussion topic since the emission regions were expected to be quite compact which was constrained by small variability timescales of days. The generally accepted as only probable physical mechanism is that accreting matters fall into an extremely massive and compact object and they release potential gravitational energies. Accordingly, the supermassive black holes (SMBH) with masses of $10^6 - 10^{10}$ $M_\odot$ are believed to power the AGN.

Figure 1.1 shows a schematic view of AGN structures. The SMBH lies at the center of AGN and is surrounded by accreting matters forming a hot, viscous accretion disk. Above the accretion disk, the broad line region (BLR) gas clouds are located near the SMBH. These BLR clouds move extremely fast and are responsible for the broad emission lines in the AGN spectra. A donut-like dusty torus encloses and obscures inner

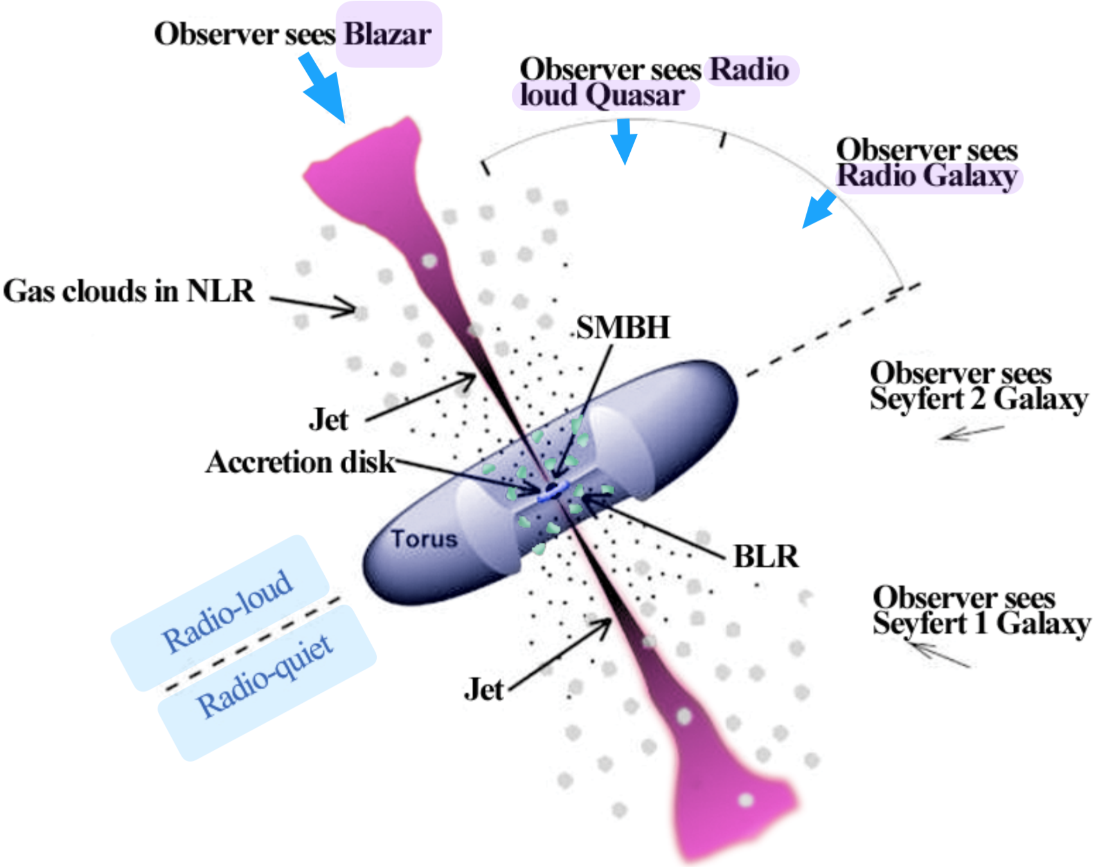
Observer sees Blazar
Observer sees Radio loud Quasar
Observer sees Radio Galaxy
Gas clouds in NLR
SMBH
Observer sees Seyfert 2 Galaxy
Jet
Accretion disk
Torus
BLR
Observer sees Seyfert 1 Galaxy
Radio-loud
Radio-quiet
Jet

Figure 1.1. Schematic view of AGN structure. The classification according to the viewing angles and radio loudness are also illustrated. Colors are added and the original image by Fermi, NASA.

structures. Along the rotation axis, the narrow line region (NLR) clouds reside outside the torus reaching out further at ~ 100 pc. A relativistic twin jet is formed along the spin axis of the black hole and extends to the galactic scale. This synchrotron emitting plasma is accelerated and collimated as moving outward at relativistic speeds. The jets are later dissolved in the outer intergalactic space and sometimes form a big radio lobes or hot spots. In this unification concept (Urry & Padovani 1995), as can be seen from the Figure 1.1, the existence of the torus obscuring the inner structures makes the identification of AGN dependent on the viewing angle.

Once Fanaroff & Riley (1974) classified the radio galaxies into the low luminosity type (FR I) and the high luminosity type (FR II). The FR I galaxies show jets brightest near the core and dimmer towards the edge-darkened lobes at further distance and tend to show complicated bent geometries. The FR II galaxies usually have straight jet geometry and very bright radio lobes or hot spot at the termination. They typically show one-sided jet and the emission is stronger in the lobes than the core.

Quasars are typically divided into radio-loud and radio-quiet ones, determined by the luminosity ratio between the radio and the optical band: The dividing line is 10 by Kellermann et al. (1989, and reference therein). They also found radio-loud quasars take up only $\sim 10\%$ of the quasar population. We call these radio-loud quasars with enhanced emission by Doppler boosting the “blazars”.

Blazars also classified into two types in a spectroscopic sense, one is BL Lacertae (BL Lac) objects, the other is flat spectrum radio quasars (FSRQ). While BL Lacs have very weak or none emission lines (with the equivalent width $< 5\AA$) with low power, FSRQs show strong broad emission lines with high power. According to the unification scheme by Barthel (1989); Urry & Padovani (1995), the quasars appear to be the beamed FR II galaxies with the very small viewing angle to the observer and the BL Lac objects are associated with the FR I galaxies. Usually FSRQs tend to have larger accretion rate than BL Lac objects.

Blzars whose relativistic jets are toward our line of sights have SED produced from non-thermal synchrotron emissions and have two characteristic peaks as can be seen in Fig. 1.2, The first peak is located from the infrared (IR) to x-ray band and the second peak is in the MeV to TeV energy band, sometimes even to TeV regime. The synchrotron emission from the relativistic particles is responsible for the first peak, and the second peak is due to inverse Compton scattering of the same electrons inducing the synchrotron emission. In the frequency ranges less than the first peak, the photons are produced by the electrons and absorbed by other electrons. This synchrotron self-absorption happens in the optically thick region of the spectrum and the optically thin region is continued. The synchrotron self-absorption turnover at the first peak in the AGN spectrum usually falls in the radio domain, then the optically thin emission proceeds.

While FSRQs, in general, show the first SED peak at infrared domain, BL Lac objects can further be classified depending on the location of the synchrotron peak frequencies in the SED. The low- and intermediate- and high-synchrotron peaked BL Lacs (LBLs, IBLs, HBLs) have their dividing freqeuncies at $\nu_{peak} = 10^{14}$ & $10^{15}\,$Hz, respectively. Additionally, Fossati et al. (1998) proposed a so-called "Blazar Sequence" in blazar SEDs which suggests a sequential movement of the two SED peaks as the luminosity varies. FSRQs are the most powerful sources with the lowest peak frequencies and HBLs are the least luminous sources. Ghisellini et al. (2017) developed the blazar sequence study which is shown in Fig 1.2. Their study shows FSRQs have similar shape of SEDs when the luminosity increases, only the high-energy peak goes slightly up which makes the x-ray spectrum harder at the larger luminosity. BL Lac objects tend to show smaller peak frequencies as the luminosity increases, resulting in a softer gamma-ray slope and the Compton dominance becomes larger. For the whole blazar family, those characters become stronger, because FSRQs take up the highest luminosity population and BL Lacs fill in the lowest luminosity population.

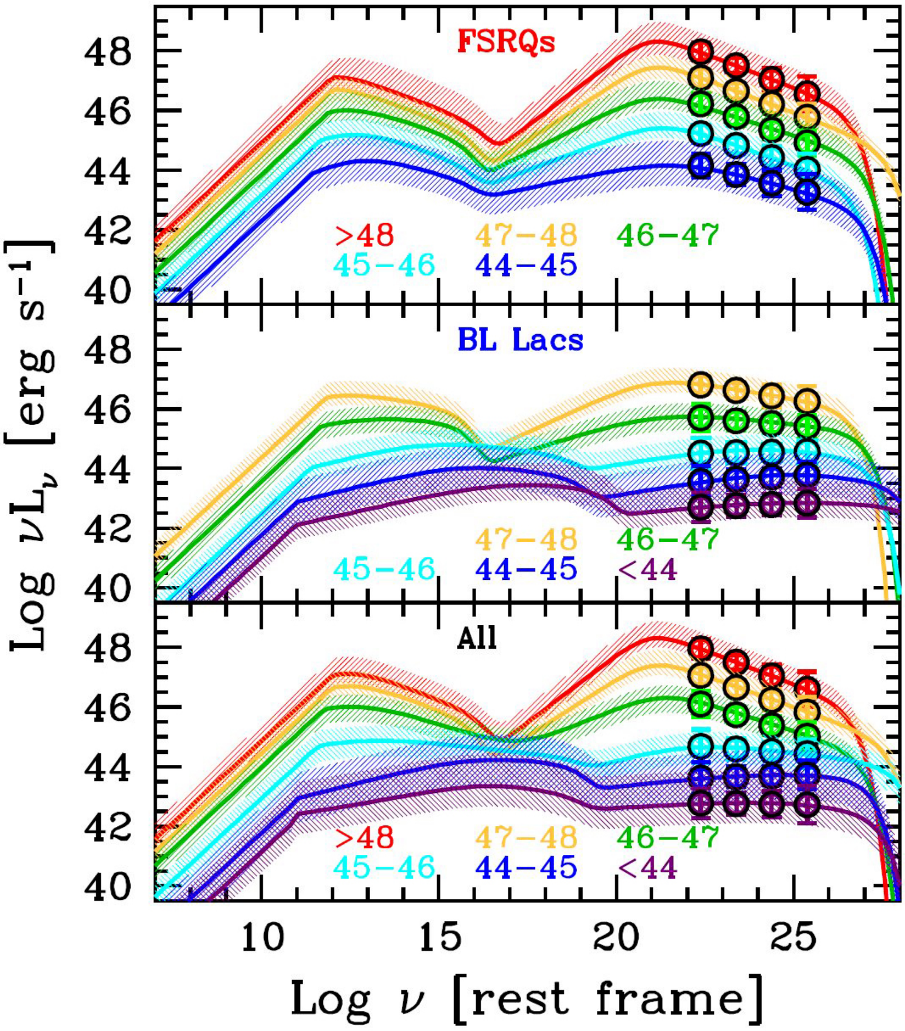

Figure 1.2. Blazar sequence by Ghisellini et al. (2017). *Top :* SEDs of FSRQs show stronger Compton dominance as luminosities become larger. *Middle :* SEDs of BL Lacs show smaller peak frequencies as the luminosity increases. *Bottom :* Combined SEDs of FSRQs and BL Lacs show more prominent features.

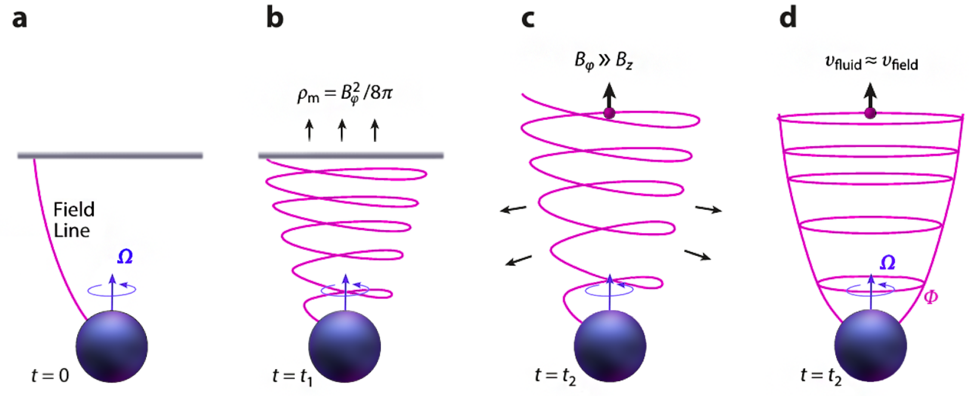

Figure 1.3. Simple jet formation mechanism with a spinning object and attached magnetic field lines. (a) A sphere is attached to the ambient medium with a poloidal field line. (b) Magnetic field lines are wound up like a coil. (c) The spring-like magnetic coil pushes the medium upward. (d) The jet is formed with the toroidal field loops. Original image by Davis & Tchekhovskoy (2020).

1.1.2 Relativistic Jets

Jet Formation, Collimation and Acceleration

The AGN jets usually radiate huge synchrotron and inverse Compton emission and stretch to the large scale.

How jets are formed is still an open question. Generally accepted idea is that SMBH is the central engine of a jet and the acceleration to relativistic speed is achieved by magnetic fields under constant collimation (Vlahakis 2015). Davis & Tchekhovskoy (2020) explained this in a simple way (see fig 1.3): Imagine a magnetic field line is dangling from a ceiling and holding a conducting sphere at the same time, then,

(a) The sphere spins at an angular frequency of Ω.

(b) as the sphere spins, the magnetic field line gets wound like a coil.

(c) The magnetic coil acts like a spring with the help of the toroidal field pressure and pushes up the ceiling.

(d) Any plasma which is attached to the field line is now accelerated and becomes a jet. The new toroidal loops are continuously created by the on-going spin of the sphere.

Depending on the identification of the rotating sphere, there are mainly two favored theories. Blandford & Znajek (1977) suggested a SMBH spin as a candidate (B-Z mechanism) and later Blandford & Payne (1982) proposed accretion disk as the rotating feature (B-P mechanism). Though it's still controversial which mechanism is in charge, there have been much attention on the B-Z mechanism (Ghisellini et al. 2014, e.g.).

The AGN jets launched from the central engine are accelerated and collimated over a long distance of parsec scales. Considering the initial toroidal fields are not strong enough to hold the jet collimated especially when the jet speed goes relativistic, the jet would seem likely to lose its internal pressure and expand at further distance. With Jet being still collimated, other requirement should meet to keep the jet structure as suggested (Nakamura et al. 2018). Most likely, the magnetic field and the pressure by the external medium appear to play an important role in collimation process and, in the case of the spine-sheath structured jet, the outer sheath can take the place (Asada & Nakamura 2012; Mertens et al. 2016). Under this collimation circumstances with magnetic pressure gradients, jet can be accelerated to relativistic speeds (Komissarov et al. 2007), proving the tight relation of the two conditions of collimation and acceleration. In order to reach mega-parsec distances, it is also crucial that the particle acceleration in the jet is very efficient.

So far, the magnetic field carried energy from the spinning black hole and transported it to further distances. Matters were withdrawn from the accretion disk by winds. Which medium, the Poynting flux or matter, is the dominant factor depends on the circumstances. Magnetohydrodynamic simulation studies using general relativity show that Poynting flux is dominant in the inner fast spine structure, while matter is dominant in the outer slow sheath of the jet (Mizuno et al. 2007; Fragile 2008). In a usual sense, a jet is dominated by the Poynting flux in the early stage, and later stage, majority of the magnetic field energy is converted to the kinetic energy, which dominates the jet around 107 Schwarzschild radii (R_s) (Sikora et al. 2005). Now, the magnetic field becomes dynamically negligible, the jet follows the physical law of gas dynamics. Thus, hydrodynamic shocks and plasma instability start to affect the jet and the dissipation process takes place.

Jet Structures

To investigate the jet in detail, the angular resolution should reach sub-milli-arcsecond scale, which can only be achieved by VLBI observations. Accordingly, radio interferometric observations have brought us much information of parsec-scale jets. Typical picture of AGN jets show a compact and bright core, a continuous jet feature, and lobes or hot spots at the termination.

In the inner region of the jet, the optical depth is too high in radio band. Jet becomes visible when the optical depth is low enough, reaching the radio core, therefore the jet appears to be emanating from it (Blandford & Königl 1979). The radio core located parsecs far from the central engine takes majority fraction of parsec scale emission and has a flat spectrum with weak polarization. The flat spectrum is suspected to come from the super-position of synchrotron self-absorption regions, implying the synchrotron opacity changes with the frequencies. Thus, radio core position is not fixed, depending on the frequencies, the core location is different which is known as "core-shift" effect. However, theories also argue that the radio core is to be a recollimation shock, where no core-shift effect is observed (Marscher et al. 2018). The measured brightness temperatures of the radio core come very close to or even exceed the inverse Compton limit especially when the source is in flaring activity, suggesting the core is particle dominated. Many of the physical aspects of VLBI cores are still in open debate.

The jet emission comes mainly from the relativistic hdyro-dynamic shocks, which is easily seen at parsec scales (Blandford & Königl 1979; Marscher & Gear 1985): VLBI images often show clumpy and many discrete jet features which are called blobs and knots. Shocks are created when there are pressure gradient at the jet edge or the jet

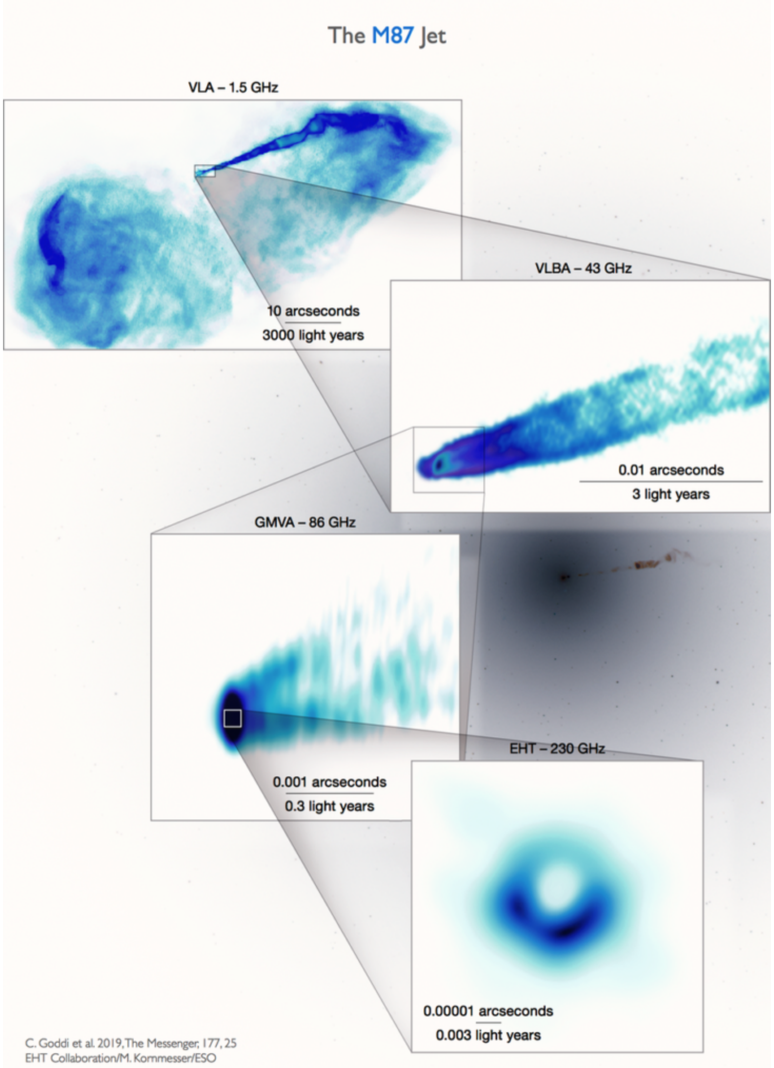
The M87 Jet
VLA – 1.5 GHz
10 arcseconds
3000 light years
VLBA – 43 GHz
0.01 arcseconds
3 light years
GMVA – 86 GHz
0.001 arcseconds
0.3 light years
EHT – 230 GHz
0.00001 arcseconds
0.003 light years
C. Goddi et al. 2019, The Messenger, 177, 25
EHT Collaboration/M. Kommesser/ESO

Figure 1.4. M87 radio jet observed with different VLBI arrays, frequencies at various scales. The smallest scale shows the black hole shadow, the intermediate scales show collimated jet features, the largest scale shows termination of the jet. Original image by ESO.

base when the bulk Lorentz factors increases, or when disturbances such as new plasma ejections propagate through the jet. In the propagating shock regions, particles are accelerated and magnetic field is strengthened, producing radio flares in the light curves. Shocks in the jet show apparent superluminal speeds usually at $< 10c$, sometimes up to $\sim 50c$ (Lister et al. 2016). The spectrum of the shock resembles a homogeneous synchrotron source (Marscher & Gear 1985). Shock evolution is explained in three stages. In the first stage of shock growth, the flux densities at all wavelengths rise and Compton dominance is weakened. The turnover frequency stays the same in this stage. The synchrotron losses begin to dominate when the magnetic field energy density becomes same as photon energy density. In this second stage, the spectrum shows a constant peak flux and the turnover frequency becomes low. In the last stage, the adiabatic losses become dominant and the shock finally fades away. Additionally, jets sometimes have bright and stationary spots (e.g. Kellermann et al. 2004; Lister et al. 2009). These spots are normally considered as standing shocks by recollimation in the jet. At the base of a jet, non-thermal high-energy particles are thought to be produced in the stationary components (Arshakian et al. 2010), which might be the transition site of the jet. Also, in a slightly larger scale, a spine-sheath velocity structure in a jet was proposed (Sol et al. 1989). This model fits well in the kinematics by Boccardi et al. (2016); Mertens et al. (2016).

Blazar jets

For the case of blazar jets where the jet direction is close to out line of sight, strong Doppler beaming effect appears. The Doppler effect boosts the luminosity of the approaching jet and de-boosts the receding jet, so the counter-jet becomes invisible to the observed. This effect is determined by the viewing angle θ, the Lorentz factor Γ, and the speed of the jet in the source's frame as

$$D = \frac{1}{\Gamma(1 - \beta \cos\theta)} \tag{1.1}$$

As the viewing angle becomes smaller, the Doppler boosting factor becomes larger. Doppler effect dramatically changes our view of the sources, as the flux density is boosted and geometrically the jet appears to be shorter and fatter, more bent than real feature (Marscher 2006).

For a small viewing angle and relativistic jet speed, the apparent superluminal motions are explained via,

$$\beta_{app} = \frac{\beta \sin\theta}{1 - \beta \cos\theta} \tag{1.2}$$

where β_{app} is the apparent transverse speed, β is the emission region speed in the jet. When the viewing angle θ becomes small enough, the apparent speed can be *faster* than the speed of light, c.

1.1.3 High Energy Radiation

The second hump of blazar SED lies in MeV-GeV band sometimes extends to TeV. The responsible emission process is inverse Compton scattering of seed photons by the relativistic electrons provided by the jet itself. Thus it's the same population of electrons that create both the low-frequency and high-frequency peaks in the SED. In terms of where the soft seed photons originate, there are a few candidates considering the proposed inner structure near the central engine. Firstly, the jet itself emits the synchrotron photons so that part of them can be up-scattered to radiate at higher energies, which is the synchrotron self-Compton mechanism (Maraschi et al. 1992).

As for the seed photons coming from the external reservoirs which is called External Inverse-Compton model, the accretion disk and BLR cloud can provide optical or UV photons (Dermer & Schlickeiser 1993), the infrared photons emanate from the dusty torus (Sikora, Begelman & Rees 1994). If considering the existence of the relativistic protons in the jet, proton-synchrotron process may also produce the gamma-ray emission (Aharonian 2000). In the both leptonic model and hadronic model in which electrons and protons are responsible respectively, acceleration mechanism must be extremely efficient in the jets. For the case of the HBLs, the lepton synchrotron emission is thought to be mainly responsible for providing seed photons and for the LBLs and FSRQs, the EIC models appear to be an active process and hadronic models are usually disfavored (Sikora et al. 2009; Petropoulou & Dimitrakoudis 2015).

Studies on large samples of data show that there are significantly tight correlations between gamma-ray (at eneries between 100 MeV - 300 GeV) and radio light curves (Ackermann et al. 2011; Fuhrmann et al. 2014), which suggests both bands share the same emission origin. Those studies also found that the high frequencies usually lead the radio band variabilities. Theoretically, the observed behavior can be due to dramatic particle density changes taking place in the base of the jet, the innermost region near the central engine. VLBI observations with high angular resolutions have provided numerous evidences that, particularly from quasars, the radio emitting region is where the gamma-ray flares occur, which is further out than the BLR. Frequently, gamma-ray flares occurred as a new jet component is ejected at a relativistic speed and the polarized radio flux peaks locally. The optical and X-ray activity is also enhanced and electric vector position angle shows significant rotations (Jorstad et al. 2010; Marscher et al. 2010). The gamma-ray originated mm-VLBI core is sometimes identified as a standing shock (Marscher et al. 2010), where the acceleration and collimation process come into an end. For the gamma-ray activity leading the mm-wavelength variability, Lisakov et al. (2017); Karamanavis et al. (2016b) found that the origin of the leading high-energy emission is parsecs upstream of the radio core.

Those observational evidences, which show the connection between high-energy activity and the radio emission and their co-spatial origin which is parsecs far from the SMBH, are interpreted as “far dissipation” mechanism. On the contrary to the “near dissipation” scenario, where BLR clouds provide the seed photons, far dissipation scenario suggests that the particles are accelerated efficiently at much further distances than BLR. Then the responsible seed photons come from the dusty torus or the jet itself and are up-scattered via synchrotron self Compton or external inverse Compton process.

A major difficulty in extragalactic high-energy studies is the process of pair-production between the blazar originated gamma-ray and low-energy photons from the diffuse extragalactic background light (EBL). This absorption results in the softening in the spectrum and higher energy of the gamma-ray photon and sources with longer distances are more severely affected.

1.2 Very Long Basline Interferometry

The highest angular resolution so far is achieved by VLBI observation using telescopes located all over the globe. The basic concept of VLBI is that connecting many observatories separated by large distances makes their longest baseline (the separation between two antennas) a diameter of a virtual gigantic telescope (e.g. the size of the Earth radius) (see Figure 1.5). Consequently, achieved angular resolution goes usually down to milli-arcsecond scale at radio band.

The simplified main VLBI observation procedure is carried out as follows,

i Many pairs of antennas at different locations observe the target source. At each stations, the observed light signal is sent to a heterodyne receiver.

ii The signals from the receiver are digitized and recorded. A high-precision time information (e.g. from a hydrogen maser) is also saved along with the signals for later correlation process.

iii The data from all different stations are collected and correlated with a hardware or software at a correlation center. In the correlation process, complex interferometric visibilities are calculated at a timescales of minutes.

iv The visibilities are distributed on the uv-plane, with u and v corresponding to the

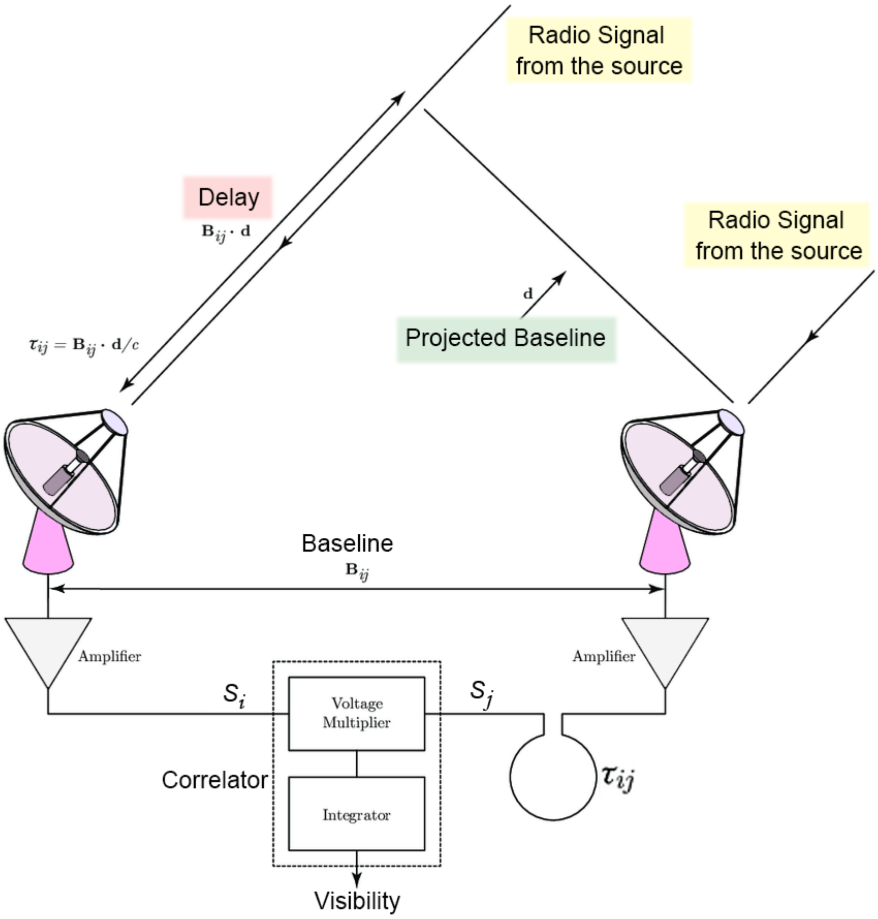
Radio Signal from the source
Delay
$\mathbf{B}_{ij} \cdot \mathbf{d}$
Radio Signal from the source
d
$\tau_{ij} = \mathbf{B}_{ij} \cdot \mathbf{d}/c$
Projected Baseline
Baseline
$\mathbf{B}_{ij}$
Amplifier
Amplifier
S_i
S_j
Voltage Multiplier
Correlator
Integrator
τ_{ij}
Visibility

Figure 1.5. Schematic picture of Very Long Baseline Interferometry. A pair of antennas receiving signals from a source. A signal delay of τ and projected baseline, d, is indicated. Original image from Mahmoud et al. (2011).

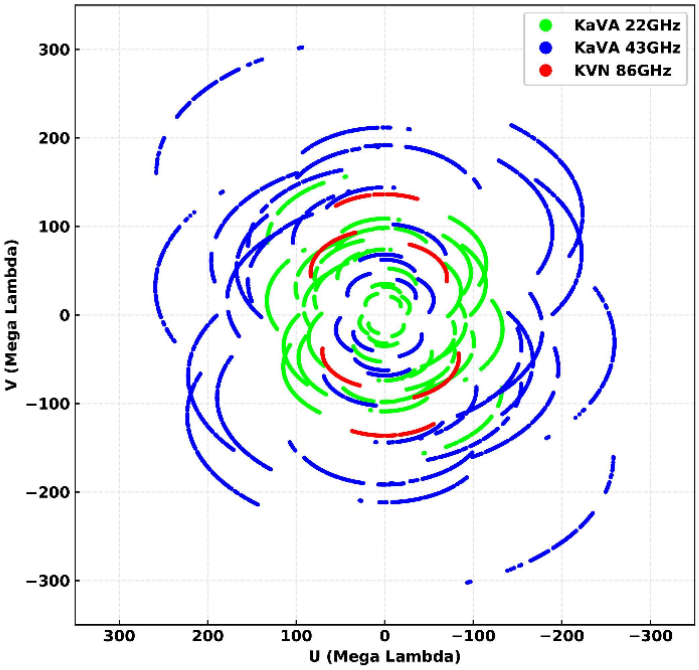

Figure 1.6. *uv*-coverage of the KVN and VERA joint array (KaVA). Different colors correspond to the different array or observation frequencies. Image from Hada et al. (2020).

North-South and East-West direction projected on the sky. The visibilities make an arc lines on the uv-plane due to the Earth rotation and the whole accumulated visibilities correspond to the "dirty beam" or the point spread function (see Figure 1.6).

v Fourier transform of the visibilities on the uv-plane produces an image of the target source on the xy-plane as the van Cittert-Zernicke theorem states.

After the observations and correlations, the interferometric data still need series of reduction processes including phase correction, amplitude correction, visibility phase correction, and global fringe fitting from the corrected signals. Usually this processes are carried out in `AIPS` software package[1] with various dedicated tasks.

The raw image obtained by Fourier transform after the calibrations is called a 'dirty map,' which incubates a true source image. The dirty map has artifacts or side-lobes to be removed, which were created by the sparse visibility distribution due to limited number of baseline, observation time, declination of the source, etc. In order to reveal the true source image, the dirty map should be de-convolved with a dirty beam (PSF) to remove the artifacts. The `CLEAN` algorithm by Högbom (1974) is commonly used for the de-convolution procedure. Repeated subtraction of the dirty beam from the dirty map is required until the residual levels reach below the image noise. Once the de-convolution is done, the source image can be generated. Though `AIPS` is also capable of generating the images, other software, `Difmap`[2] is widely used as in this thesis.

1.3 Thesis outline

The thesis is structured as follows. In the following chapters, we will discuss the details of the topics, which were covered in this chapter. In Chapter 2, we report the KVN single dish observation results regarding intra-day variability analysis on four bright nearby AGN (3C 111, 3C 279, 3C 454.3, BL Lac). Our work on the BL Lac object, PKS 1749+096, initiated by our KVN VLBI observation is presented in Chapter 3, where we discuss the radio flares associated with Gamma-ray flare and their connection with the kinematics study. Our results of jet kinematics on the FSRQ, 4C +21.35 from dense quasi-simultaneous VLBI observations carried out with KaVA at two frequencies are shown in Chapter 4. Our conclusion is followed in Chapter 5.

---

[1] `http://www.aips.nrao.edu/index.shtml`

[2] `https://www.cv.nrao.edu/adass/adassVI/shepherdm.html`

Throughout the thesis, we adopt a cosmology with $\Omega_m = 0.27$, $\Omega_\Lambda = 0.73$, and $H_0 = 71$ km s^{-1} Mpc^{-1}.

Chapter 2

A Search for Intra-day Variability with KVN[1]

2.1 Abstract

Active galactic nuclei (AGN) are known for irregular variability on all time scales, down to intra-day variability with relative variations of a few percent within minutes to hours. On such short timescales, unexplored territory, such as the possible existence of a shortest characteristic time scale of activity and the shape of the high frequency end of AGN power spectra, still exist. We present the results of AGN single-dish fast photometry performed with the Korean VLBI Network (KVN). Observations were done in a "anti-correlated" mode using two antennas, with always at least one antenna pointing at the target. This results in an effective time resolution of less than three minutes. We used all four KVN frequencies, 22, 43, 86, and 129 GHz, in order to trace spectral variability, if any. We were able to derive high-quality light curves for 3C 111, 3C 454.3, and BL Lacertae at 22 and 43 GHz, and for 3C 279 at 86 GHz, between May 2012 and April 2013. We performed a detailed statistical analysis in order to assess the levels of variability and the corresponding upper limits. We found upper limits on flux variability ranging from $\sim 1.6\%$ to $\sim 7.6\%$. The upper limits on the derived brightness

---

[1] Published in the Journal of The Korean Astronomical Society: Lee et al. 2015, JKAS, 48, 313

temperatures exceed the inverse Compton limit by three to six orders of magnitude. From our results, plus comparison with data obtained by the University of Michigan Radio Astronomy Observatory, we conclude that we have not detected source-intrinsic variability which would have to occur at sub-percent levels.

2.2 Introduction

Variability of the flux from active galactic nuclei (AGN) as function of time has been frequently reported at various time scales and wavelengths (see, e.g., Trippe et al. 2011; Benlloch et al. 2001; Fuhrmann et al. 2008; Gupta et al. 2012). Variability on a time scale under one day, so-called *intra-day variability* (IDV), was first detected by Witzel et al. (1986). AGN of various type, such as flat spectrum radio quasars (FSRQs), BL Lacertae (BL Lac) objects, and Seyfert galaxies have been observed to show IDV (Lovell et al. 2008).

Theoretical models constructed for the explanation of IDV mechanisms include accretion disk models with flares or disturbances (Abramowicz et al. 1991), Doppler boosted relativistic jets (Blandford & Königl 1979), and interstellar scintillation (ISS) (Rickett 1990). On the one hand, interstellar scintillation is a source-extrinsic mechanism, due to ionized interstellar medium (de)focusing the light traveling from an AGN to Earth. Lovell et al. (2008) claimed that at 5 GHz the known short term variability can be caused by scintillation. However, ISS becomes irrelevant factor at higher frequency radio bands as it scales with the observation frequency, ν, like $\nu^{-2.2}$. Hence, ISS should be unimportant at >22 GHz. On the other hand, observed brightness temperatures well above the inverse Compton limit suggest Doppler boosting accompanied by rapid intrinsic variability (Kellermann & Pauliny-Toth 1969).

On the shortest time scales, down to a few minutes, the variability of AGN is only poorly probed, implying the need for further investigation for various reasons. Firstly to probe the possible existence of a shortest time scale of AGN activity, possibly given by shocks in relativistic jets (Blandford & Königl 1979; Marscher & Gear 1985). Secondly, the AGN power spectrum at the highest sampling frequency needs to be probed.

Though, on time scale between hours and years, those power spectra are known to obey red noise statistics (Park & Trippe 2014), there is still unknown territory at shorter time scales. In addition, the degree of simultaneity of flux variations across frequency bands ought to be studied. Even though a characteristic time delay between lightcurves obtained at different frequencies due to the variations of the optical depth with frequency is expected by certain emission model based on expanding AGN outflows, this is only found sometimes and on few-hour scales (Marscher & Gear 1985).

For spectroscopic observations with time resolutions of minutes, the Korean VLBI Network (KVN) is the tool of choice. KVN has three identical 21-meter antennas located at three different sites, each equipped with four receivers which can operate simultaneously at up to four frequencies: 22, 43, 86, and 129 GHz. In this paper, we investigate the variability on time scales of few minutes of four AGN: 3C 111, 3C 279, 3C 454.3, and BL Lacertae. Several observing runs were conducted from 2011 to 2013. We derived upper limits on source variability and the corresponding upper limits on brightness temperature.

2.3 Observations

We performed observations with the KVN 21-meter radio telescopes at Yonsei, Ulsan, and Tamna from December 2011 to December 2013. We used all three antennas as independently operating single dishes at all four frequencies of 22, 43, 86, and 129 GHz, partially simultaneously. Jupiter, Venus, and Mars were chosen as amplitude calibrators, since they are stable radio emission sources. We pointed each antenna onto the target for five minutes, then five minutes onto the calibrator. We used a cross scan observation mode to obtain the flux density of the sources. One scan sequence consists of four scans, i.e., back and forth scans in azimuthal direction and in elevation direction, respectively.

To examine the variability on time scale on the order of minutes, it is essential to obtain densely sampled uninterrupted light curves. In order to achieve this, we paired antennas with their receivers tuned to the same frequency and polarization. Whenever

Table 2.1. Our taget sources.

	3C 111	3C 279	3C 454.3	BL Lac
R.A. (J2000)	04:18:21.3	12:56:11.1	22:53:57.7	22:02:43.3
DEC (J2000)	+38:01:36	−05:47:22	+16:08:54	+42:16:40
Redshift	0.0485	0.537	0.859	0.0686
Distance (Mpc)	205	2996	5330	292
Type	Seyfert	FSRQ	Blazar	FSRQ

Note: Source data are from the NASA/IPAC Extragalactic Database (NED), adopting a cosmology with $H_0 = 73\,\mathrm{km\,s^{-1}\,Mpc^{-1}}$, Ω_m=0.27, Ω_Λ=0.73.

one antenna needed to point at the calibrator, the other one was pointed at the target. The maximum slew speed of KVN is three degree per second and the maximum acceleration is three degree per square second, which also helped us to minimize the inevitable time consumption for switching between target and calibrator.

Unfortunately, weather or technical conditions were difficult in general; we could achieve only four successful observation runs, out of 13 in total, resulting in high-quality data, mostly due to rain or cloudy sky. High frequency data were especially vulnerable to humidity; we obtained only one epoch of 86-GHz data and no data at 129 GHz. We had two epochs of three consecutive clear nights each in 2012 and 2013, resulting in long and high-quality light curves of 3C 111. At the low frequency bands of 22 and 43 GHz, 3C 454.3 and BL Lac could be observed in good conditions, however for one epoch only. In spring 2012, observations of 3C 279 with KVN Yonsei and Ulsan stations provided a long and densely sampled light curves at 86 GHz. In late 2013, we tried to catch other sources such as 4C 69.21 at higher frequencies of 86 and 129 GHz, only to fail mostly due to humid weather. Despite our efforts, we failed to combine the two light curves obtained from the paired stations for BL Lac (in April 2013), 3C 111 (in February 2013), and 3C 454.3 (in April 2013) because the quality of the two data sets was too different due to technical problems at one of the stations. For a detailed observations journal, see Tables 2.2 and 2.3. In some cases, data that appeared to be of high quality (in terms of good agreement between cross-scan source profile and theoretical Gaussian) turned out to suffer from systematic uncertainties caused by technical glitches like incorrect time resolution, receiver problems, or further technical errors at a KVN station; those data were excluded from the analysis. Data quality classification is discussed in the following section.

2.4 Data Analysis

The primary data extraction and calibration made use of the Gildas CLASS software package.[2] Each scan across a target provided a (Gaussian for point sources, as was the case for our observations) profile of the amplitude as function of position angle. We sorted out bad scans according to the clearness of the Gaussian shape of the amplitude profile; we assigned a quality flag “high” to scans showing a clear Gaussian profile, and “low” to scans showing nothing like a Gaussian (see Tables 2.2 and 2.3).

We fit a linear baseline to each amplitude profile in order to remove (instrumental and sky) background emission. We fit a Gaussian curve to the amplitude and used the best-fit peak value of the profile as one flux data point. By combining four consecutive data points from one full scanning sequence, we obtained one flux measurement point for a light curve, using the mean value as flux measurement value.

We used the standard deviation of the four scan values as the initial estimate of the statistical error of a given flux measurement. However, error bars obtained this way are seriously affected by low number statistics. Robust error bars can be found from an iterative procedure:[3] (1) calculate a first error estimate $\sigma_{0,i}$ for data point $i = 1, 2, ...$ from the standard deviation of four scan values; (2) compute the average $\sigma_{0,i}$, i.e. $\langle\sigma_{0,i}\rangle$,

---

[2] `http://www.iram.fr/IRAMFR/GILDAS`

[3] Iterative error estimates are well established in stellar dynamics, especially for calculating velocity dispersions from stellar velocities with poorly constrained uncertainties (see Armandroff & Da Costa 1986; Hargreaves et al. 1994 for detailed discussion).

Table 2.2. Overview on observations in 2011 and 2012.

Date		Source	Frequency [GHz]	Obs. Time [Hr] (KY/KU/KT)	Data Quality[†]	$T_{\rm sys}$ [K]
2011	Dec 30	3C279*	22	—/—/5.9	—/—/high	—/—/110
			43	—/—/5.9	—/—/high	—/—/180
			86	5.9/5.8/—	high/high/—	230/260/—
			129	5.9/5.8/—	high/high/—	230/400/—
		BL Lac	22	2.7/2.4/0.9	low/low/high	70/80/110
			43	2.7/2.4/0.9	low/low/high	160/120/180
			86	2.7/2.4/—	low/low/—	170/240/—
			129	2.7/2.4/—	low/low/—	160/350/—
2012	Jan 26	3C279	22	—/—/7.4	—/—/high	—/—/120
			43	—/—/7.4	—/—/high	—/—/180
			86	7.4/7.1/—	low/low/—	190/210/—
			129	7.4/7.1/—	low/low/—	410/590/—
		BL Lac	22	—/—/7.1	—/—/high	—/—/100
			43	—/—/7.1	—/—/high	—/—/140
			86	6.7/3.8/—	low/low/—	170/180/—
			129	6.7/3.8/—	low/low/—	160/200/—
	Feb 21	3C279	86	7.9/7.9/—	high/low/—	230/400/—
			129	7.9/7.9/—	high/low/—	300/760/—
		BL Lac	86	2.9/2.9/—	low/low/—	150/150/—
			129	2.9/2.9/—	low/low/—	290/580/—
	Apr 30	3C279	22	—/—/4.6	—/—/low	—/—/190
			43	—/—/4.6	—/—/low	—/—/190
			86	6.9/—/—	high/—/—	520/—/—
			129	6.9/—/—	low/—/—	1200/—/—

Note. — [†] Referring to the agreement between cross-scan source profile and theoretical Gaussian

*Data suffer from systematic errors due to technical failures (cf. Section 2.3)

Table 2.3. Overview on observations in 2012 and 2013

Date		Source	Frequency [GHz]	Obs. Time [Hr] (KY/KU/KT)	Data Quality[†]	T_{sys} [K]
2012	Apr 30	BL Lac	86	3.1/—/—	low/—/—	190/—/—
			129	3.1/—/—	low/—/—	190/—/—
2012	May 31	3C279	22	—/—/6.9	—/—/high	—/—/240
			43	—/—/6.9	—/—/high	—/—/170
			86	6.8/6.9/—	high/high/—	460/470/—
			129	6.8/6.9/—	low/low/—	1100/1300/—
		BL Lac	22	—/—/3.9	—/—/high	—/—/130
			43	—/—/3.9	—/—/high	—/—/250
			86	3.4/3.8/—	low/low/—	280/290/—
			129	3.4/3.8/—	low/low/—	730/600/—
	Nov 28/29/30	3C111	22	27/—/25	high/—/high	70/—/90
			43	27/—/25	low/—/high	140/—/120
		3C279*	22	16/—/17	high/—/high	70/—/140
			43	16/—/17	high/—/high	150/—/200
2013	Feb 22/23/24	3C111	22	29/—/20	high/—/high	70/—/80
			43	29/29/20	high/low/high	130/200/120
			86	—/29/—	—/low/—	—/200/—
	Apr 18	3C454.3	22	3.8/4.9/4.0	high/high/high	100/100/150
			43	3.8/—/4.0	high/—/high	150/—/150
			86	—/4.9/—	—/low/—	—/260/—
		BL Lac	22	5.6/2.9/5.6	high/high/high	70/120/90
			43	5.6/2.9/5.6	high/low/high	190/110/120
	May 18	3C111	22	—/—/9.0	—/—/high	—/—/160
			43	—/—/9.0	—/—/high	—/—/140
			86	9.6/8.7/—	low/low/—	210/210/—
			129	9.6/8.7/—	low/low/—	980/260/—

Note. — [†]Referring to the agreement between cross-scan source profile and theoretical Gaussian

*Data suffer from systematic errors due to technical failures (cf. Section 2.3)

Table 2.4. Overview on observations in 2013

Date		Source	Frequency [GHz]	Obs. Time [Hr] (KY/KU/KT)	Data Quality[†]	T_{sys} [K]
2013	May 18	3C454.3	22	—/—/3.9	—/—/low	—/—/160
			43	—/—/3.9	—/—/low	—/—/140
			86	3.9/3.9/—	low/low/—	110/180/—
			129	3.9/3.9/—	low/low/—	1000/200/—
	Oct 17	4C69.21	22	5.2/—/—	high/—/—	100/—/—
			43	5.2/—/—	low/—/—	200/—/—
			86	—/9.8/9.8	—/low/low	—/270/230
			129	—/9.8/9.8	—/low/low	—/330/300
		BL Lac	86	—/6.3/7.7	—/low/low	—/260/320
			129	—/6.3/7.7	—/low/low	—/290/500
	Nov 1	3C454.3	86	6.6/—/6.3	low/—/low	260/—/280
			129	6.6/—/6.3	low/—/low	650/—/480
		4C69.21	86	8.8/—/8.8	low/—/low	200/—/430
			129	8.8/—/8.8	low/—/low	390/—/860
	Dec 21	3C111	22	—/—/3.8	—/—/high	—/—/70
			43	—/—/3.8	—/—/high	—/—/110
			86	3.8/3.8/—	high/low/—	150/160/—
			129	3.8/3.8/—	low/low/—	130/150/—
		3C454.3*	22	—/—/5.1	—/—/high	—/—/80
			43	—/—/5.1	—/—/high	—/—/110
			86	5.1/5.1/—	high/high/—	150/180/—
			129	5.1/5.1/—	low/low/—	140/170/—
		4C69.21	22	—/—/1.9	—/—/high	—/—/90
			43	—/—/1.9	—/—/low	—/—/150
			86	1.9/1.9/—	low/low/—	190/200/—
			129	1.9/1.9/—	low/low/—	180/250/—

Note. — [†] Referring to the agreement between cross-scan source profile and theoretical Gaussian

*Data suffer from systematic errors due to technical failures (cf. Section 2.3)

for all data points of a given light curve; and (3) compute the final error σ_i for a given data point via

$$\sigma_i^2 = \frac{1}{2}\sigma_{0,i}^2 + \frac{1}{2}\langle\sigma_{0,i}\rangle^2 \tag{2.1}$$

We removed data points deviating more than 3σ from the mean value. In general, data obtained at the beginning and finishing parts of the observation have large error bars caused by the low elevation of the target and were removed. Furthermore, the KVN antennas seemed to have difficulties in pointing at a target around the time of its transit, resulting in the loss of about 10 to 15 minutes of data in the middle of the light curves obtained in November 2012.

The light curves of the calibrators were normalized to unity averages and were fit with 2nd order polynomials using IDL.[4] The uncalibrated light curves of the targets were then divided by the calibrator model curves, resulting in amplitude calibrated lightcurves of the targets. The maximum elevation difference between target and calibrator was 20°. According to the KVN gain curve,[5] this difference corresponds to about 3 % difference in normalized gain at 22 and 43 GHz, and up to about 6% at 86 GHz.

We achieved a typical time resolution of three minutes and, occasionally, one minute whenever the light curves from paired KVN stations could be combined. For some epochs, only parts of the light curves could be combined since the data from one of the stations were usable only for a part of the total observing time. In some cases (and even when the observation conditions were good at both KVN sites), we found a systematic offset between the two light curves. The most obvious case occurred in the data for 3C 454.3 obtained in April 2013 with a relative offset value of 6.8%. Assuming this was an effect occurring at one of the stations (specifically weather, gain calibration errors, or incorrect aperture efficiency estimates), we multiplied the ratio of the averages to one light curve to remove the offset before combination.

Flux densities were converted from antenna temperature (in Kelvin) to flux density

---

[4] Interactive Data Language, ITT Exelis Inc., McLean (Virginia)

[5] `http://kvn.kasi.re.kr/status_report_2013/gain_curve.html`

(in Jansky) using

$$[\mathrm{Jy/K}] = \frac{2k}{A_{eff}} = \frac{2k}{\eta\pi r^2}, \tag{2.2}$$

where k is the Boltzmann constant, A_{eff} is the effective antenna aperture, η is the aperture efficiency, and r is the antenna radius. The conversion factors are different depending on the sites, frequencies, and time. For KVN, we found values ranging from 12.4 to 14.2 throughout our observation period.

To analyze the variability of the light curves, we applied modulation index (m, in units of %) analysis, using (Kraus et al. 2003)

$$m = \frac{stddev}{mean} \times 100\% \tag{2.3}$$

where *stddev* and *mean* are the standard deviation and mean values of the flux densities.

We also performed a reduced χ^2 test assuming a constant flux density with (Kraus et al. 2003)

$$\chi_r^2 = \frac{1}{N-1}\sum_{i=1}^{N}\frac{(S_i - \langle S\rangle)^2}{\sigma_i^2} \tag{2.4}$$

where N is the number of data points, S is the flux density, σ_i is the error derived according to Equation (2.1), and $\langle\cdot\rangle$ denotes the average of the enclosed quantity. The modulation indices and reduced χ^2 values are listed in Table 2.5.

Taking the standard deviation of a given lightcurve and the observed time period as proxies for the amplitude of flux variation and the variability time scale, respectively, we obtained limits on the brightness temperatures using (Wagner & Witzel 1995),

$$T_b = 4.5 \times 10^{10} A_{var}\left[\frac{\lambda d}{t_{var}(1+z)}\right]^2 \tag{2.5}$$

where A_{var} is the amplitude of flux variation (in units of Jy), λ is the observation wavelength (in cm), d is the distance to the source (in Mpc), t_{var} is the variability time scale (in days), and z is the redshift of the source. Our upper limits on brightness temperatures are listed in Table 2.5. They range from 1.2×10^{15} K to 2.9×10^{18} K, much higher than the inverse Compton limit of $T_{max} = 10^{12}$ K. In general (e.g., Fuhrmann et al. 2008), the occurrence of brightness temperatures in excess of the inverse Compton

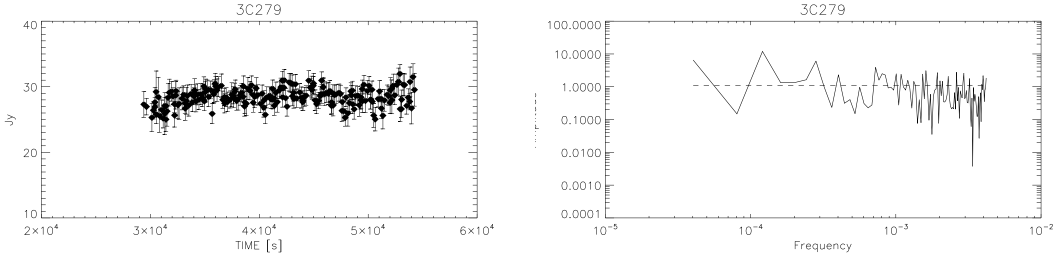

Figure 2.1. The 86-GHz lightcurve (left) and power spectrum (right) of 3C 279 as observed in May 2012. The dashed line in the power spectrum indicates the mean value; the sampling frequency is in units of s^{-1}. Note that the axis scales are logarithmic, leading to downward spikes being more pronounced that upward deviations.

limit is interpreted as an effect of Doppler boosting. The corresponding Doppler factors can be found from (Wajima et al. 2014),

$$\delta = (1+z)\left(\frac{T_b}{10^{12}K}\right)^{1/(3-\alpha)} \tag{2.6}$$

where z is the redshift of the source and α is the spectral index which is typically assumed to be 0.6, defined via $S_\nu \propto \nu^{-\alpha}$ (cf., Kim & Trippe 2013).

The emission from AGN is known to follow red-noise statistics with amplitudes $A_f \propto f^\beta$ (f being the sampling frequency) with $\beta < 0$ (e.g., Park & Trippe 2014). Accordingly, we used Scargle periodogram analysis (Scargle 1982) to constrain the statistics of our lightcurves. Especially, we aimed at distinguishing intrinsic variability (which is likely to show $\beta < 0$) from instrumental and atmospheric fluctuations which would show white noise behavior ($\beta = 0$).

2.5 Results

2.5.1 3C 279

Being our brightest target source, 3C 279 was observed in May 2012, providing the only 86-GHz data set we could obtain (Figure 2.1). The two paired KVN stations contributed a dense and high-quality lightcurve throughout the whole observation period.

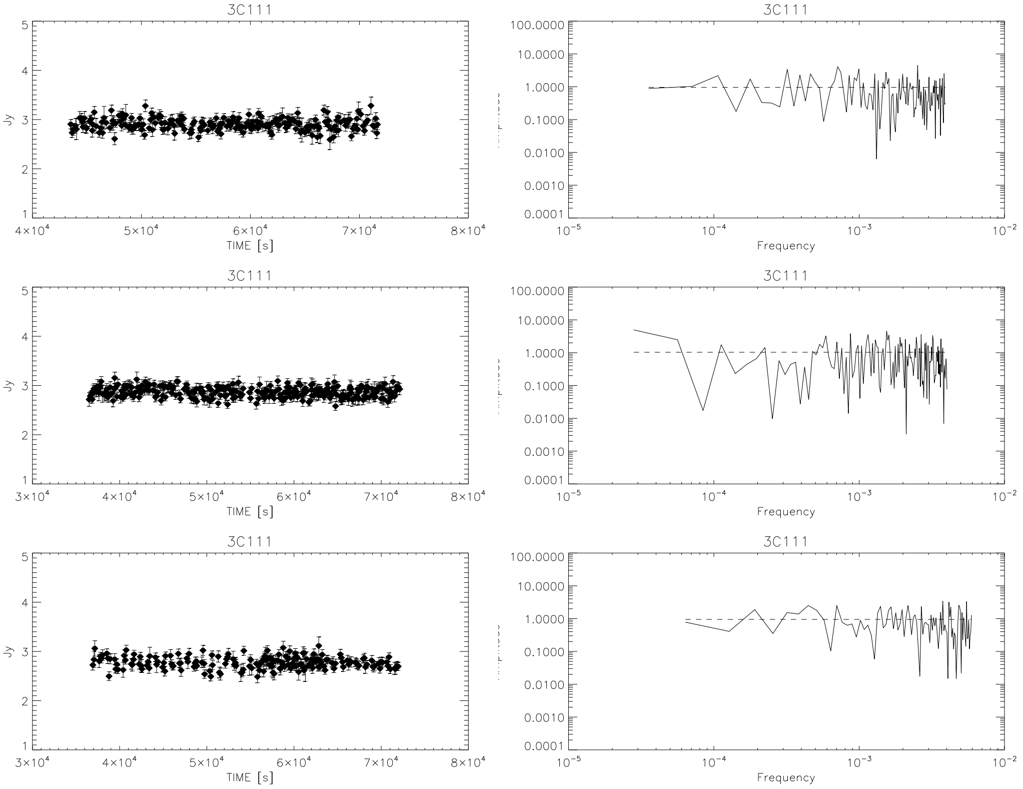

Figure 2.2. The 22-GHz lightcurves and power spectra of 3C 111 observed during three consecutive days in November 2012. Dashed lines in the power spectra indicate mean values; the sampling frequency is in units of s^{-1}.

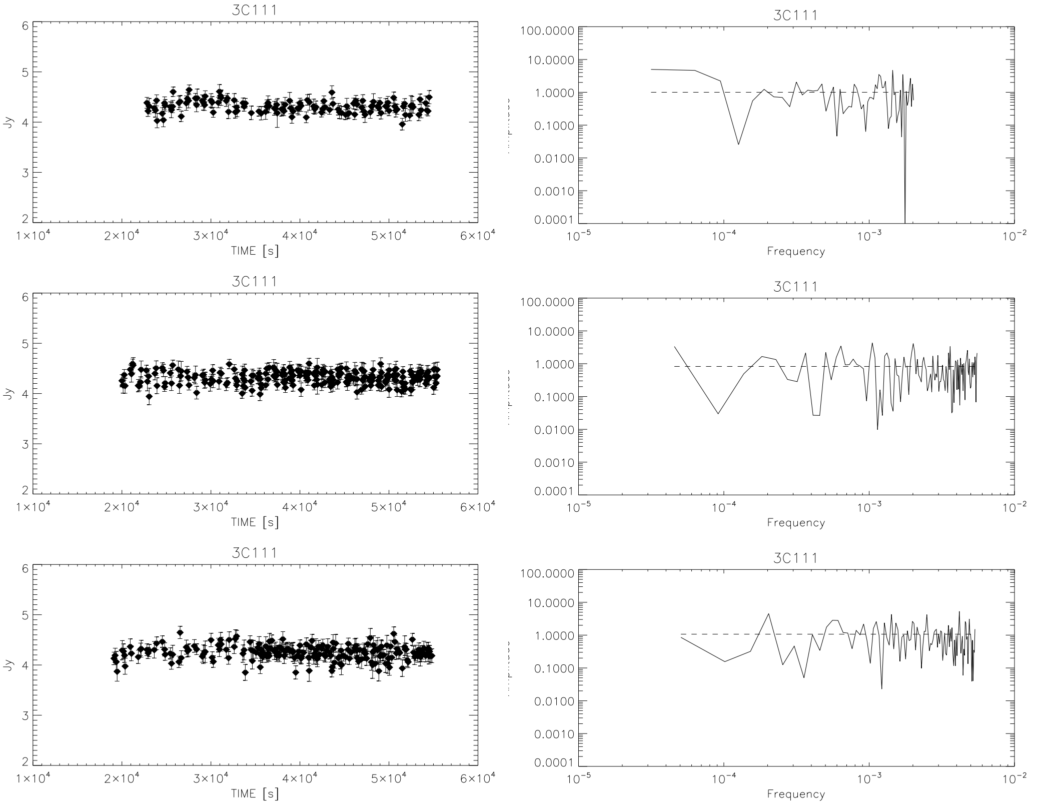

Figure 2.3. The 22-GHz lightcurves (left panels) and Scargle periodogram (right panels) of 3C 111 observed at three consecutive days (from top to bottom) in February 2013. The sampling frequency of the periodograms is in units of s^{-1}.

The lightcurve appears flat within errors with slight ups and downs at the beginning and the end; these deviations come with relatively large error bars and scatter, and occur at times of low elevations. The power spectrum is essentially flat (powerlaw index $\beta \approx 0$), implying a white noise time series.

2.5.2 3C 111

Partially thanks to its high declination, 3C 111 could be observed for the longest observation time among our targets, 56 hours in total. In November 2012 (Figure 2.2), the light curves of all three observing days show remarkably constant flux density of around 2.8 Jy, with m values lingering around 4%, and reduced χ^2 values around 1.3.

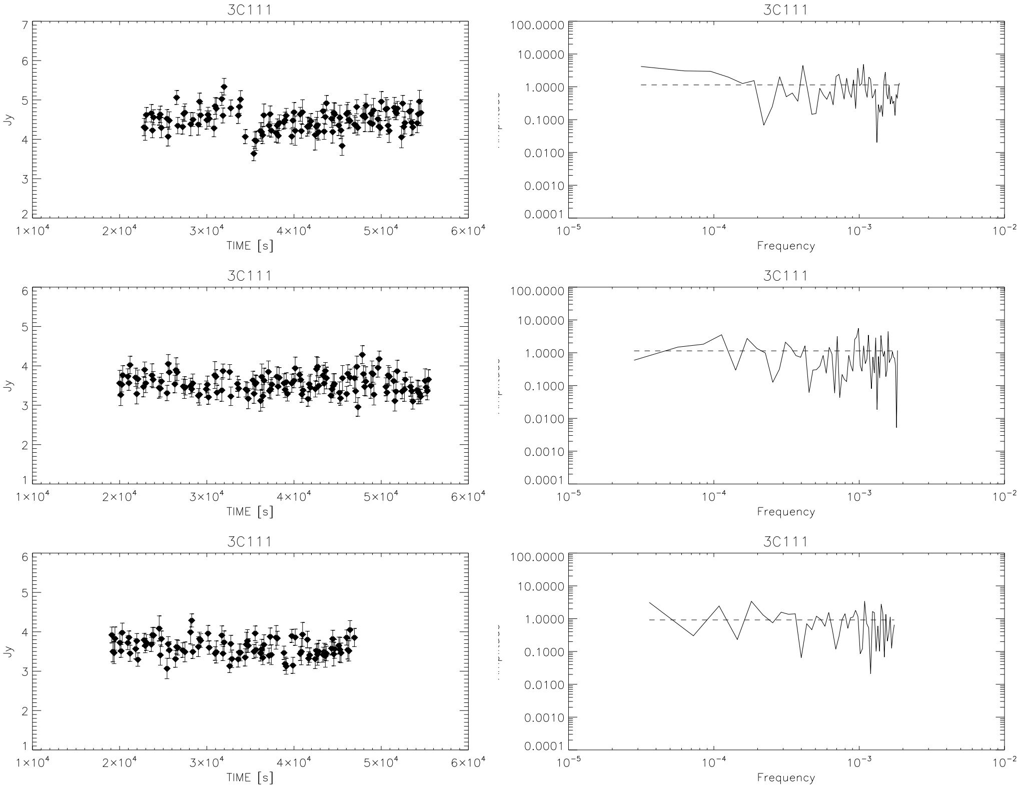

Figure 2.4. The 43-GHz lightcurves (left panels) and Scargle periodogram (right panels) of 3C 111 observed at three consecutive days (from top to bottom) in February 2013. The sampling frequency of the periodograms is in units of s^{-1}.

The power spectra appear to be flat most times.

3C 111 still seemed to be equally calm three months later, when observed at 22 GHz in February 2013 (Figure 2.3). The weather conditions were consistently fine, the light curves are almost flat with mean fluxes around 4.3 Jy. The m values are 2.8%, 3.0%, and 3.4%, respectively. Reduced χ^2 values range from 1.1 to 1.3. At 43 GHz (Figure 2.4), the light curves show larger error bars than the 22 GHz data and show slight systematic variations. Both reduced χ^2 and m values are a little higher than those of the 22 GHz lightcurves. The data from the first day show a "break" feature caused by an antenna pointing instability around the time of the transit of the target. The power spectra for both frequencies are almost constant.

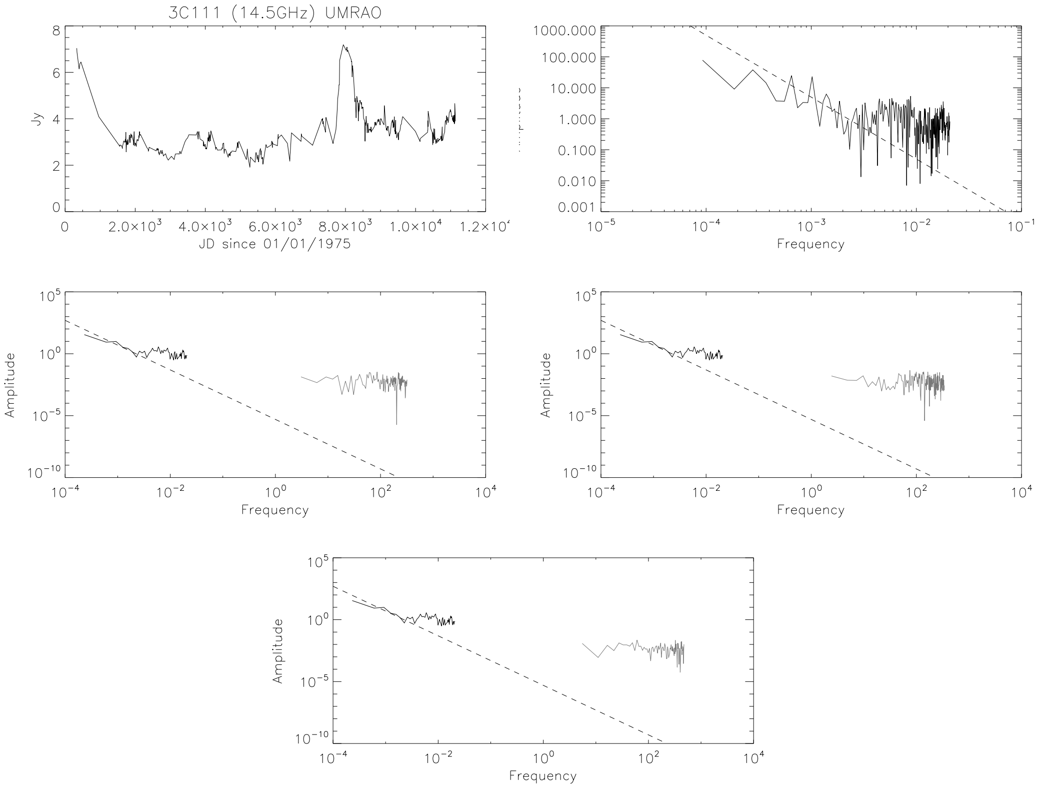

Figure 2.5. *Top left:* UMRAO lightcurve of 3C 111 observed at 14.5 GHz from 1975 to 2005. *Top right:* The associated power spectrum; the dashed line indicates a theoretical random walk noise spectrum ($A_f \propto f^{\beta}$, $\beta = -2$). *Center and bottom:* The Scargle periodogram from UMRAO data (black curve) along with periodograms from KVN 22-GHz data (gray curves) for three consecutive days in November 2012. The sampling frequency of the periodograms is in units of day^{-1}. Again, the dashed lines indicate theoretical random walk noise laws.

For a deeper statistical analysis, we used 14.5-GHz long-term flux monitoring data taken from 1975 to 2005 by the University of Michigan Radio Astronomy Observatory (UMRAO) for comparison with our 22-GHz data sets (the UMRAO data are discussed in detail in Park & Trippe 2014). We calculated Scargle periodograms for all time series and normalized the power spectra from UMRAO and KVN data consistently in order to make them compatible; the results are shown in Figure 2.5. We compare the observed

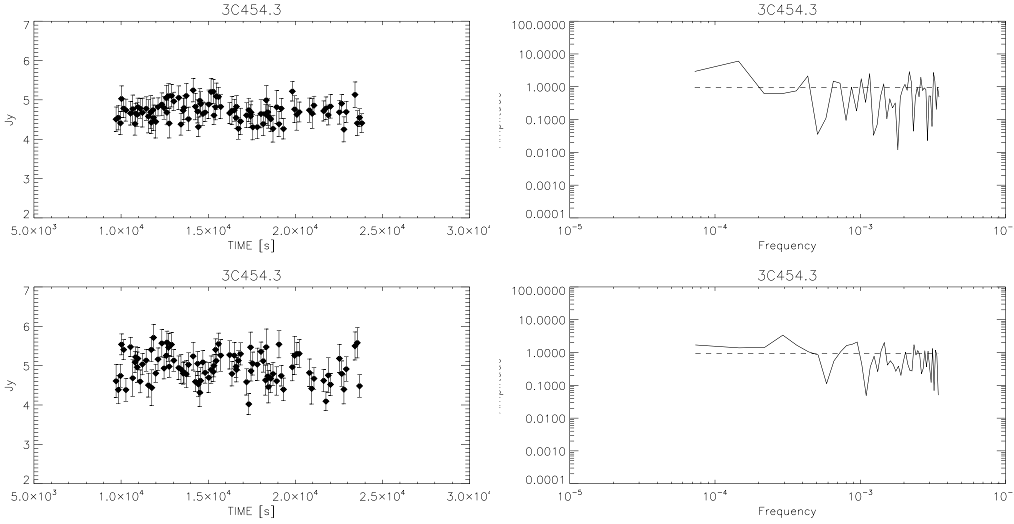

Figure 2.6. Lightcurves (left panels) and Scargle periodograms (right panels) of 3C 454.3 observed in April 2013. *Top:* 22 GHz. *Bottom:* 43 GHz. The sampling frequency of the periodograms is in units of s^{-1}.

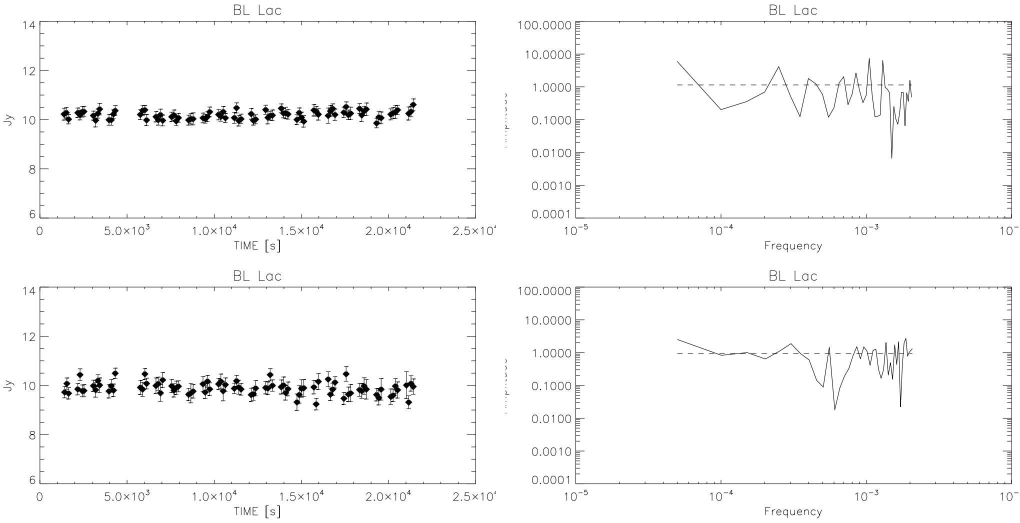

Figure 2.7. Lightcurves (left panels) and power spectra (right panels) of BL Lacertae observed in April 2013. *Top:* 22 GHz. *Bottom:* 43 GHz. The sampling frequency of the periodograms is in units of s^{-1}.

power spectra to a theoretical random walk noise ($\beta = -2$) law which appears to be a generic feature of blazar power spectra (Park & Trippe 2014); the flat tail of the UMRAO power spectrum is due to known sampling effects. As it turns out, all KVN power spectra are located above the theoretical line by several orders of magnitude.

2.5.3 3C 454.3

In April 2013, 3C 454.3 provided moderately sampled light curves (Figure 2.6) with relatively large error bars at both 22 and 43 GHz. The m and reduced χ^2 values are comparable to the 43 GHz data for 3C 111 of February 2013. With short observing times and large scatter, the lightcurves lead to high upper limits on brightness temperature.

2.5.4 BL Lac

BL Lacertae was observed on the same day as 3C 454.3 for a somewhat longer time. Though the sampling of the light curves at 22 and 43 GHz is only moderately dense, the light curves are the flattest among all our sources: reduced χ^2 values are 0.6 and 0.9, m indices are 1.6% and 2.5%, respectively.

2.6 Discussion

Despite our efforts and a high time resolution of few minutes, we have not found indication for distinct intra-day variability in our target sources. On time scales from minutes to hours, the source fluxes did not change more than a few percent, the light curves are flat.

The modulation indices range from 1.6% to 7.6% depending on source and epoch. These values are comparable to or slightly higher than those in the work by Kraus et al. (2003) or Gupta et al. (2012) in which the authors searched for and found, in part, variability in compact extragalactic radio sources. In our case, our relatively large m values are caused mostly by the photometric uncertainty. The lightcurves are characterized by scatter rather than systematic deviations from the mean, as expected

Table 2.5. The variability parameters.

Date	Source	Frequency [GHz]	Time[a]	m	${\chi_r}^2$	N[b]	${\chi^2_{r(<0.1\%)}}^{\mathrm{c}}$	T_b
2012 May	3C279	86	0.28	4.8	0.8	208	1.3	$< 2.1 \times 10^{17}$
2012 Nov	3C111	22	0.33	4.1	1.2	220	1.3	$< 3.5 \times 10^{15}$
			0.41	3.7	1.2	286	1.3	$< 1.9 \times 10^{15}$
			0.41	4.3	1.4	185	1.4	$< 2.1 \times 10^{15}$
2013 Feb	3C111	22	0.37	2.8	1.1	128	1.4	$< 2.7 \times 10^{15}$
			0.41	3.0	1.3	242	1.3	$< 2.3 \times 10^{15}$
			0.41	3.4	1.1	211	1.3	$< 2.8 \times 10^{15}$
		43	0.37	6.1	1.7	120	1.4	$< 1.5 \times 10^{15}$
			0.41	6.8	1.2	130	1.4	$< 1.2 \times 10^{15}$
			0.32	6.5	1.4	97	1.5	$< 1.8 \times 10^{15}$
2013 Apr	3C454.3	22	0.16	5.1	0.7	96	1.5	$< 2.9 \times 10^{18}$
		43	0.16	7.6	1.5	94	1.5	$< 1.1 \times 10^{18}$
	BL Lac	22	0.23	1.6	0.6	82	1.6	$< 1.8 \times 10^{16}$
		43	0.23	2.5	0.9	83	1.5	$< 7.2 \times 10^{15}$

[a] in units of day

[b] number of data points

[c] reduced χ^2 for a signal with a false alarm probability of 0.1%

for the case of source intrinsic variability.

Our χ_r^2 tests find values ranging from 0.6 to 1.8. These values are in agreement with no variation (for significance levels given by $\chi_r^2 \approx 1.4$ for a false alarm probability of 0.1%) in our lightcurves[6] (see also Table 2.5) – with the exception of one 43-GHz lightcurve of 3C 111 obtained in February 2013 which shows a fluctuation that is actually caused by an antenna pointing instability during the transit of the target. Overall, our lightcurves are in agreement with being flat within errors.

Even so, we were able to identify upper limits for flux variability and, at least formal, upper limits on brightness temperatures. As we did not find intrinsic variability, we used the scatter in a given lightcurve and its length in time as proxies for the amplitude of flux variations and the variability time scale. The resulting, rather loose, upper limits on brightness temperatures (10^{13} to 10^{18} K) exceed the Inverse Compton limit (10^{12} K) (Kellermann & Pauliny-Toth 1969) as well as the equipartition limit (3×10^{11} K) (Readhead 1994) by two to six orders of magnitude.

Physically, we are dealing with brightness temperatures in the *observer* frame, not with the intrinsic plasma temperatures in the *emitter* frame. Relativistic Doppler boosting leads to an upscaling of the *apparent* brightness temperature by the appropriate Doppler factor as given in Equation (2.6). Accordingly, our upper limits on apparent brightness temperatures can be translated into rather loose upper limits on Doppler factors ranging from about 20 to about 900.

This view is supported by the results of the periodogram analysis. Overall, all power spectra are consistent with white noise statistics ($\beta = 0$), in contrast to the known red noise behavior of AGN emission. From the power spectrum of 3C 111 we see that the KVN power spectra of three different days lie several orders of magnitude above the theoretical power-law line ($A_f \propto f^{-2}$). This suggests that our data are dominated by measurement noise and provide upper limits on the intrinsic variability only, which would have to be at sub-per cent level. We note however that it is not clear if the f^{-2}

---

[6] Calculated using the Internet χ^2 calculator provided by `www.fourmilab.ch/rpkp/experiments/analysis/chiCalc.html`

law is valid on time scales of minutes.

In our analysis, we have not followed flux variations on time scales longer than hours. 3C 279 had a high flux density of 28 Jy. 3C 111 showed different flux densities in November 2012 (2.8 Jy) and February 2013 (4.2 Jy), but we were not able to follow the trend since our observations covered two epochs only. This suggests that a more extended observations campaign with more observation runs at good weather might provide valuable insights on AGN variability in the – as yet poorly probed – time regime from hours to days.

In principle, binning of light curves in the frame of a statistical multi-scale analysis can provide additional information and enhance the chance of detecting variability, especially weak flares that span many scans in time but appear insignificant when studying the original light curve (Kim & Trippe 2013). However, in this case one has to sacrifice the time resolution which is critical in probing the shortest time scales of variability. As suggested by the periodiogram analysis, all our lightcurves are consistent with being white noise signals, meaning that the amplitude of variations is the same on all time scales – meaning that a binning of our light curves would not provide additional information.

2.7 Summary and Conclusions

We performed photometric radio single dish observations of four AGN – 3C 111, 3C 279, 3C 454.3, and BL Lac – using the three KVN 21-meter antennas at four different frequencies (22, 43, 86, and 129 GHz) in order to probe AGN intra-day variability. Observations were done in an "anti-correlated" pointing mode – with always at least one antenna of a pair of antennas pointing at the target – to construct long and undisrupted light curves which are of high importance in examining short time scale variability. In general, we achieved a time resolution of about one minute.

We were able to derive high-quality light curves for 3C 111, 3C 454.3, and BL Lacertae at 22 and 43 GHz, and for 3C 279 at 86 GHz, between May 2012 and April 2013. We found upper limits on flux variability ranging from ∼1.6% to ∼7.6%. The upper limits on the derived brightness temperatures exceed the inverse Compton limit by three to six orders of magnitude. From our results, plus comparison with data obtained by the UMRAO, we conclude that we have not detected source-intrinsic variability which would have to occur at sub-percent levels.

Chapter 3

The Radio and Gamma-ray Connection in the Jets of PKS 1749+096

3.1 Abstract

We present the results of 1.5-year-long KVN observations of a BL Lac object, 1749+096. In the radio band ranging from KVN 22 GHz to ALMA band3 100 GHz, the radio lightcurves show concurrent flares with the characteristic variability time scale of 1.4 yrs. 1749+096 went through a gamma-ray outburst in mid-2016 and had one of few follow-up flares at the end of 2017. Studying the correlation between the ALMA band 3 and Fermi-LAT lightcurves, we found that gamma-ray flare precedes the radio flare by 1.26 year. From the VLBA 43 GHz archival data, we could identify and track four jet components and the estimated apparent jet speeds are 4, 4.8, 5.8, and 9.7 *c*. The VLBA kinematics analysis revealed an evidence of an interaction between newly ejected jet component and the stationary component at the time of gamma-ray flare. We also probed the physical information of synchrotron self-absorption region during the flaring activity. From the radio flare rising timescale, we derived the variability brightness temperature, 4.7×10^{10} K, Doppler factor, 0.35, and the emission region size, 0.024

mas. Associated magnetic field strength of 0.11 G was obtained assuming synchrotron cooling of the region.

3.2 Introduction

Blazar radiation takes places across all the electro-magnetic spectrum and its characteristic spectral energy distribution (SED) has a shape of two-hump structure, the first hump ranges from radio to optical domain and is caused by synchrotron radiations. The second hump of the SED is due to the inverse Compton (IC) radiation and covers optical to gamma-ray regime.

The blazars take up most of the sources responsible for the γ-ray detection by Fermi-LAT observation in the extra-galactic sky above 10 GeV (Ajello et al. 2017). The origin of the gamma-ray radiation in the relativistic jets of blazar has been proposed to be mainly from broad line region (BLR) or down-stream of the jet (radio core). In the case of the BLR origin scenario, within sub-parsec distances from the central engine, the optical-UV photons are up-scattered by relativistic electrons in the jet via inverse Compton (IC) process (Sikora, Begelman & Rees 1994). Out further in the base of the relativistic jets, the external photon fields such as the dusty torus located parsecs away from the black hole or the jet itself provides the radio or thermal IR seed photons required for the IC scattering. Recently, Costamante et al. (2018) studied spectra of 106 Fermi-LAT gamma-ray broad-line blazars and found that BLR IC scenario is mostly disfavored. From the kinematic views, gamma-ray flares occur when a jet component is ejected from the radio core or interacts with other jet component (e.g. a stationary feature) (Jorstad et al. 2001a,b, 2014; Lee et al. 2019).

PKS 1749+096 (OT 081) is a low-synchrotron peaked BL Lac (LBL) object located at a redshift of 0.32 (Stickel et al. 1988) and is highly variable reaching a variability time scale of a few days in optical polarization (Lu et al. 2012; Uemura et al. 2017). It has a curved jet feature heading to the north-east direction on parsec-scale (Lister et al. 2019). The physical information such as Doppler factor of ~ 17.7, magnetic field strength of 1.5 G, bulk Lorentz factor, Γ of 10, viewing angle of $2.4 \sim 3^\circ$ was reported by Jorstad et al. (2017) and Ghisellini et al. (2011). From the observations of recent 10 years, its several jet components showed apparent super-luminal motions with speeds of 5 to 27c which is the fastest jet speed of BL Lac object observed by BU blazar group (Homan et al. 2001; Weaver et al. 2022; Jorstad et al. 2017). Lu et al. (2012) reported a common correlation between the emergence of VLBI components and radio outbursts at 15 GHz and a bi-modal distribution of super-luminal jet speeds.

A degree of linear polarization of 2.9 - 3.3 % was reported with the polarization angle of $\sim -50^\circ$ at 43 GHz radio core (O'Sullivan & Gabuzda 2009). The core polarization orientation is almost perpendicular to the jet at all frequencies of 4.6-43 GHz. They Also argued that the core region is highly self-absorbed but shows clear evidence of a spectral turnover feature at ~10 GHz. While Pushkarev (2001) estimated a large integrated rotation measure (RM) of 95 rad m^{-2} of the source, O'Sullivan & Gabuzda (2009) did not find significant non-zero RM during a flare at 43 GHz.

Since the first gamma-ray detection reported by (Abdo et al. 2009), there had been no notable gamma-ray activity until 2015, then after a long hibernation, unprecedented prominent outburst came out in 2016. Kim et al. (2018) carried out a multi-wavelength study of this strong outburst along with polarization information. They found that the flare coincided with the local maxima at longer wavelength light curves and confirmed the spectral hardening. Since the polarized knot propagated through the radio core after the outburst event, they concluded that gamma-ray flares are caused by the disturbance in the mm-wavelength core.

After the mid-2016 outburst, 1749+096 still intermittently shows ongoing mild gamma ray activity. In this work, we focus on the small gamma flare occurred at the end of 2017, as a part our multi-frequency blazar monitoring project `PAGaN` (the Plasma Physics of Active Galactic Nuclei) which uses Korean VLBI Network (KVN) and was initiated in the beginning of 2017. We have been observing in-total of ~30 bright blazars every month to account for their fast variabilities and aim to probe the physical properties of their relativistic jets in different polarization and frequency domain. For 1749+096, we investigate the temporal variability at radio and gamma-ray regime and test the correlations in the hope that we constrain the origin of gamma ray flares. Additionally, we use Atacama Large Millimeter Array (ALMA) archival data for time-series analysis and adopt VLBA data from BU Blazar group[1] to probe the details of jet kinematics at the time of the flares. We studied the flaring and spectral features to derive the physical parameters of synchrotron self absorption region of the jet.

Throughout the paper, we adopt a cosmology with $\Omega_m = 0.27$, $\Omega_\Lambda = 0.73$, and $H_0 = 71$ km s^{-1} Mpc^{-1}. The luminosity distance to the source is 1685 Mpc, the image scale is 4.64 pc/mas (Jorstad et al. 2017).

3.3 Observations and Data Analysis

3.3.1 KVN

KVN has capability of observing four frequencies simultaneously and we used dual polarization mode at two different frequencies each time. Every two epochs were scheduled to be 1-day separated from each other to ensure the quasi-simultaneous observation at different frequencies. For this 1749+096 study, observations from February 2018 to June 2019 were analyzed. The data cover total number of 15 epochs at the frequencies of 22, 43, 86, 94, 139 GHz. In total, we have seven epochs at 22 GHz, nine epochs at 43 GHz, six epochs at 86 GHz, five epochs at 94 GHz, one epoch at 139 GHz. At the frequency of 139 GHz, the source gets too faint to secure the required minimal signal to noise ratio. Dual-polarization observation data were recorded at 1 Gbps rate using the Mark 5B system and correlated using the DiFX software correlator at the Korea-Japan Correlation Center (KJCC) in Daejeon, South Korea (Yeom et al. 2009; Lee et al. 2015).

The data calibration process was carried out using Natonal Radio Astronomy Observatory (NRAO) Astronomical Image Processing System (`AIPS`) software package. Then the Caltech `Difmap` (Shepherd et al. 1994) software was used to construct the images. We set the natural weighting scheme for all epochs and de-convolved the images with `CLEAN` process, then repeated phase self-calibration was applied. After the `CLEAN`ed maps were constructed, we fitted circular Gaussian or point flux model components to the maps using the `modelfit` function (Jorstad et al. 2005) and extracted physical information of flux, size, etc. For the error estimation of the flux densities, we adopted a 10% of the flux density of each modelfit component following Kim et al. (2018), Homan et al. (2002).

---

[1] https://www.bu.edu/blazars/VLBAproject.html

3.3.2 ALMA

ALMA has publicly available calibrator catalogue[2] which consists of mostly bright quasars as their calibrator sources in the mm and sub-mm regime. In a special observing mode, the calibrators are observed and the data are automatically reduced via the ALMA pipeline. From the catalogue, we collected the data of band 3, 6 and 7 (at frequencies of 91.5, 103.5 GHz for the band 3, 233 GHz for the band 6 and 337.5, 343.5, 349.5 GHz for the band 7) spanning from 2017 to 2020. The total number of epochs are 269, 130, 18 at band 3, 6 and 7.

3.3.3 Fermi-LAT

The Fermi-LAT was launched in 2008 and scans the whole sky within a time period of ~ 3.2 hr in a survey mode (Atwood et al. 2009). We extracted the Pass 8 γ-ray data from the FSSC's website data server [3]. `SOURCE` class events of energy range from 0.1 to 300 GeV were selected with observation period spanning between 2017 January 1 and 2021 January 1 (MJD: 57754 - 59215). The data are calibrated by the standard "unbinned likelihood analysis procedure"[4]. We set the photon extraction radius (region of interest or ROI) of 10° centered at the source and included all the sources in the 4th LAT source catalog (4FGL) (The Fermi-LAT Collaboration et al. 2020) within the ROI. The maximum zenith angle of 90° was chosen, which is the LAT instrument team provided as the standard value, in order to avoid the *gamma*-ray contamination from the Earth's limb. For a selection of good time intervals, the filter of "`DATA_QUAL>0 && LAT_CONFIG ==1`" was selected as recommended by the LAT team. To manage the contamination from the background emission and the Galactic diffuse emission, the latest isotropic instrument response function (IRF) of `iso_P8R3_SOURCE_V3_v1` and `gll_iem_v07` were applied. For the significance of the source signal detection, a maximum likelihood test statistic (TS) value is computed. We set the minimum threshold of 9, which corresponds to a 3σ cut-off, so any flux values below this were rejected. To generate the light curve, the model parameters of all the sources located in the ROI are fixed as the catalogue values and the spectral parameters of the target source are left free. We set the binning intervals as 7 days for the whole time range as weekly or monthly time bins are widely used for gamma-ray analysis (Meyer et al. 2019).

---

[2] https://almascience.eso.org/alma-data/calibrator-catalogue

[3] https://fermi.gsfc.nasa.gov/cgi-bin/ssc/LAT/LATDataQuery.cgi

[4] https://fermi.gsfc.nasa.gov/ssc/data/analysis/documentation/

3.3.4 VLBA 43 GHz

We selected the fully calibrated 43 GHz (7mm) UV data from the Boston University blazar program [5] to take a deeper look into the source structure. The observation dates are from December 2017 to October 2020 and the obtained total number of epochs is 22. We model-fitted the calibrated visibility data with circular Gaussian or point model components as we did the same for the KVN data in section 3.3.1 using `Difmap` software.

3.4 Results

3.4.1 Multi-Wavelength Lightcurves

The spatial resolution of KVN is not high enough to resolve the source structure in detail. At all wavelength of 22, 43, 86, 94, and 139 GHz, only the core part is visible (see Figure 3.1) as the source is known to be quite compact and have little one-sided jet in the northern direction (Lu et al. 2012). Consequently, the one Gaussian model component fitted to the core takes up most of the total flux. At all four frequencies

---

[5] http://www.bu.edu/blazars/VLBA GLAST/1749.html

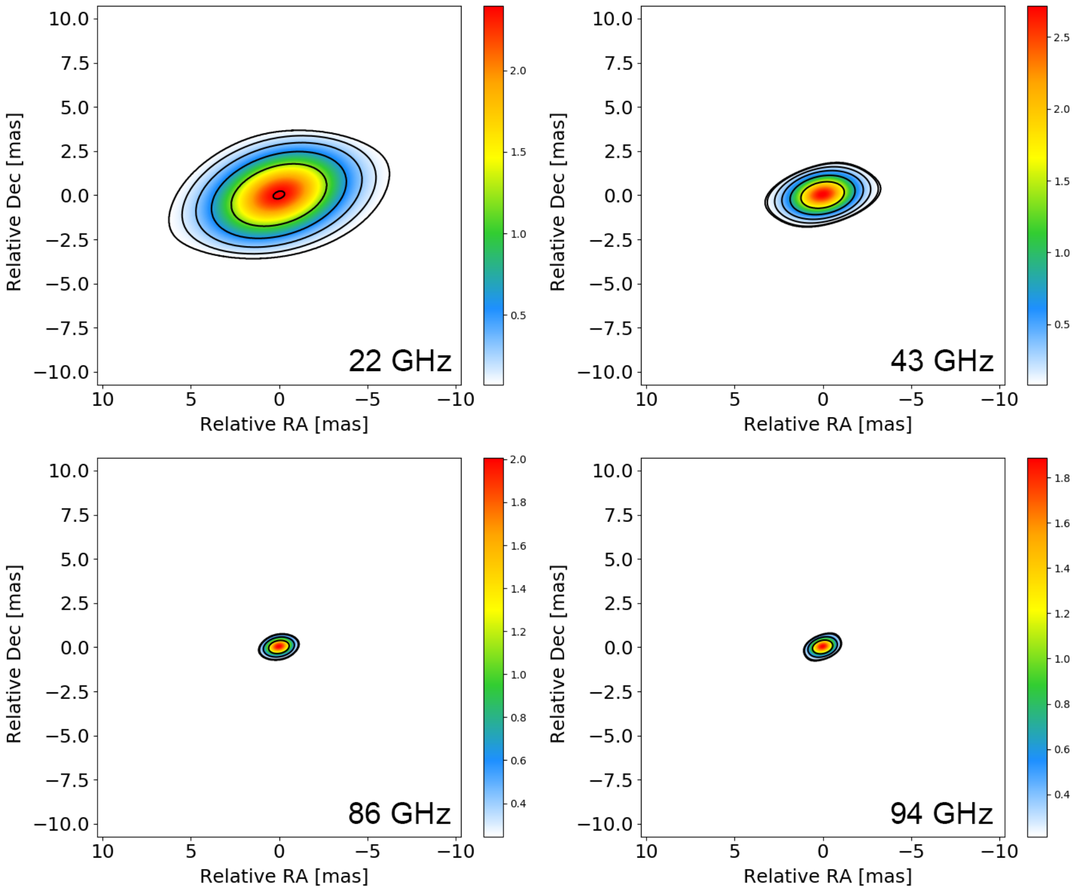

Figure 3.1. KVN images of 1749+096 at 22,43,86,94 GHz. The contour levels start at three times the rms noise value and increase in steps of 2.

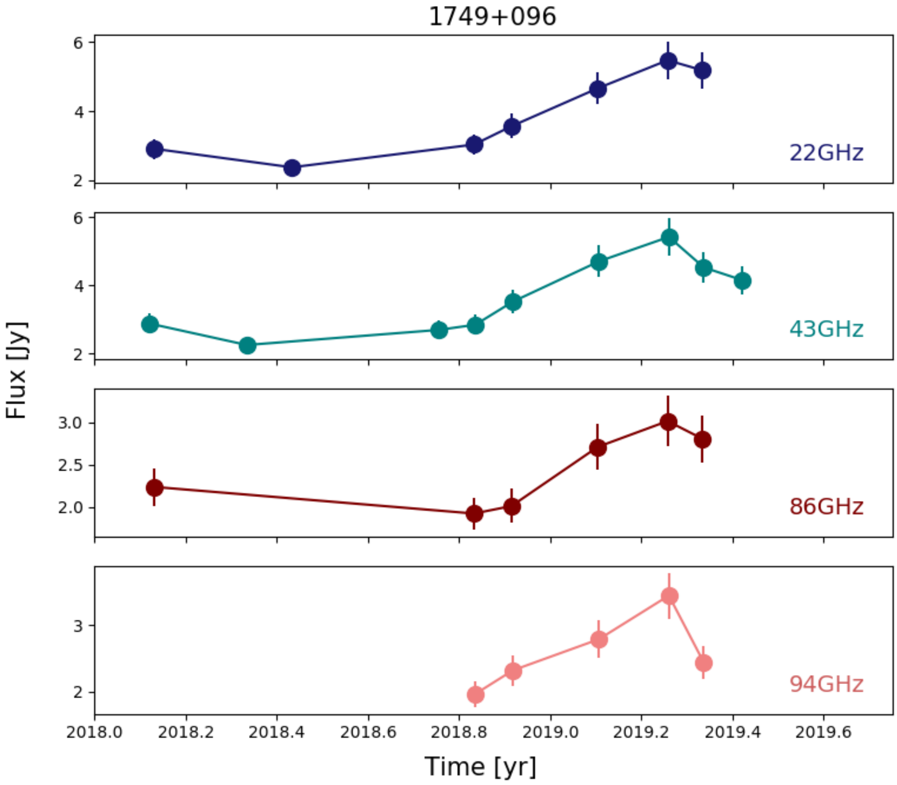

Figure 3.2. KVN lightcurves of 1749+096 at 22, 43, 86, 94, 139 GHz from top to bottom.

of 22, 43, 86, 94 GHz, the flux evolution indicates a small flaring feature: the light curves of the core flux shows increase from the middle of 2018 and seems to peak around 2019.25, then starts to decrease (see Figure 3.2). The flux at the peak exceeds two-times of the minimum flux value at the beginning. The spectral indices between 22-43 GHz are close to zero except the time of radio flare peak. Other spectral indices are all negative values and tend to decrease throughout the whole observation period.

ALMA light curves show similar trend to the KVN light curves but have much more data points to clearly exhibit the evolution of the flux measurement (see Figure 3.4). The light curves have local minima at the beginning of 2018 and peak around 2019.2, then decrease till the end of 2019. Then there is a small enhancement, but the flux value goes back quickly almost down to the local minima at the beginning of 2018. All

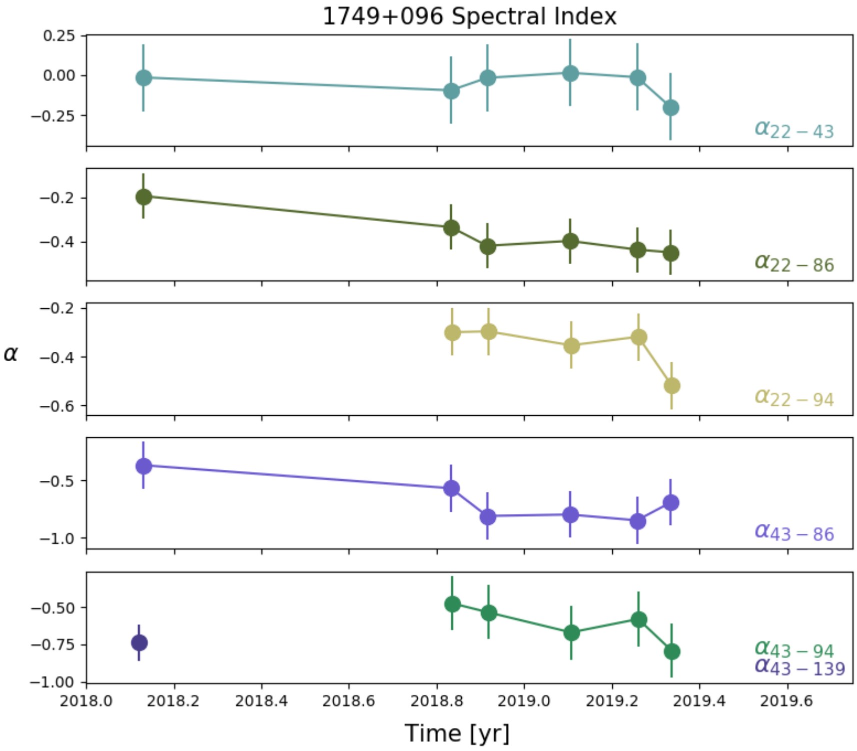

Figure 3.3. Spectral indices obtained from the four frequencies of KVN.

three different bands all look very alike except fewer number of data points at band 6. We chose the band 3 light curve for the further analysis which has slightly better flare feature than band 7 and much more data points than band 6.

After the mid-2016 outburst, 1749+096 exhibits occasional afterglows, as seen in the light curve, in the beginning of 2017, around the beginning of 2018, in the last quarter of 2020 (see Figure 3.5). The small flares reach almost 2 or 3 times the fluxes of the quiescent state and last for 0.35 years. for the further analysis, we interpolated the weekly-binned Fermi-LAT light curves and used it for the rest of the further work (see Figure 3.6).

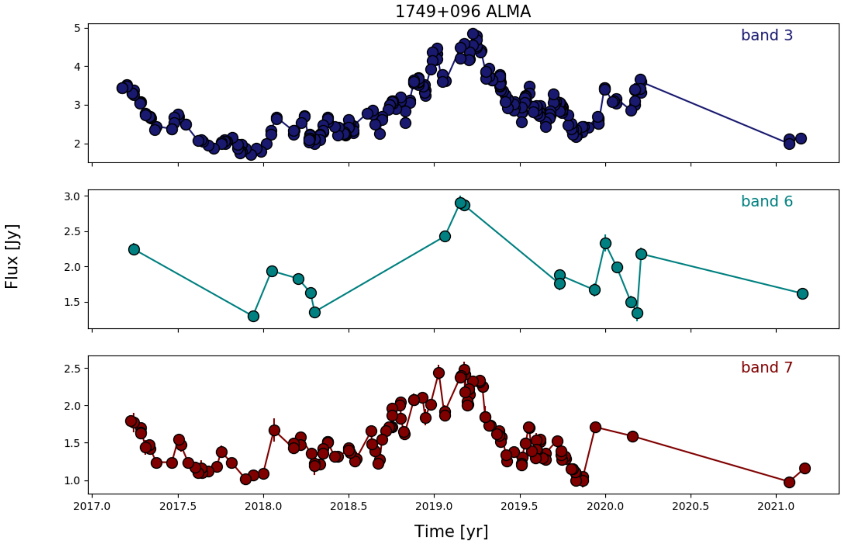

Figure 3.4. ALMA lightcurves of 1749+096 at band 3,6,7 from the top to bottom.

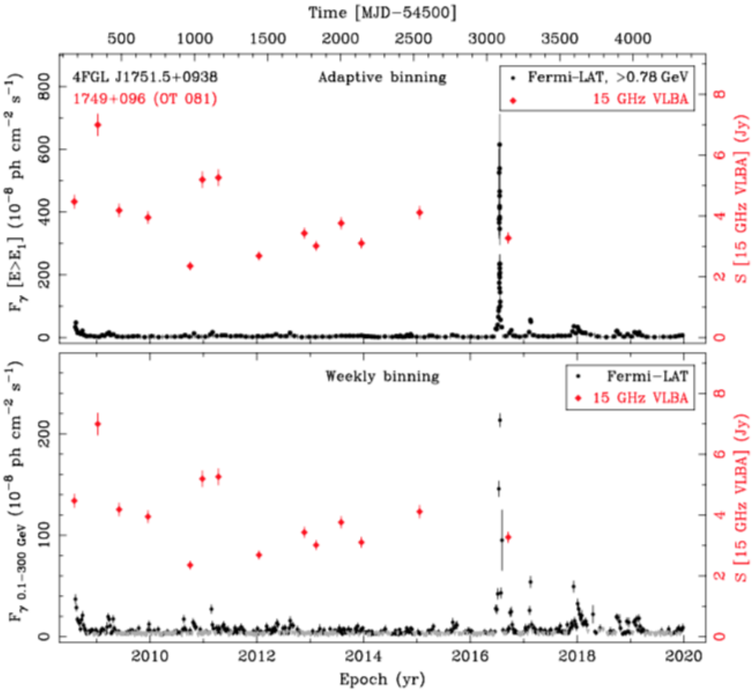

Figure 3.5. Fermi-LAT lightcurves of 1749+096 from 2009 to 2020. *Top :* Adaptive binning, *Bottom :* Weekly binning. Image by Fermi-LAT.

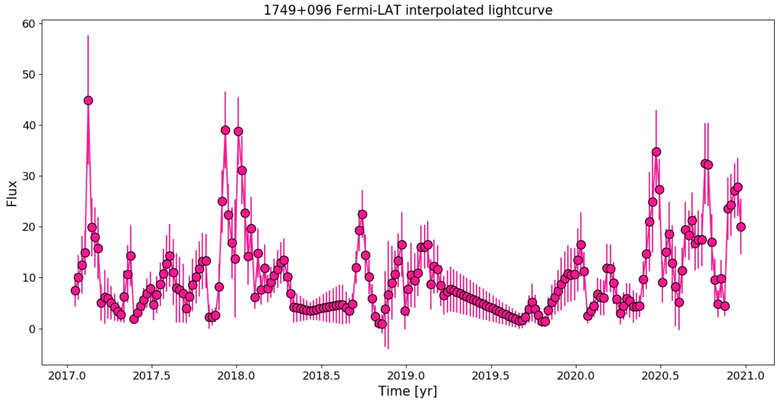

Figure 3.6. The interpolated weekly binned Fermi-LAT lightcurve from 2017 to 2021.

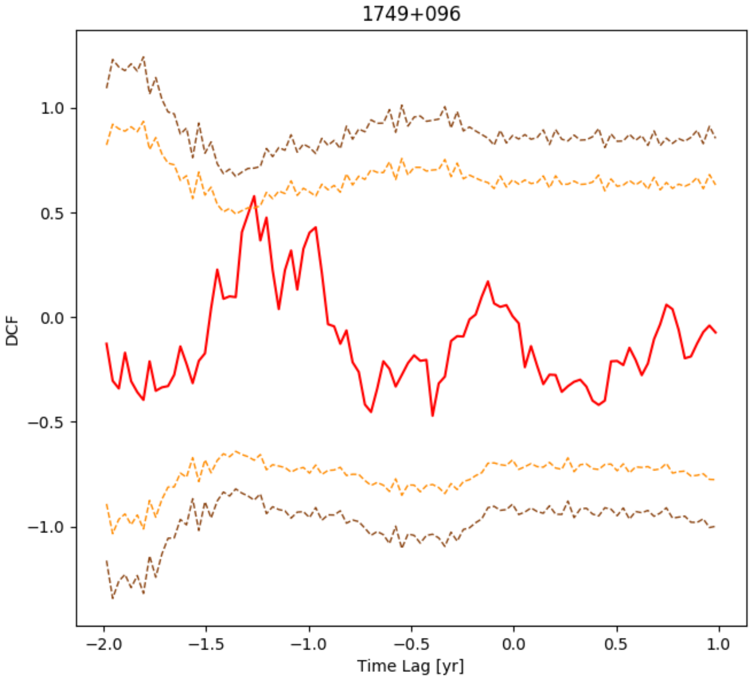

Figure 3.7. The DCF result between the Fermi-LAT and ALMA band 3 light curves. the brown and orange dashed lines indicate 99 and 95 % significance level respectively. The DCF peak is located at the time lag of -1.26 yr.

3.4.2 Correlation bewteen Radio and Gamma-rays

We used the DCF (Edelson & Krolik 1988) analysis between the gamma-ray and the ALMA band 3 light curves to test the correlation. In order to address the significance level of the DCF, we generated 10,000 artificial light curves following Emmanoulopoulos et al. (2013) and using DELCGEN code (Connolly 2015). We built the probability density function (PDF) and power spectral distribution (PSD) of the interpolated light curve. A log-normal function and a simple power-law were fitted to each distribution. Then we simulated light curves with the same PSD and PDF as the original light curve. Then we ran DCF on ALMA band 3 data with every simulated light curves and estimated the significance level from the distribution of the DCF values in each time bin. The result DCF is shown in Figure 3.7. The DCF peak exceeds the 95% significance level, and the estimated time-delay of the light curves is -1.26 yrs, indicating the gamma-ray flare precedes the radio flare.

With the time delay obtained with DCF analysis, we shifted the gamma-ray light curve by 1.26 year and checked the correlation (see Figure 3.8). The estimated Pearson's r coefficient is 0.5, with Spearman's coefficient is 0.4. It mildly supports the correlation between the two light curves.

3.4.3 Synchrotron Self-Absorption region

To derive physical information from the flaring event, we obtained the characteristic time scale via fitting an exponential function to the ALMA band 3 lightcurve using,

$$\mathrm{S(t)} = \begin{cases} S_{max} e^{(t-t_{max})/t_r}, & t < t_{max}. \\ S_{max} e^{(t_{max}-t)/1.3t_r}, & t > t_{max}. \end{cases} \tag{3.1}$$

where S_{max} is the maximum flux density in Jy, t_{max} is the time of the maximum amplitude of the flare, and the t_r is the flare rising time scale. We set the ratio of 1.3 between the the decay and rise timescale as Hovatta et al. (2009), Kravchenko et al. (2020). The fitted flare rising time scale is 1.4 yr, resulting in 1.82 yr for the decay time scale.

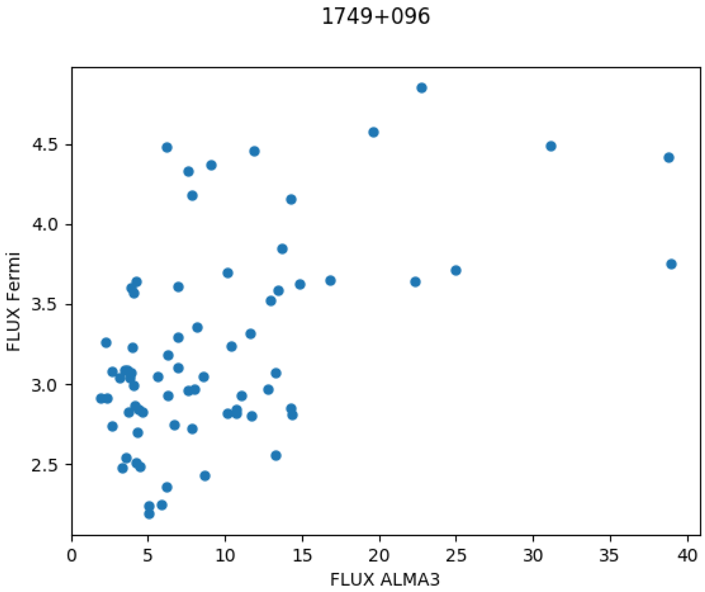

Figure 3.8. ALMA band3 and Fermi-LAT correlation. The Pearson's correlation coefficient is 0.5. Note that Fermi-LAT light curve was shifted by the value of correlated time delay, 1.26 yr for the analysis.

The variability brightness temperature of the emission region is derived using (Rani et al. 2013),

$$T_{b,var} = 3.47 \times 10^5 \Delta S \left(\frac{\lambda D_L}{\tau_{var}(1+z)^2} \right)^2 \tag{3.2}$$

where Δ S is the flux density variation in Jy during a variability time scale of τ_{var}, λ is the observation wavelength, D_L is the luminosity distance, and z is the redshift of the source. We adopt the distance of 1685 Mpc from Jorstad et al. (2017), and obtained the brightness temperature of 4.6×10^{10} K.

The variability Doppler factor is related to the variability brightness temperature and the intrinsic brightness temperature by,

$$\delta_{var} = (1+z) \left(\frac{T_{b,var}}{T_{IC}} \right)^{1/3} \tag{3.3}$$

which yields 1.3.

Then the size of the emission region is obtained via,

$$d = 0.173\frac{1}{D_L}\delta_{var}\tau_{var}(1+z) \quad [mas] \tag{3.4}$$

which gives 0.025 mas, using the image scale of 4.64 pc/mas (Jorstad et al. 2017), equals to 0.12 pc.

If cooling synchrotron plasma is concerned, then the cooling time scale is related to the magnetic field strength via (Rybicki & Lightman 1979),

$$\tau_{cool} = 7.74\left[\frac{\delta_{var}}{1+z}\right]^{-1}B^{-2}\gamma^{-1} \quad [s] \tag{3.5}$$

where γ is the electron Lorentz factor, which can be estimated if we consider a broken power law for the electron energy distribution by using the ratio of the peak frequencies of inverse Compton ($\nu_{\rm IC}$) and synchrotron ($\nu_{\rm syn}$) emission in the SED as (Beckmann & Shrader 2012). However, without the contemporaneous SED information, We adopt 10,000 for the γ as this is typical value for AGN and obtained the the value of the magnetic field strength of 0.11 G.

From the spectral energy distribution, we fitted the power law function (Algaba et al. 2018b),

$$S = C_1\left(\frac{\nu}{\nu_c}\right)^{C_2+C_3(\nu/\nu_c)} \tag{3.6}$$

where C_1 is the peak flux at the turn-over frequency, ν_c, and C_2 is the spectral index at the turn-over frequency, C_3 is a constant value. We obtained the turn-over frequencies of the emission region, ranging from 24 to 32 GHz (see Figure 3.9).

By assuming a compact emission region and a homogeneous synchrotron self absorption region, we can estimated the magnetic field strength using,

$$B_{SSA} = 10^{-5}b(\alpha)S_m^{-2}\theta^4\nu_c^5\left(\frac{\delta}{1+z}\right)^{-1} \quad [G] \tag{3.7}$$

where b(α) is a parameter ranging from 1.8 to 3.8 and dependant on the optically thin spectral index (see the table.1 in Marscher (1983)), θ is the size of the emission region. We adopt the b value of 1.8 and obtained the B_{SSA} ranging from 0.04 to 0.19 G.

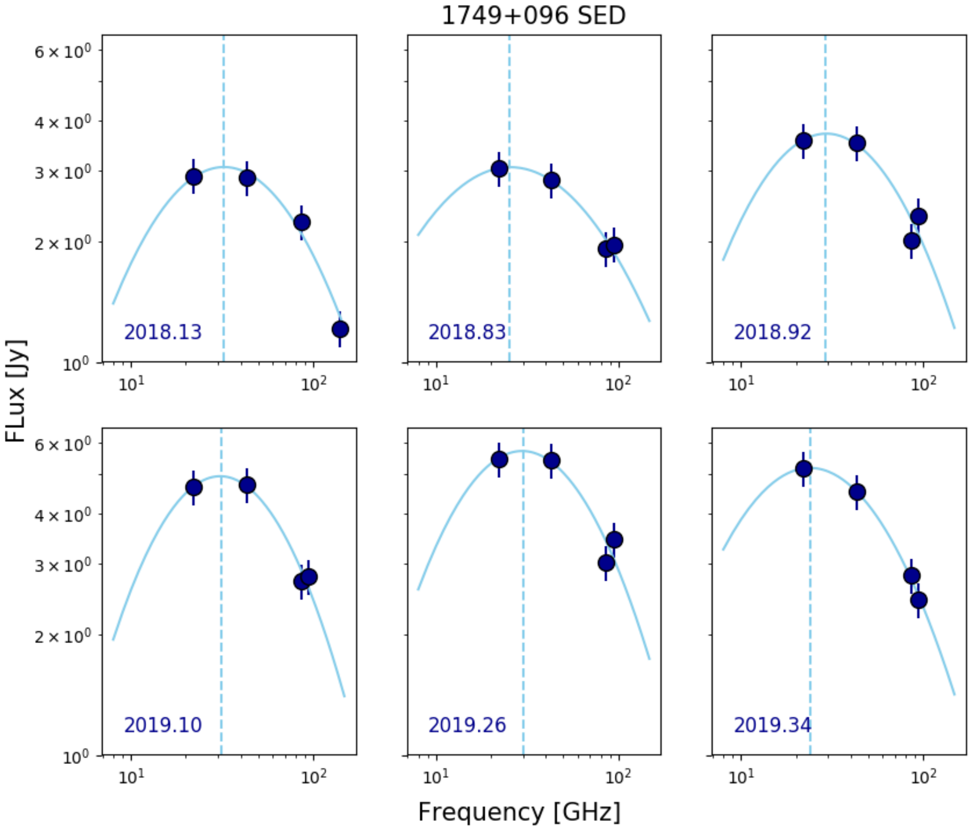

Figure 3.9. Spectral energy distribution at six epochs of KVN quasi-simultaneous data. Curved power-law function is fitted for turnover frequency. The obtained turnover frequencies range from 25.1 to 32.2 GHz.

Another way of addressing the magnetic field of the emission region is assuming that the particle and magnetic field energy densities are equal, then we can estimate the magnetic field strength via (Kataoka & Stawarz 2005),

$$B_{eq} = 0.25\eta^{2/7}(1+z)^{11/7}D_L^{-2/7}\nu_c^{1/7}S_m^{2/7}\theta^{-6/7}\delta_{var}^{-5/7} \quad [mG] \tag{3.8}$$

where η is the ratio of proton and electron energy density to the electron energy density. We take 100 as our η value following Pacholczyk (1970) and the obtained equipartition magnetic field strength are 2.4-2.9 mG.

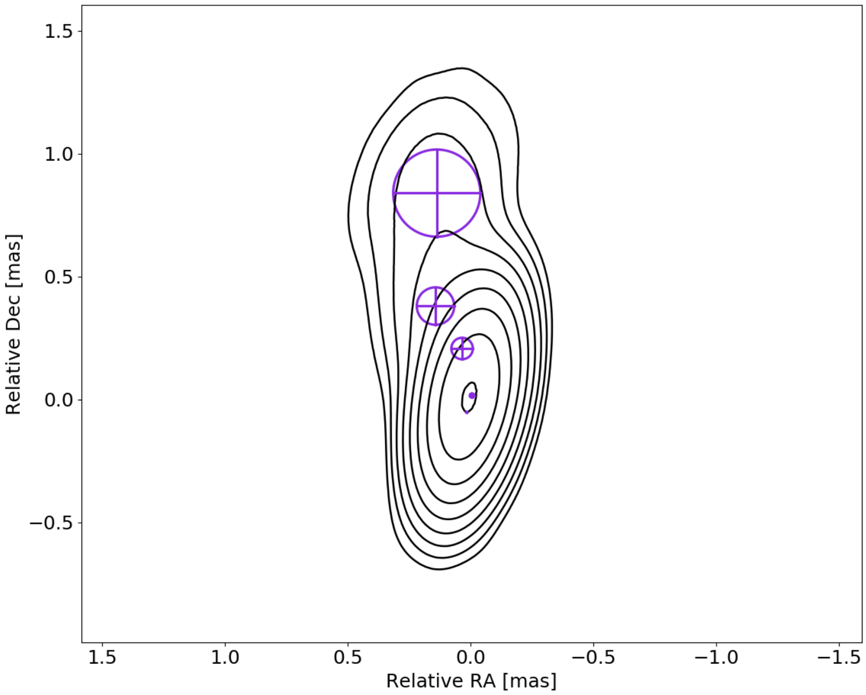

Figure 3.10. VLBA 43 GHz image in January 2020. The contour levels start at three times the rms noise value and increase in steps of 2.

3.4.4 VLBA 43 GHz

We constructed 22 VLBA images at 43 GHz from December 2017 to October 2020. A small one-sided jet feature toward the north and east-ward can be seen along with the

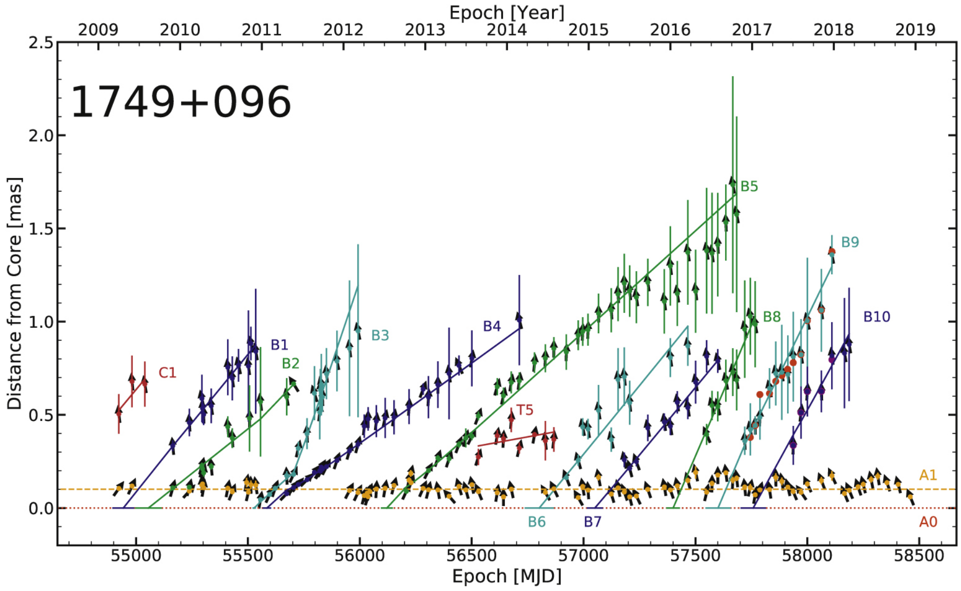

Figure 3.11. The kinematics result of VLBA 10-year-long observations by Weaver et al. (2022). A1 is the stationary component and B3 is the fastest component with apparent speed of $25c$. B10 component is identified and tracked as J1 component in our work. Figure from Weaver et al. (2022).

diffuse faint jet at ∼2 mas (see Figure 3.10). We could fit five to six jet components depending on the observation epochs, which mostly lie within 2 mas. We carried out the identification of the modelfit components in the jet from epoch to epoch, based on the consistency in the flux densities, separations from the core, position angles, and the sizes of the component (see Figure 3.12). We restrict the threshold by 1.5 mas from the core for tracking the jet component as Weaver et al. (2022) did, because the jet gets too faint to be identified further out. The errors of the flux density, σ_S, are set to be 10% of the flux of each modelfit component and the positional error, σ_D, are 20% of the beam-size (e.g. Homan et al. 2002). There is a stationary component located close to the core, which stays around at 0.2 mas in the early 2018 and later comes closer to the core. In total, we could track six jet components including a stationary component located around 1 mas from the core, which had already been observed by Weaver et al. (2022) from mid-2009 (see Figure 3.11).

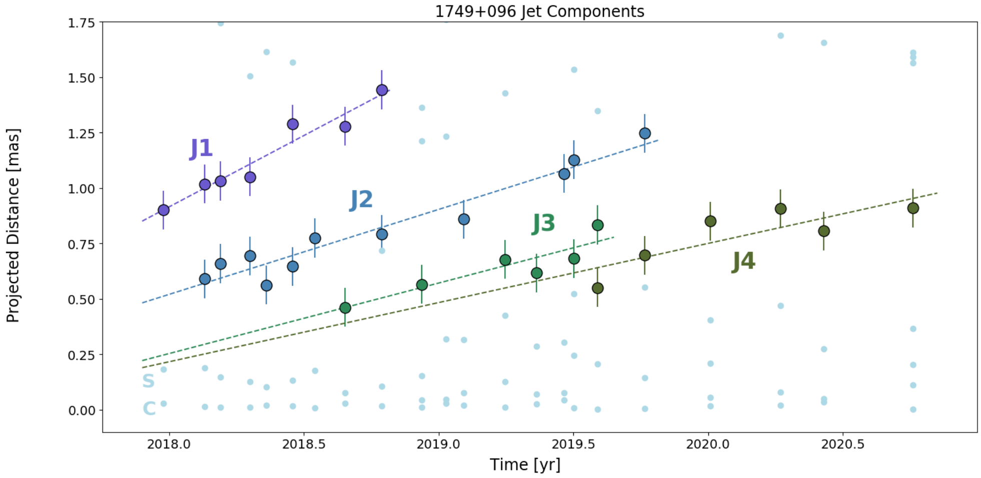

Figure 3.12. The radial distances of the jet components from VLBA observation. Four jet components, J1-J4, are identified and tracked. The light blue ones are the jet components which couldn't be traced. The jet components S and C denote the stationary and core component at the bottom.

We estimated the apparent jet speeds, β_{app}, from the radial distance plot, not taking position angles of the jet into account. The estimated βs are 9.7±1.1, 5.8±0.50, 4.8±1.1, 4.0±1.4 c for the J1, J2, J3, J4 respectively. The positions of the four jet components were extrapolated back to the zero separation from the core, and the obtained ejection times of the jet components J1, J2, J3, and J4 are 2016.58, 2016.64, 2017.20, and 2017.19. We fitted a linear line to the jet component locations and assumed constant speeds.

3.5 Discussion

The lightcurves by KVN observation at 22, 43, 86, 94 GHz show quite similar flaring features starting to go up from 2018 Spring and peaking in 2019 Spring. The ALMA lightcurves of band 3, 6, 7 also follow the similar manner with a slightly earlier start and exhibit a contemporaneous flares peaking in 2019.25. The overall radio light curves seem to be significantly correlated with each other at zero time lag, suggesting a concurrent radio flare. Such behaviors imply a co-spatial origin of the emission region, which is a rare picture in the blazar studies. Usually, the high frequency flux variations lead the low frequency variations (e.g. Rani et al. (2013); Chidiac et al. (2016); Karamanavis et al. (2016a)). ALMA data at band 3 and 7 have many data points enough to cover short variability, but KVN have sparse data points, owing to a month-long sampling rate, that a shorter time lag may exist.

The spectral index between 22 and 43 GHz is close to zero, indicating the source is opaque at that frequency range during the gamma ray flare period. The similar states were earlier observed in this source by Kim et al. (2018); O'Sullivan & Gabuzda (2009), where they found 15-43 and 12.9-43 GHz pair spectral indices being almost zero near the core region. Also, Algaba et al. (2018a) found from their work on 1633+38 that the radio spectral indices are correlated with flux densities: the higher the flux densities are, the larger the opacities in the source become. In the other pairs, the spectral indices are less than zero indicating the emission region is optically thin.

The gamma ray peaks at the starting point of a rise at the radio band, which is a conventional picture of the radio and the gamma ray connection (Orienti et al. 2013; Max-Moerbeck et al. 2014) and even at the time of the gamma flare, the radio flux seems to jump a bit during a rising phase. There are also opposite examples of studies in which the gamma-ray flares occur simultaneously with radio flares (e.g. Wehrle et al. 2012; Lico et al. 2014). While the previous work on 1749+096 by Kim et al. (2018) reported relatively weak radio counter parts on the mid-2016 gamma-ray outburst, the gamma-ray flare in the beginning of 2018 showed strong radio counter parts.

From the almost two-year-long VLBA archival observation data, we could track four jet components located within 1.5 mas from the core. For the outermost identified jet component J1, the location and apparent speed are consistent with the B10 component in Figure 3.11 within errors. The estimated β_{app} values are 4, 4.8, 5.8, and 9.7 c for the J1, J2, J3, J4 (from the outer to the inner jet) respectively. Lu et al. (2012) reported that the apparent jet speeds of 1749+096 have bi-modal distribution, faster ones with $\sim 20c$ and slower ones with $\sim 7c$ from 1996 to 2006 observations at 15 GHz. Similar

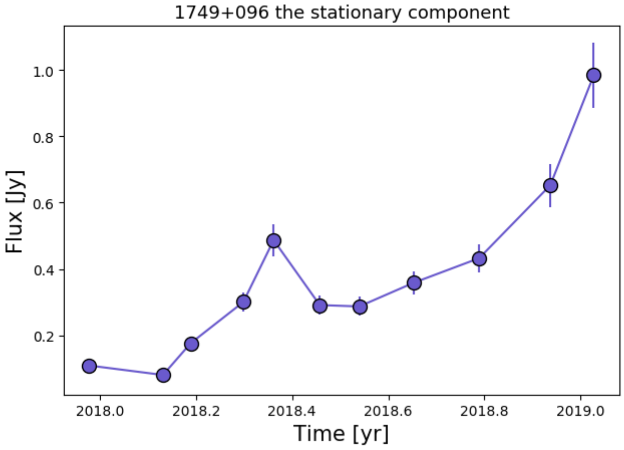

Figure 3.13. VLBA 43 GHz flux density variation of the stationary component, S, at 0.2 mas. The flux density started to rise after the beginning of 2018 gamma-ray flaring activity

distribution was also found in the work by Weaver et al. (2022), the jet speeds are either $\sim 10c$ or $\sim 20c$ (except one large outlier of $27c$) from their observation at 43 GHz covering from 2009 to 2018. Our estimation falls within the slower part of the bi-modality and the higher speeds $\sim 20c$ are not found, which is general case for BL Lac objects showing lower apparent jet speeds than quasars (Jorstad et al. 2001a; Hovatta et al. 2009).

While the estimated ejection times of the jet components stretch back to 2016 and 2017, the J3 and J4 components appear to have interacted with the stationary component at the end of 2017. The stationary component tends to move little further from the core whenever a jet component comes out of the core region as can be seen in Figure 3.11, 3.12, then later moves back inside. This behavior might have resulted from the blending of the two interacting components. Also the flux density of the stationary component went up from 0.1 jy to almost 1 jy in a year since the interaction at the end of 2017 (see Figure 3.13). Further tracking of the flux was difficult since there seem to be another disturbance interaction.

When the unprecedented outburst came out in the mid-2016 analyzed by Kim et al.

(2018), the radio band showed relatively small variabilities. On the contrary, the small gamma-flare from the end of 2017 to the beginning of 2018 has radio counterpart at all the KVN bands and ALMA band 3, 6, 7. We have studied the correlation between ALMA band 3 and Fermi-LAT gamma-ray lightcurves and obtained a negative time lag, which indicates the gamma ray flare leads the radio flare as in earlier studies by Pushkarev,Kovalev & Lister (2010); Orienti et al. (2013); Meyer et al. (2019). The estimated delay of 1.26 year ($\sim$ 456 days) between the radio and the gamma-ray is unusually long regarding the statistical work by Liodakis et al. (2018), who studied 145 blazars with gamma ray and radio data and found the median time lags of $\sim$100-160 days.

The correlation between the gamma-ray and the radio band implies a common origin of the flares as shock-in-jet model suggests (Marscher & Gear 1985). According to this widely favored model, if a shock propagates along a relativistic jet and triggers both gamma-ray and radio emission, the time delay depends on the separation of the two emission regions (e.g. fig.3 in Max-Moerbeck et al. (2014)). In other words, the flaring origin is a region where it's optically thick at radio frequencies, only the gamma-ray is emitted. Then, the radio emission escapes once the shock has moved out where it's optically thin. As for our relatively large time lag of 1.26 year, the two-zone emission model should be exploited as Das, Prince & Gupta (2021) explained their time lag of 135 days. They carried out a broadband study on the FSRQ 4C+28.07 and found a radio-gamma correlation, and explained the time lag with the two-zone emission model in which the radio emission region is located several parsec downstream from the gamma-ray emission region in the jet.

From the kinematics analysis, the time of interaction between the jet component J3, J4 and the stationary component falls on the gamma-ray flare time. During the interaction, the location of the stationary component moved outward (not permanently) and after the interaction, the flux density grew up almost 10 times higher. Such behavior was not reported by Kim et al. (2018) from the mid-2016 gamma-ray outburst, they found the polarized component moving through the mm-core of the source. However, an ejection of a new jet component and the outward motion of the stationary component can be also seen at the time of the mid-2016 outburst in the Figure 3.11. Consequently, we suggest that a shock or disturbance propagating through the mm-VLBI core is responsible for the gamma-flare at the end of 2017 and beginning of 2018 as in Marscher et al. (2018); Wehrle et al. (2012); Jorstad et al. (2013)

We derived the variability brightness temperature of 4.6×10^{10} K, using the flux rising time-scale of $1.4\,yr$ obtained from the ALMA band 3 lightcurve. The associated variability Doppler factor, 0.35, is relatively small owing to the long variability time-scale. Lu et al. (2012) estimated δ values as 10.2–20.4 from the jet component they tracked from VLBI observations. The size of emission region is measured as 0.025 mas, which is comparable to the VLBI circular modelfit size of the core at 43 GHz. The magnetic field strength derived from synchrotron cooling time scale is 0.11 G, smaller than the value of 1.5 G Ghisellini et al. (2011) found based on the SED analysis.

Chapter 4

Jet Kinematics of the Quasar 4C +21.35 from Observations with the KaVA Very Long Baseline Interferometry Array[1]

4.1 Abstract

We present the jet kinematics of the flat spectrum radio quasar (FSRQ) 4C +21.35 using timeresolved KaVA very long baseline interferometry array radio maps obtained from September 2014 to July 2016. During two out of three observing campaigns, observations were performed bi-weekly at 22 and 43 GHz quasi-simultaneously. At 22 GHz, we identified three jet components near the core with apparent speeds up to $(14.4 \pm 2.1)c$. The timing of the ejection of a new component detected in 2016 is consistent with a γ-ray flare occurred in November 2014. At 43 GHz, we found four inner jet (<3 mas) components with speeds from $(3.5 \pm 1.4)c$ to $(6.8 \pm 1.5)c$. Jet component speeds tend to be higher with increasing distances from the core. We compared our

---

[1] Published in the Monthly Notices of the Royal Astronomical Society: Lee et al. 2019, MNRAS, 486, 2412

data with archival Very Long Baseline Array (VLBA) data from the Boston University (BU) 43 GHz and the Monitoring Of Jets in Active galactic nuclei with VLBA Experiments (MOJAVE) 15.4 GHz monitoring programs. Whereas MOJAVE data and our data are in good agreement, jet speeds obtained from the BU Program data in the same time period are about twice as high as the ones we obtain from the KaVA data. The discrepancy at 43 GHz indicates that radio arrays with different angular resolution identify and trace different jet features even when the data are obtained at the same frequency and at the same time. The flux densities of jet components decay exponentially, in agreement with a synchrotron cooling time scale of $\sim$1 year. Using known electron Lorentz factor values ($\sim$9,000), we estimate the magnetic field strength to be $\sim$1–3 μT. When adopting a jet viewing angle of 5°, the intrinsic jet speed is of order 0.99c.

4.2 Introduction

Active Galactic Nuclei (AGN) are the most powerful persistent astronomical sources and are marked, among others, by the ejection of relativistic jets of matter that reach kiloparsec to megaparsec scales in size. The detailed mechanisms of ejection and collimation of these powerful jets are only partially understood, even though there has been progress in understanding them both observationally and theoretically in recent years (see, e.g., Komissarov et al. 2009; Boettcher et al. 2012; Mertens et al. 2016). Generally, the interaction of accreted matter, magnetic fields, and either black hole rotation or accretion disc rotation is supposed to launch a jet from the immediate vicinity (a few Schwarzschild radii) of a galactic supermassive black hole (Blandford & Znajek 1977; Blandford & Payne 1982).

According to the unified model of AGN (Urry & Padovani 1995), blazars are AGN whose jet axis is aligned with the line of sight within a few degrees. They are characterised by strong stochastic (red-noise type) variability across the whole electromagnetic spectrum, from γ-rays to the radio domain, on time scales from hours to years (e.g., Trippe et al. 2011; Gupta et al. 2012; Park & Trippe 2014; Aleksic et al. 2011).

Commonly, blazars are divided into two groups: BL Lacertae objects (BLO) and flat spectrum radio quasars (FSRQ) according to spectral features (e.g., Beckmann & Shrader 2012). Recent works by Ghisellini et al. (2011) proposed a more physical distinction based on the difference in accretion rates: FSRQs and FR II have disc luminosities higher than 5×10^{-4} of the Eddington luminosity, while BLOs and FR Is have disc luminosities lower than that. Further works expanded the classification by including the radio-loud galaxies. Meyer et al. (2011) suggested that radio-loud AGN are divided by source power: low synchrotron peaked sources whose jets do not show significant velocity gradients and high synchrotron peaked sources whose jets do show such gradients. As both types of structure are observed in AGN with low kinetic jet power, they suggested that the jet structure in those sources is controlled by the accretion rate in Eddington units, with the dividing line between the two source types being located between 3×10^{-3} and 10^{-2}. Sbarrato et al. (2014) also used a sample of blazars and radio-galaxies and found a smooth transition from radiatively inefficient to efficient accretion discs. Giommi et al. (2012) concluded from their Monte-Carlo simulations that there are only two intrinsic blazar types, low-ionization sources consisting mostly of beamed Fanaroff-Riley type I (FR I) galaxies and high-ionization sources of mostly beamed FR II ones. Xiong et al. (2015) also found an anti-correlation between jet power and beam-corrected synchrotron peak frequency of blazars and radio galaxies. Hervet et al. (2016) approached the blazar classification using very-long-baseline-interferometry (VLBI) maps, resulting in three classes with different radio knot kinematics.

The nearby FSRQ 4C +21.35 (PKS 1222+216), at a redshift of 0.433, is a compact lobe-dominated source (Wang et al. 2004) and located at the J2000 position $\alpha = $12h 24m 54.4584s, $\delta = +21^\circ\, 22'\, 46.389''$. This source displays super-luminal apparent jet motions with speeds ranging from $3c$ to $25c$ at milli-arcsecond scales as revealed by VLBI maps (Jorstad et al. 2001a, 2014; Lister et al. 2016; Jorstad et al. 2017). A large jet knot was ejected in the early 2000s and has kept its way along a bent trajectory since then (Homan et al. 2009). The bent trajectory is very different from the path of a jet knot ejected earlier; indeed, the two knots have been moving into different directions (Lister et al. 2013).

4C +21.35 also belongs to a small group of very-high-energy (VHE; $E > 100$ GeV) detected FSRQs along with 3C 279, PKS 1510–089, PKS 1441+25, S3 0218+35, and PKS 0736+017 (Cerruti et al. 2017). 4C +21.35 experienced two major γ-ray flares in April and June 2010. Multiple studies (Aleksic et al. 2011; Tavecchio et al. 2011; Nalewajko et al. 2014; Ackermann et al. 2014) aimed at finding the origin of the γ-ray radiation and at understanding the emission processes. Jorstad et al. (2014) used multi-frequency data including Very Long Baseline Array (VLBA) 43 GHz and *Fermi* Large Area Telescope (LAT) light curves and found a good correlation between γ-ray emission and radio kinematics. They showed that the γ-ray flare occurred when a newly ejected jet component moves through the core as well as a stationary feature near the core, which are assumed to be recollimation shocks. The time it took a moving knot to cross the stationary knot, and the epoch of the crossing, coincide with that of γ-ray flares.

So far, the VHE emission from FSRQs is usually understood as originating from a compact emitting region residing just outside the broad-line-region (BLR). The location is inferred from the absence of VHE photon absorption by BLR clouds (Boettcher & Els. 2016), and the small size is inferred from the rapid variability on time scales of a few minutes, thus implying physical extensions of less than a few light minutes (Tavecchio et al. 2011). Ackermann et al. (2014) constructed a theoretical spectral energy distribution (SED) of the source using a one-zone leptonic model in which a small emission region (with a radius of $\sim 10^{15}$ cm) resides outside the BLR. The resulting SED model, which is fitted to multi-frequency data, has a characteristic two-hump ("camel back") structure, with the first hump (from radio to optical) being caused by synchrotron radiations and the second (from optical to γ-rays) being due to inverse Compton radiation. Synchrotron self-Compton (SSC) radiation supposedly dominates the spectrum in the X-ray regime, external Compton (EC) emission dominates the γ-ray spectrum.

In this work, we aim at a detailed characterization of the kinematics of 4C +21.35

as well as illuminating the connection between kinematics and γ-ray activity. Since 4C +21.35 shows ongoing vigorous γ-ray activity and blazars are famous for their fast variability, persistent and frequent monitoring of the source structure is essential. We therefore studied the kinematics of the jet of 4C +21.35 with bi-weekly radio interferometric mapping observations, providing an unprecedented density of data.

We used the Korean VLBI Network (KVN) and VLBI Exploration of Radio Astrometry (VERA) array (KaVA; for detailed information, see Niinuma et al. 2014; An et al. 2016; Zhang et al. 2017; Cho et al. 2017; Kino et al. 2018) at 22 and 43 GHz from 2014 to 2016. We follow up on an earlier study by Oh et al. (2015) who observed eight radio-bright AGN with KaVA over one year. We compare our results with archival VLBA data from the Boston University Blazar Monitoring program at 43 GHz and Monitoring Of Jets in Active galactic nuclei with VLBA Experiments (MOJAVE) at 15 GHz that approximately cover the time span of our observations.

Throughout the paper, we adopt a cosmology with $\Omega_m = 0.27$, $\Omega_\Lambda = 0.73$, and $\mathrm{H}_0 = 71$ km s^{-1} Mpc^{-1}. The luminosity distance to the source is 2.4 Gpc, the image scale is 5.6 pc/mas (Jorstad et al. 2017).

4.3 Observations and Data Analysis

4C +21.35 was observed during a KaVA monitoring campaign of M87 (Hada et al. 2017). During the allocated epochs, observations were performed bi-weekly and quasi-simultaneously at 22 and 43 GHz, with a separation of one day between the two frequencies (when both were available). Observations at 22 GHz started in September 2014, followed by joint 22 and 43 GHz observations from May 2015 on. Continuous bi-weekly observations began in 2016. In total we obtained thirteen epochs of data for 4C +21.35 at 22 GHz and eleven at 43 GHz (see Table 4.1 for an overview). Angular resolutions (beam sizes) are on average 1.2×1.1 mas and 0.8×0.6 mas at 22 and 43 GHz, respectively. The on-source time is 70 minutes on average, the data are recorded at a rate of 1Gbps with 2-bit sampling: 16 IFs with a bandwidth of 16 MHz per IF were used in 2014, 8 IFs with a bandwidth of 32 MHz per IF were used from 2015 on. Only left-hand

Table 4.1. Overview of our KaVA observations.

Year	Month	Date	Frequency [GHz]
2014	September	1	22
		14	22
	November	4	22
2015	May	3	22
		4	43
		16	22
		17	43
2016	February	25	22
		26	43
	March	9	22
		10	43
		20	43
		21	22
	April	8	22
		9	43
		21	22
		22	43
	May	3	22
		5	43
		23	22
		24	43
	June	2	43
		13	22
		15	43

circular polarization was observed. In mid-November 2014, a γ-ray flare from 4C +21.35 was detected by the *Fermi*–LAT. Our observation closest in time was performed in January 2015. All data were correlated at the Korea-Japan Correlation Center (KJCC) at the Korea Astronomy and Space Science Institute (KASI) (Oh et al. 2015; Lee et al. 2015).

We processed our KaVA data with the `AIPS` software package,[2] following the standard VLBI data reduction procedures. A-priori amplitude calibration was performed with the measured opacity-corrected system temperature and the gain curve of each antenna. Then, we ran the fringe-fitting process `FRING` to calibrate the visibility phases. We clipped out both the first and the last 50 channels (out of 1024 in total) to eliminate known band-edge artifacts. We constructed high resolution VLBI images with `DifMAP` (Shepherd et al. 1994) using natural weighting for all epochs. Using the `modelfit` task, we fitted circular Gaussian model components to the brightest features in the (u,v) plane; this choice reduces the number of free parameters and provides consistent positions over multiple epochs (Lister et al. 2009). We removed components that overlapped with others or had a best-fit size of zero. We stopped model fitting when the residual map became consistent with the noise level of ~1 mJy/beam.

The cross-identification of individual jet components from epoch to epoch is one of the key constraints on any kinematic analysis. In our case, thanks to the slow evolution of the jet structure with time and frequent observations, the cross-identification process was straightforward usually. We extracted the 2-dimensional position information of the jet components and checked that the variation of the position angles is less than 10°. We then tracked only the radial distances of the jet components from the core component, which we presumed to be stationary. We estimated flux density errors according to Fomalont (1999). We followed Lister et al. (2009) for estimating the errors on the best-fit positions of the Gaussian jet components: ~10 percent of the component size convolved with the beam size.

---

[2] `http://www.aips.nrao.edu/index.shtml`

4.4 Results

4.4.1 KaVA at 22 GHz

In our 22 GHz maps, 4C +21.35 has a compact straight jet extending up to 4 mas to the north (cf. Figure 4.1). In addition, we detect an extended structure ("blob") located about 10 mas north of the core, at a position angle of about 10° (counter-clockwise from north).

We identified three components in the inner jet and two in the blob. The middle component in the inner jet was excluded from our analysis – even though we detected it throughout the observations – because it showed significant, random position variations; what we observed is probably a blend of multiple components. The innermost component became visible in early 2016; accordingly, we suspect that it was blended with the radio core until then. This is supported by the fact that the peak flux density of the core decreased from 1.6 to 0.9 Jy from 2015 to 2016. All the jet components show linear outward motion; the further from the core, the faster they move (see Figure 4.2). The apparent speeds are $(6.3^{+11.9}_{-6.3})c$, $(10.8 \pm 1.4)c$, and $(14.4 \pm 2.1)c$ outward: For the newly ejected jet component, we could constrain only the upper limit of speed. Extrapolating the position of the newly emerged component (component C in Figure 4.1) back to zero distance from the core suggests an ejection in 2014.5 ± 3.4, assuming a constant component speed, consistent with the peak time of the mid-November 2014 γ-ray flare.

The 10-mas blob moved toward the north-east with an apparent speed of $(5.7{\pm}0.4)c$. Its flux density did not change significantly during our observations. The trajectories of the two jet components inside the blob are almost perpendicular to the jet orientation. This is consistent with previous MOJAVE observation results (Homan et al. 2009).

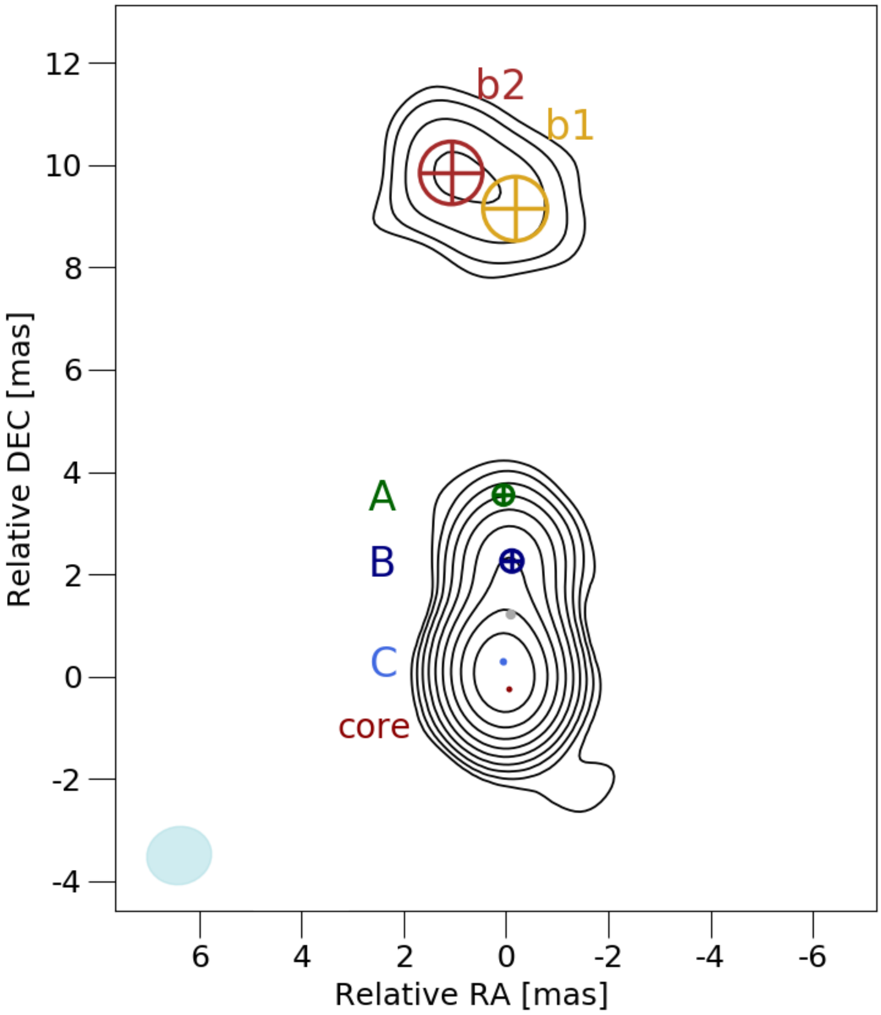

Figure 4.1. A 22 GHz KaVA image of 4C +21.35 in February 2016. The contour levels start at three times the rms noise value (0.64 mJy/beam), and increase in steps of 2. Circles labeled with letters mark identified jet components, the grey crossed circle is excluded from our analysis. The lightblue ellipse on the bottom left illustrates the CLEAN beam (1.27 mas × 1.13 mas).

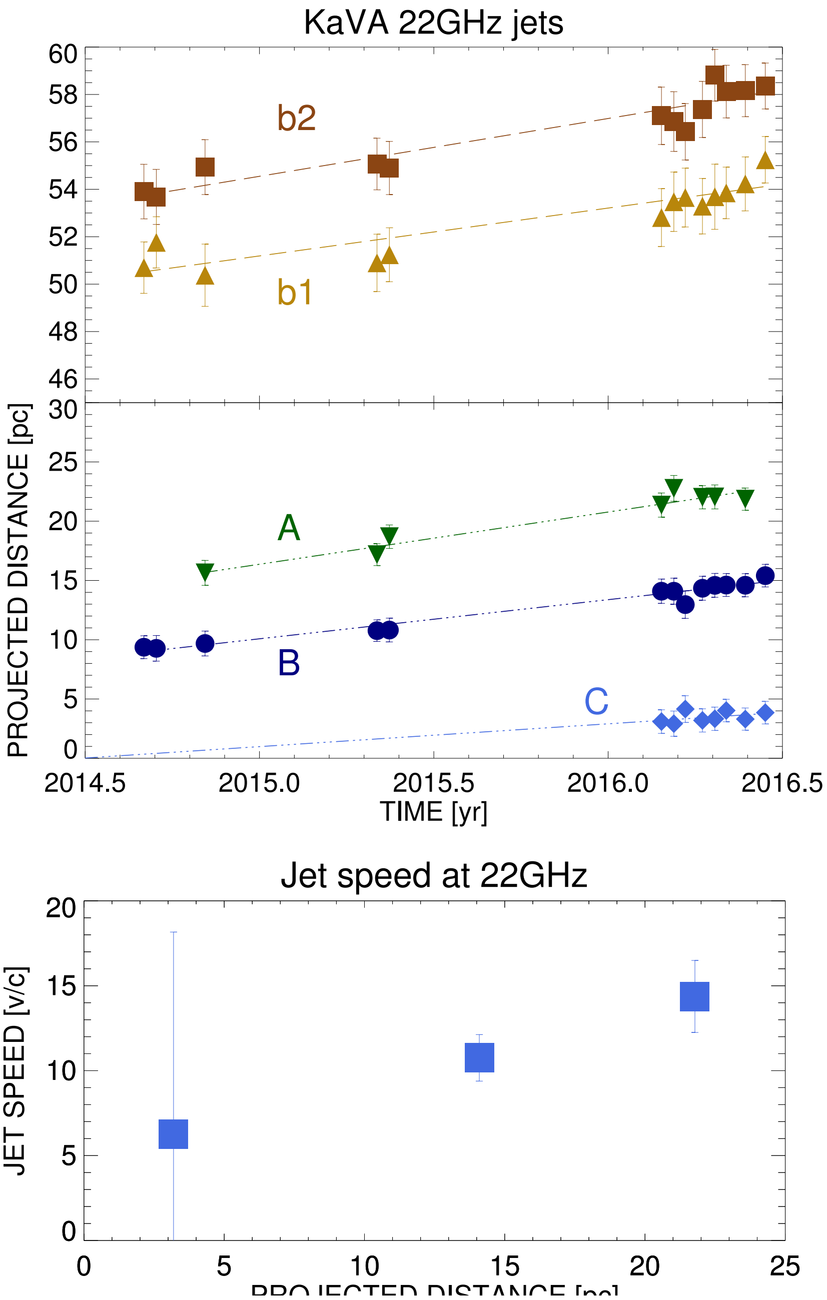

Figure 4.2. Jet kinematics derived from the 22 GHz KaVA maps. *Top panel:* Projected distance from the core as a function of time for all five jet components, separately for the outer components in the 10-mas blob (upper diagram) and the three inner jet components (lower diagram). *Bottom panel:* Apparent speeds of the three inner components as a function of projected distance from the core.

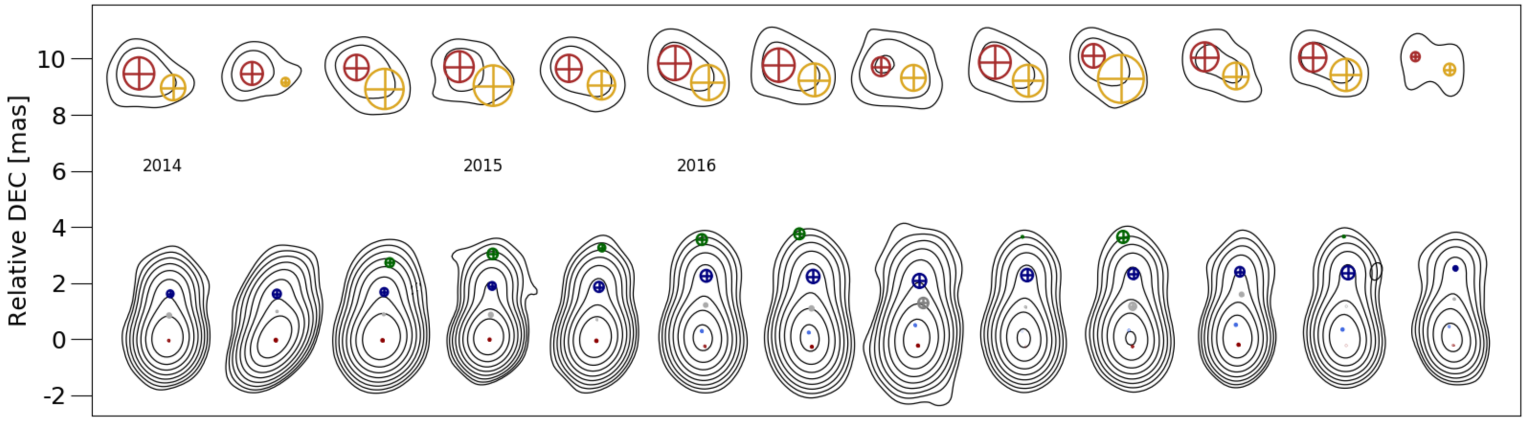

Figure 4.3. 22 GHz KaVA images from September 2014 to June 2016. The contour levels start at three times the rms noise value and increase in steps of 2. Jet component identification colors are same as Figure 4.1.

Table 4.2. Best-fit parameters for each Gaussian jet component, for the period of April 21–22, 2016.

Frequency [GHz]	ID	Flux [Jy]	Distance [mas]	Position angle [$\circ$]	Major axis [mas]
22	A	0.0058	3.7	4.6	0.43
	B	0.10	2.3	-2.3	0.38
	C	0.38	0.33	13	0.023
	b1	0.033	9.3	2.3	1.7
	b2	0.021	10	7.9	0.84
43	D	0.081	2.3	-1.5	0.58
	E	0.14	0.72	5.7	0.16

4.4.2 KaVA at 43 GHz

At 43 GHz, only the core and the inner jet of 4C +21.35 are visible; the 10-mas blob is too faint to be seen at this frequency (cf. Figure 4.4). The core peak flux dropped from 1 Jy to 0.5 Jy from 2015 to 2016, consistent with the observations at 22 GHz. We detected four jet components and could track two of them. The component closest to the core, at a distance of around 0.3 mas, seemed to be blended with the core. The component at around 1.7 mas showed no clear preferred direction of movement. We were not able to confirm the new knot whose appearance in 2015 Troitskiy et al. (2016) reported, or the stationary component located at 0.14 mas from the 43 GHz core. This is likely due to limited resolution since our maps show that the innermost component is located at ∼0.3 mas and exhibits random movements. Alternatively, it could have been short-lived and was not detectable when our observation re-started in the beginning of 2016.

The jet components moved outward monotonously throughout our observations (see

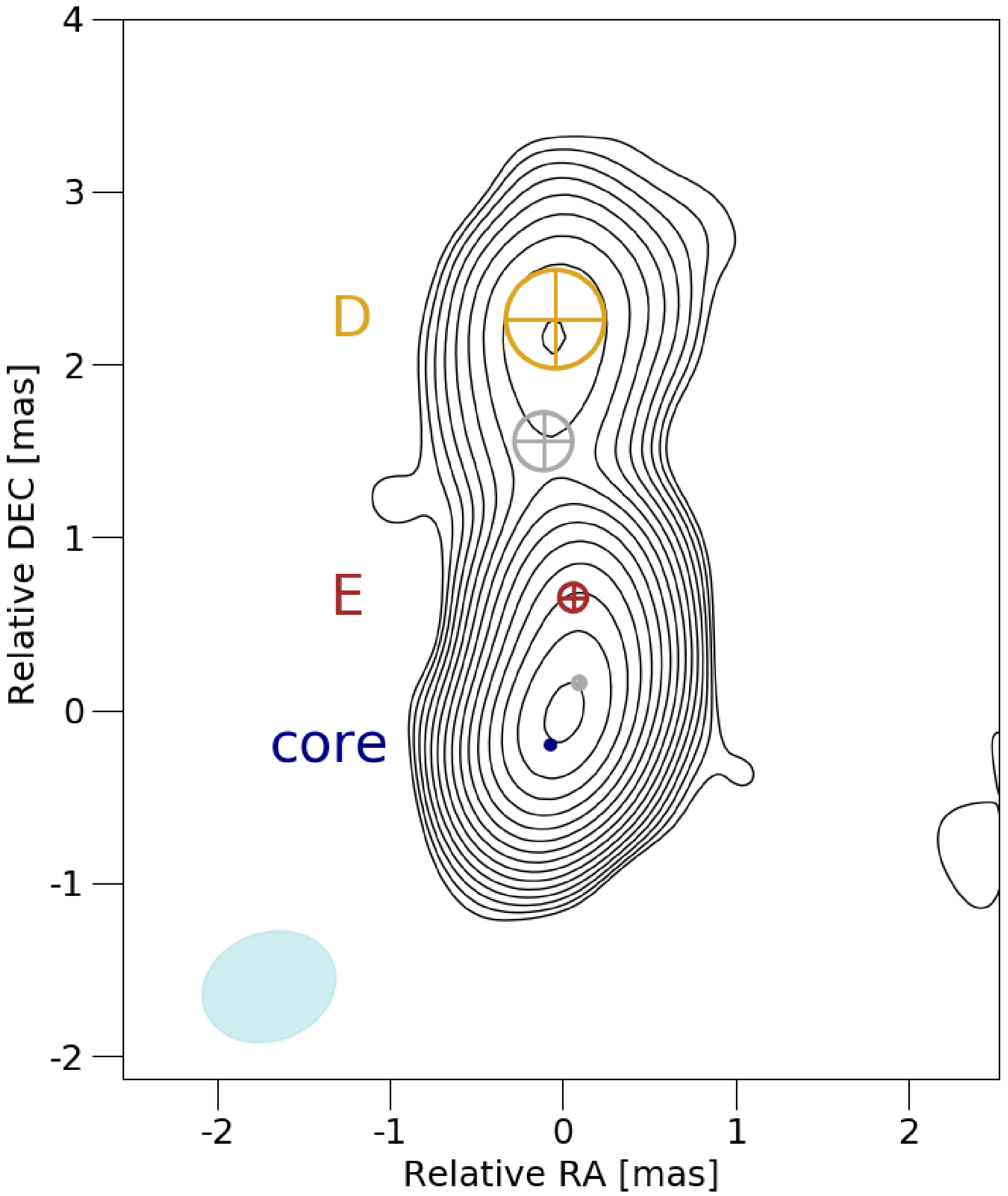

Figure 4.4. A 43 GHz KaVA image of 4C +21.35. The contour levels start at three times the rms noise value (1.14 mJy/beam), and increase in steps of $\sqrt{2}$. The two circles labeled with letters mark jet components that we were able to track reliably, the two grey crossed circles mark jet components we could not re-identity or track reliably. The CLEAN beam size is illustrated on the bottom left (0.79 mas × 0.63 mas).

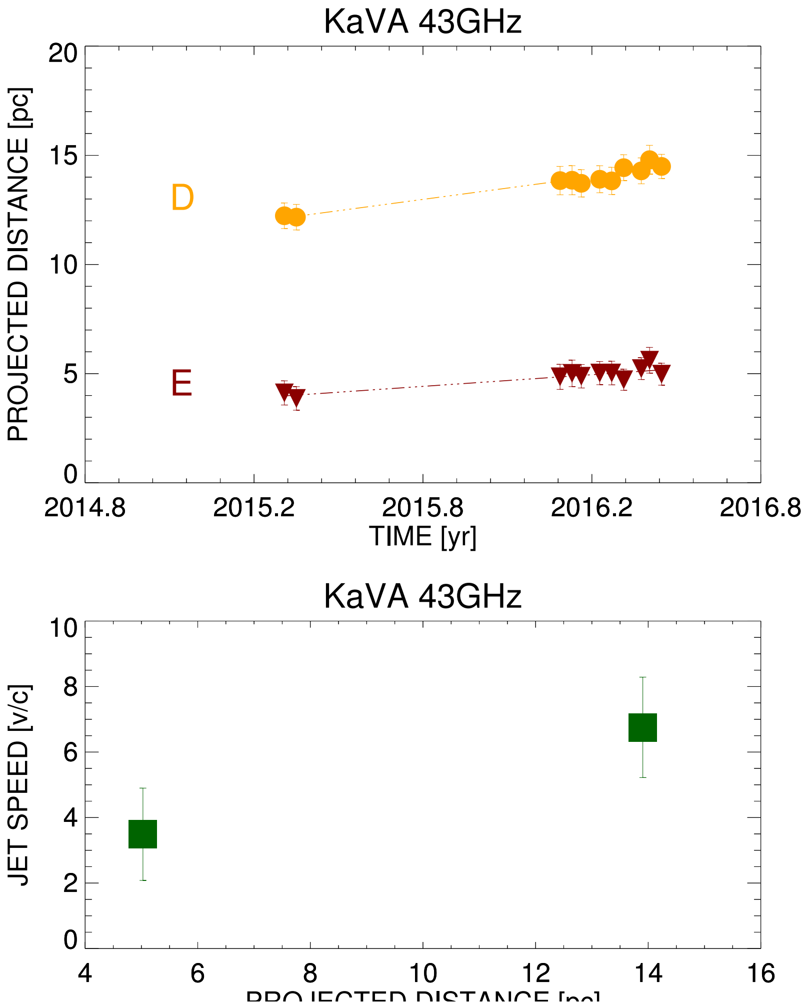

Figure 4.5. Jet kinematics derived from the 43 GHz KaVA maps. *Upper panel:* Projected distance from the core as a function of time for the two components we could track reliably. *Lower panel:* Apparent jet speed as a function of projected distance from the core for the two components shown in the upper panel.

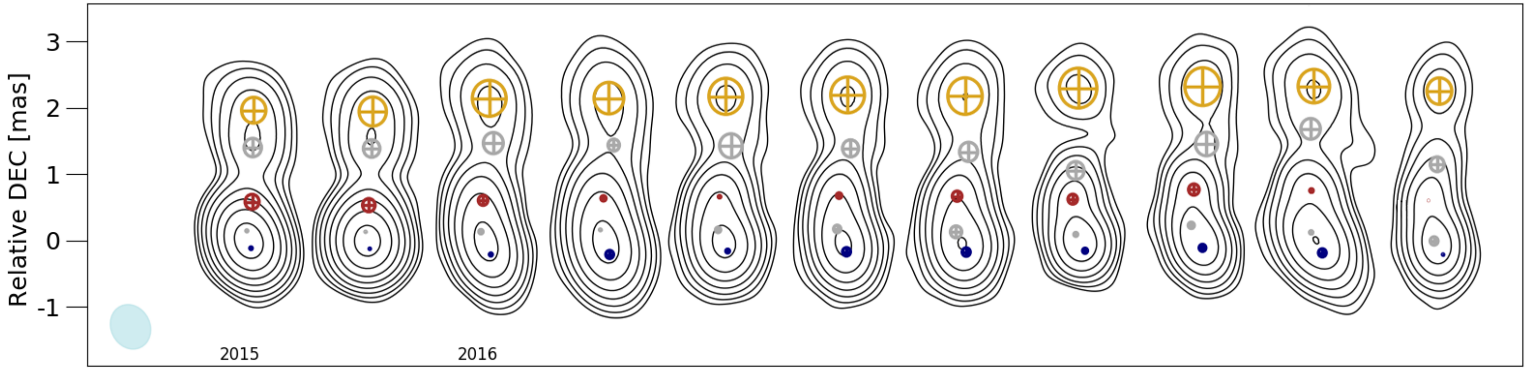

Figure 4.6. 43 GHz KaVA images from May 2015 to June 2016. The contour levels start at three times the rms noise value and increase in steps of 2. Jet component identification colors are same as Figure 4.4.

Figure 4.5). The flux density from the outer component decreased almost linearly, while the flux density from the inner component *increased* (cf. Figure 4.7). The apparent jet speeds are $(3.5 \pm 1.4)c$ and $(6.8 \pm 1.5)c$, respectively.

4.4.3 Intrinsic Jet Speeds and Doppler factors

The apparent (plane of sky) jet speed in units of speed of light β_a, intrinsic jet speed β, and viewing angle between the jet axis and the line of sight θ are related via

$$\beta = \frac{\beta_a}{\sin\theta + \beta_a \cos\theta} \ . \tag{4.1}$$

As we observe apparent jet speeds up to $13c$, we can infer that $\theta \lesssim 10°$, in agreement with the value $\theta \approx 5.3°$ reported by Pushkarev et al. (2017). Using the canonical value ($\theta = 5.3°$), we can derive intrinsic jet speeds of $(0.990 + 0.010)c$ to $(0.998 \pm 0.001)c$ at 22 GHz and $(0.978^{+0.007}_{-0.017})c$ to $(0.991^{+0.002}_{-0.004})c$ at 43 GHz. Consequently, the Doppler factors we obtain are 9.8, 10.2, and 10.8 at 22 GHz and 8.0 and 10.0 at 43 GHz. These values are consistent with the earlier findings by Pushkarev et al. (2017).

4.4.4 Flux Evolution and Synchrotron Cooling

Most of the jet components we observed with KaVA showed a steady decrease in flux density with time. Especially the three innermost 22 GHz jet components showed well-sampled decay light curves (cf. Figure 4.7). We described those with an exponential decay model

$$F = X \exp(-Yt) + Z \tag{4.2}$$

where t is the time, X, Y, and Z are constants, and $Y = 1/\tau$ with τ being the decay time scale. The best-fit decay time scales for each jet component are for A: 1.1 ± 0.2 yr, B: 1.9 ± 0.1 yr, C: 0.5 ± 0.04 yr at 22 GHz, and for D: 2.8 ± 0.8 yr at 43 GHz, respectively. Assuming that the flux decay results from synchrotron cooling, we may equate the decay time scale τ with the synchrotron cooling time scale $\tau_{\rm cool}$. For a relativistic plasma, where the electron energy distribution follows a broken power law, and considering the dominant synchrotron energy is emitted near the break frequency

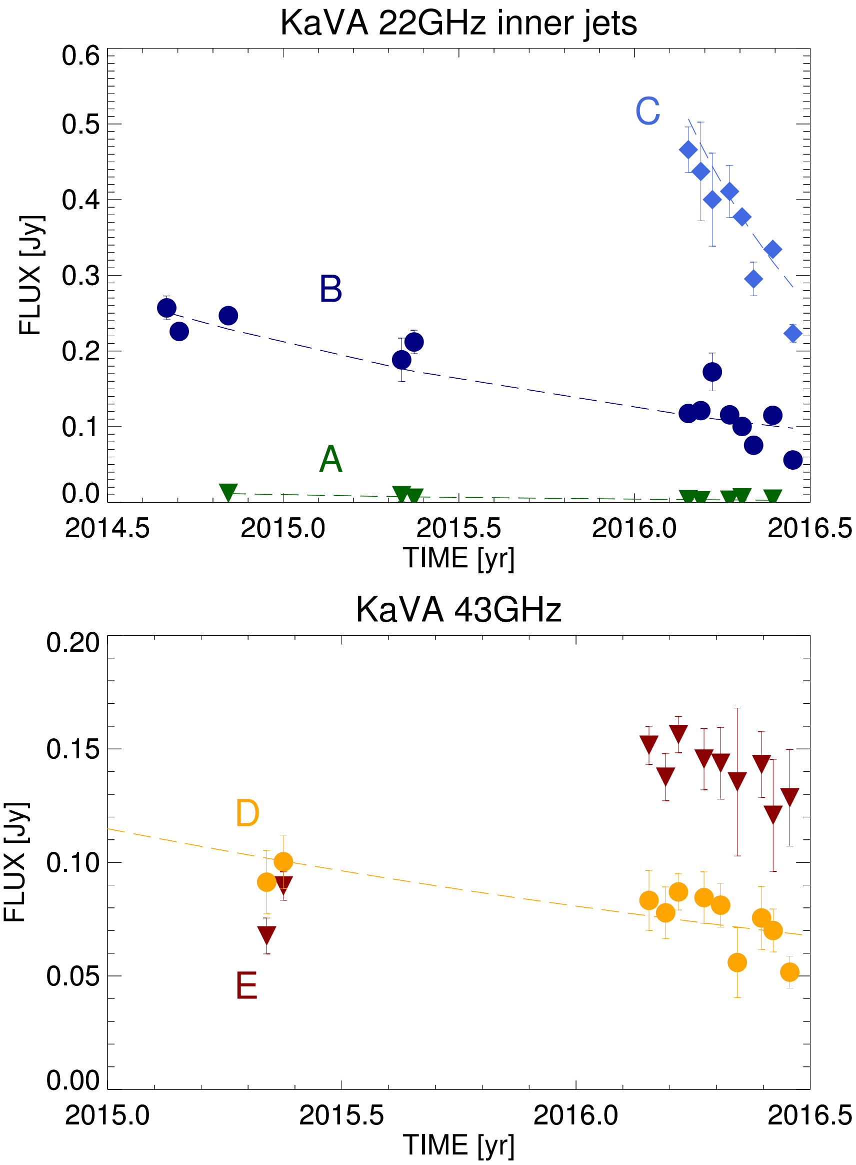

Figure 4.7. Flux evolution of KaVA jet components. *Top panel:* For the three inner jet components at 22 GHz. *Bottom panel:* For the two components at 43 GHz.

Table 4.3. The KaVA jet parameters.

Frequency [GHz]	ID	β_{app} [c]	β_{int} [c]	τ_{cool} [a] [yr]	δ[b]	B[c] [μT]
22	A	14.4	0.998	1.1	10.2	1.8
	B	10.8	0.996	1.9	10.8	1.4
	C	6.3	0.990	0.5	9.8	2.8
43	D	6.8	0.991	2.8	10.0	1.2
	E	3.5	0.978		8.0	

[a] flux cooling time scale

[b] Doppler factor

[c] magnetic field strength

in the electron spectrum, we can estimate the electron Lorentz factor γ from the ratio of the peak frequencies of inverse Compton ($\nu_{\rm IC}$) and synchrotron ($\nu_{\rm syn}$) emission like (Beckmann & Shrader 2012)

$$\gamma = \sqrt{\frac{3\nu_{\rm IC}}{4\nu_{\rm syn}}}\ . \tag{4.3}$$

For 4C +21.35, $\nu_{\rm IC} \sim 10^{24}$ Hz and $\nu_{\rm syn} \sim 10^{16}$ GHz (from Figure 9 of Ackermann et al. 2014), implying $\gamma \sim 9\,000$. For a cooling synchrotron plasma, we can connect the cooling time scale to γ and the magnetic field strength B via (Rybicki & Lightman 1979)

$$\tau_{\rm cool} = 7.74 \left[\frac{\delta}{1+z}\right]^{-1} B^{-2}\gamma^{-1} \quad \text{seconds.} \tag{4.4}$$

For a redshift $z = 0.43$ and a Doppler factor $\delta \sim 10$, cooling times in the range 0.5–2.8 years imply $B \approx 1 - 3\ \mu$T.

4.4.5 Spectral Index Maps

Since the 22 GHz and 43 GHz observations were performed quasi-simultaneously with one day separation between the frequency bands, spectral information is available. Our spectral index α is defined via $S_\nu \propto \nu^\alpha$. We obtained seven spectral index maps of the source using the `VIMAP` software routine (Kim & Trippe 2014): two in 2015 and five in 2016. However, 4C +21.35 is compact and core-dominated. Accurate alignment of maps obtained at two different frequencies requires alignment of the (presumably) optically thin jet at 22 and 43 GHz via spatial cross-correlation; in our case, only small parts of the source could be used. Even so, our spectral index maps managed to capture the smooth transition from a flat spectrum ($\alpha \approx 0$) at the core to a steep spectrum ($\alpha \approx -1$) at the very tip of the jet region, indicating that the core is optically thick while the jet is optically thin – as it was to be expected. Spectral index maps obtained at different epochs do not show significant differences; accordingly, we only present one of them in Figure 4.8 as a representative example.

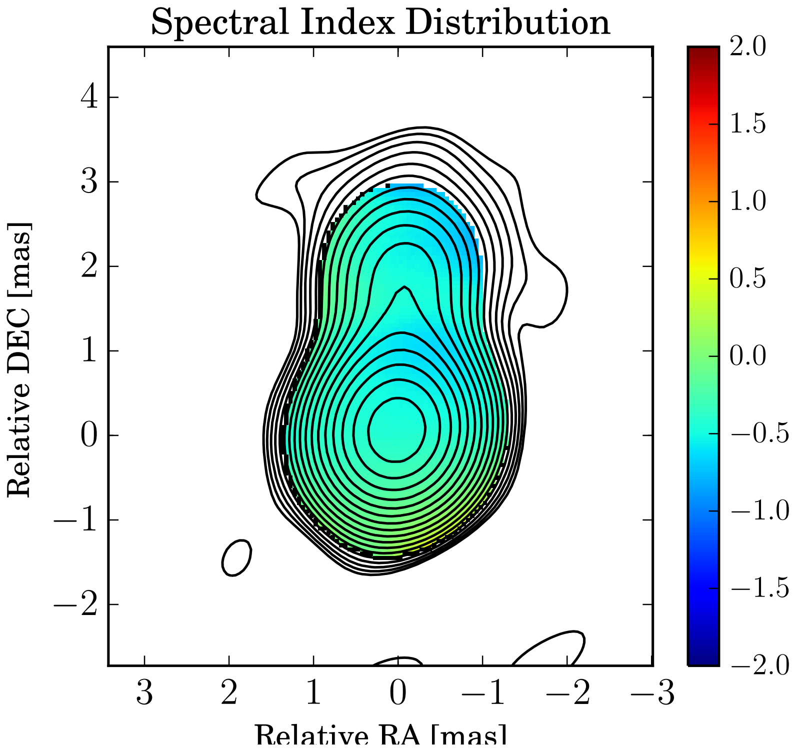

Figure 4.8. KaVA spectral index map of 4C +21.35 from May 2015 data.

4.5 Discussion

4.5.1 Boston University Program Data

In order to cross-check our 43 GHz KaVA results with VLBA data, we used archival data from the Boston University Blazar Monitoring Program (BU Program).[3] The BU Program archive provided us with eight epochs of 43 GHz maps obtained from April 2015 to April 2016. During monitoring campaigns, the BU Program gathers data on a monthly basis. VLBA has more antennas and a better *uv*-coverage than KaVA. As a result, we found more circular Gaussian jet components in the (original) VLBA images than in our KaVA maps. For a direct comparison to our data, we step by step trimmed out components from the BU Program maps: we removed peripheral components and repeated the component fitting procedure until we came up with jet component locations and sizes that are as close as possible to the KaVA data. We then continued with an analysis of the jet kinematics as we did for the KaVA data.

We found apparent jet speeds ranging from $(7.8 \pm 0.9)c$ to $(15.3 \pm 1.1)c$, with higher speeds at larger distances from the core (see Figure 4.9). These speeds are faster than the ones we obtained from our 43 GHz KaVA data by a factor of at least two. Since the observing frequencies are identical and the observations overlap in time, we suspected blending effects due to differences in angular resolution as a main cause for this discrepancy; the beam-size of VLBA at 43 GHz is 0.38×0.19 mas, half of the KaVA beam-size.

4.5.2 BU Program Data with KaVA *uv*-coverage

In order to make the *uv*-coverage of the BU Program data as similar as possible to our KaVA observations, we removed visibilities obtained at baselines longer than those of KaVA, i.e., $3 \times 10^8\lambda$ (λ being the wavelength). The resulting *uv*-coverage still shows a higher density of visibilities than the KaVA case. The beam size is 0.58×0.53 mas (July 2015 data) and the image noise rms value is $\sim$1 mJy/beam, both of which are

---

[3] `www.bu.edu/blazars/VLBAproject.html`

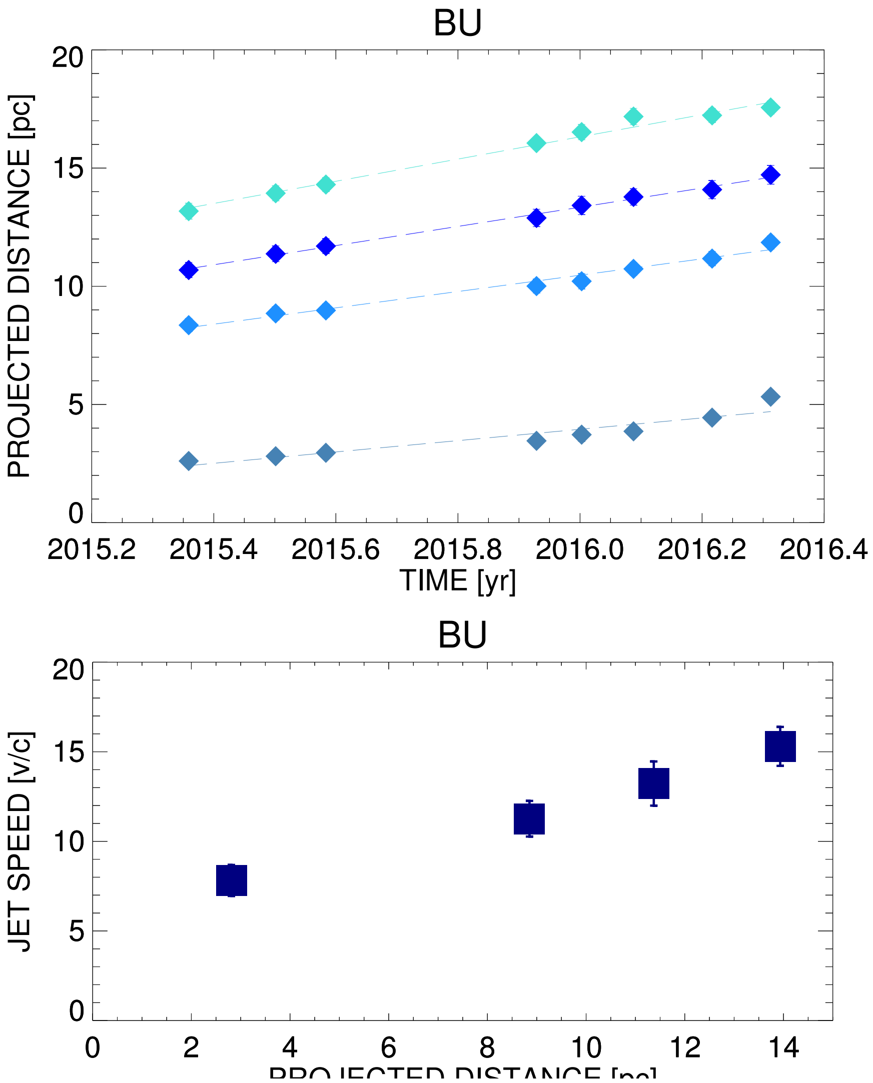

Figure 4.9. Jet kinematics derived from BU Program 43 GHz data. *Top panel:* Core distance as a function of time for four jet components. *Bottom panel:* Jet component speed as a function of core distance. Error bars represent 1σ uncertainties.

comparable to that of KaVA. In the modified images, we again identified and tracked the jet components if possible. The jet component locations are consistent with those in the KaVA maps. For the components at 3 pc and 10 pc from the core, the apparent speeds are comparable to the original BU data; at 13 pc, however, the estimated speed was $\sim 7c$. This is just about half of the speed found in the original VLBA data and close to the value for the KaVA component at 14 pc (see Figure 4.10).

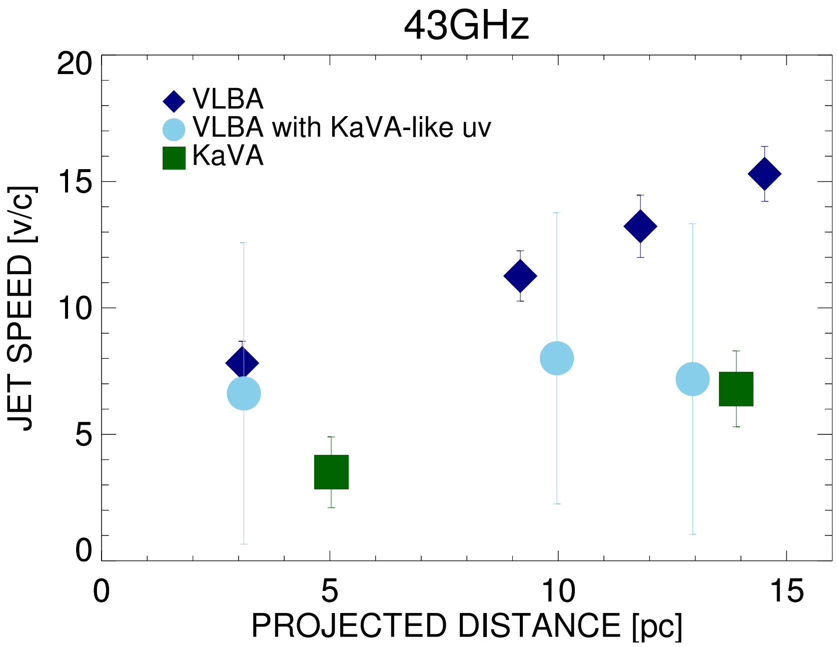

Figure 4.10. Jet component speeds as a function of core distance for three different 43 GHz datasets. Blue: VLBA; green: KaVA data; skyblue: VLBA with KaVA-like *uv* coverage. Error bars represent 1σ uncertainties.

4.5.3 MOJAVE Data

As a further cross-check, we analyzed archival 15.4 GHz VLBA data obtained by the MOJAVE program[4] and compared those to our 22 GHz KaVA data. The MOJAVE archive provided us with seven epochs of data spanning from September 2014 to September 2016.

---

[4] `www.physics.purdue.edu/MOJAVE/allsources.html`

The beam size of the MOJAVE maps, 1.01 × 0.576 mas (June 2015 data) and the map rms value, 2 mJy/beam, are about the same as that for KaVA at 22 GHz. We thus proceeded with direct comparison of the two datasets without modifying the VLBA maps. We found four jet components at 1, 3, 8, and 12 pc from the core, closer to the core than those found in the KaVA 22 GHz data. The apparent jet component speeds range from $(5.3 \pm 1.3)c$ to $(9.3 \pm 2.0)c$, comparable to the KaVA 22 GHz data (see Figure 4.11).

4.5.4 The 10-mas-blob

The 10-mas-blob continues to drift to the north-east, in agreement with the report by Homan et al. (2009). This is interesting for two reasons: (a) the 10-mas-blob has remained on a stable bent path since its ejection in the early 2000s; (b) the trajectory of the 10-mas-blob, when extrapolated, is inconsistent with that of an older blob located ∼15 mas (not shown in our maps) that shows an almost radial trajectory. Non-ballistic motion, as observed for the 10-mas-blob, is a well-known feature of blazar jets; Lister et al. (2009) and Kellermann et al. (2004) found almost one third of the blazars in their samples to show non-radial motion. Homan et al. (2009) concluded that accelerations perpendicular to the jet direction are common in blazars. They also found that, despite changes in jet direction, jet components have an overall tendency to follow the downstream flow; this was also noted by Kellermann et al. (2004) who concluded that jet flows follow pre-existing bent channels. Even so, the mechanism behind non-radial motions is not yet understood. Given that many blazars show misaligned jet orientations on parsec to kiloparsec scales (Kharb et al. 2010), it is possible that the 10-mas blob changes its course again in the future. Based on Very Large Array 1.4 GHz maps, Cooper et al. (2007) reported that the blob seems to follow the existing large-scale structure to the east.

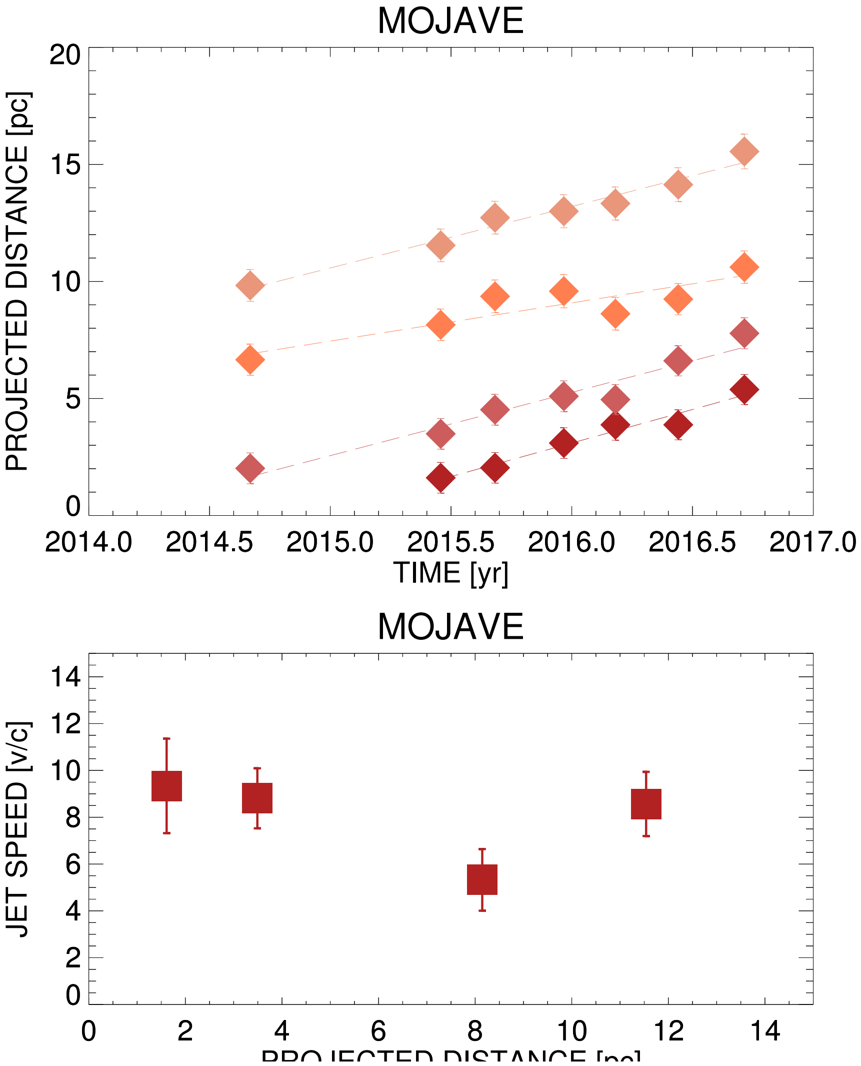

Figure 4.11. Jet kinematics derived from MOJAVE 15.4 GHz data. *Top panel:* Core distance as a function of time for four jet components. *Bottom panel:* Jet component speed as a function of core distance. The 1σ error bars are smaller than the symbols.

4.6 Conclusion

We have been able to constrain the kinematics of the jet of 4C +21.35 with KaVA observations spanning from mid-2014 to mid-2016. Our results demonstrate the ability of KaVA to provide important information on AGN jet kinematics in the frame of focused observing campaigns, in line with several recent works (Niinuma et al. 2014; Oh et al. 2015; Hada et al. 2017). Exploiting the dense (bi-weekly) sampling of our data, we were able to identify and track jet components from epoch to epoch with high reliability. Due to the timing of our observations, we were able to find a connection between the γ-ray flare of 2014 and the jet kinematics. Furthermore, we were able to accurately trace the exponential flux decay for the inner jet components, especially for the newly ejected jet component C at 22 GHz.

Our maps resolve several components within the northward-pointing jet. At 22 GHz (Section 4.4.1), we identify five components in total, three of them in the continuous inner jet within 4 mas from the core. Notably, a new component emerged in early 2016. This new component moved along the straight path of the other two inner jet components; the apparent speeds of the three components are $(6.3^{+11.9}_{-6.3})c$, $(10.8 \pm 1.4)c$, and $(14.4 \pm 2.1)c$ (outward from the core) and are in good agreement with those obtained from MOJAVE 15.4 GHz data (about $8c$).

At 43 GHz (Section 4.4.2), we have been able to resolve the (inner) jet into four components out which we could re-identify (from epoch to epoch) and track two reliably. Even though all the jet components appear to move straight to the north, the jet appears somewhat bent (with a tilt of about 20 deg to the west) within the innermost $\lesssim$0.5 mas. Indeed, the innermost jet component, located about 0.3 mas away from the core, seems to mark the approximate location where the jet flow turns straight north (see Figure 4.4).

The apparent KaVA jet component speeds at 43 GHz are $(3.5 \pm 1.4)c$ and $(6.8 \pm 1.5)c$ at 5 and 14 pc, respectively. However, a kinematic analysis of the contemporaneous BU Program 43 GHz (Section 4.5.1) data finds speeds ranging from $(7.8 \pm 0.9)c$ to $(13.2 \pm 1.2)c$. Likewise, Troitskiy et al. (2016) reported speeds of $9c$ to $22c$ for five jet components located within $\lesssim$5 pc using BU Program data obtained from 2010 to 2016. We suspect an effect of angular resolution: the beam-size of the BU Program data, 0.38 mas $\times$ 0.19 mas, is about half of that of KaVA at 43 GHz, 0.72 mas $\times$ 0.63 mas. Our test analysis of BU Program data with KaVA-like *uv*-coverage (Section 4.5.2) supports this conclusion: it found a substantial drop of the apparent jet speed compared to the one derived from the original VLBA maps; this "loss of speed" increases with increasing core distance and reaches up to about 50%. The "loss of speed" effect is, arguably, a consequence of the well known fact that, physically, an AGN jet is not a group of discrete point-like sources but a complex continuous distribution of matter. Observations with different *uv*-coverages will beam-average different regions of a jet which may lead to systematic differences in component positions as function of time. Indeed, it seems somewhat unsettling that the observed kinematics may depend on the instrument used for observations.

Another potential mechanism leading to a "loss of speed" effect is *time* resolution: observations obtained at discrete epochs may not reliably re-identify jet components from epoch to epoch. Piner et al. (2007) noted that temporal undersampling often results in misidentification of components and under- or overestimation of apparent jet speeds. Notably, the high cadence of KaVA observations – every two weeks since early 2016 – reduces the risk of time resolution effects distorting kinematic analyses. In the case of 4C +21.35, proper motions of jet components are below 1 mas yr^{-1}, corresponding to about 40 μas per two weeks and thus making a confusion of components is unlikely.

In Section 4.4.4, we found $1/e$ flux decay time scales for the KaVA jet components ranging from $\sim$ 0.5 years to $\sim$ 3 years. Equating this time scale with the synchrotron cooling time provided us with the estimated magnetic field strengths of about 1 to 3 μT. We used an electron Lorentz factor $\gamma \sim 9\,000$, a value located at the upper end of the interval covered by values typical for FSRQ (Ghisellini et al. 2002). The magnetic field strengths we find are consistent with the values typical for blazars which are in the range from 1 to 10 μT (Lewis et al. 2016). Pushkarev et al. (2012) independently calculated the magnetic field strengths at the core and at 1 pc downstream from the jet vertex using the core shift effect, finding 4 μT and 90 μT, respectively – which is consistent with our findings.

We detected a new 22 GHz jet component in early 2016. Assuming a constant speed and extrapolating its motion back to zero distance from the core suggests that it was ejected at the end of October 2014. Although this estimated ejection time has relatively large uncertainties, it's in agreement with the time of the mid-November 2014 Fermi-LAT γ-ray flare. This is consistent with the very high energy emitting region being located close to the broad line region (thus avoiding absorption by BLR clouds) as well as a small size of the VHE emitter (as already expected from γ-ray / VHE variability) (Kushwaha et al. 2014; Tavecchio et al. 2011). Aleksic et al. (2014) also came to the same conclusion from the MAGIC observation of a FSRQ, PKS 1510-089. Likewise, Ackermann et al. (2014) constructed a SED with a one-zone model that assumes a very compact emission region outside the BLR.

Overall, our KaVA observations of 4C +21.35 strengthen the case for a causal connection between the occurrence of γ-ray flares and the ejection of new jet components in blazars. This merits additional radio-interferometric studies of VHE AGN in order to probe this suspected connection in depth. Our analysis, however, clearly shows the importance of high cadence observations in order to avoid misunderstanding the jet kinematics.

Chapter 5

Conclusion

In this thesis, we presented the time-series analysis, related kinematics, and gamma-ray relations of bright nearby blazars using various projects and archival data.

In the first chapter, we investigated AGN intra-day variability using single-dish observations with KVN. We achieved a time resolution of less than three minutes at all four KVN frequencies of 22, 43, 86, and 129 GHz. The high-quality lightcurves are constructed for 3C 111, 3C 454.3, and BL Lacertae at 22 and 43 GHz, and for 3C 279 at 86 GHz, between May 2012 and April 2013. On time scales from minutes to hours, the source fluxes did not change more than a few percent, the light curves appear to be mostly flat. We found the flux variability modulation index ranging from $\sim 1.6\%$ to $\sim 7.6\%$. In our case, our relatively large m values are caused mostly by the photometric uncertainties. The lightcurves are characterized by scatter rather than systematic deviations from the mean, as expected for the case of source intrinsic variability. Our χ_r^2 tests find values ranging from 0.6 to 1.8, which indicates no variation in our lightcurves.

Even so, we were able to put upper limits on brightness temperatures. The resulting upper limits range from 10^{13} to 10^{18} K and exceed the Inverse Compton limit (10^{12} K) as well as the equipartition limit (3×10^{11} K) by two to six orders of magnitude. From our results, we conclude that we have not detected source-intrinsic variability which would have to occur at sub-percent levels.

In the following chapter, we showed the results of the monthly monitoring of a BL Lac object, PKS 1749+096. We investigated the temporal variability spanning 1.5 years observed with KVN at four frequencies of 22, 43, 86 and 94 GHz quasi-simultaneously. The four ligntcurves from four KVN frequencies and three lightcurves by ALMA band 3, 6, 7 all show concurrent radio flares with the characteristic variability time scale of 1.4 yrs. The spectral indices indicate the optically thin radio core of the source except at 22 GHz where it was mostly optically thick with $a \sim 0$. PKS 1749+096 experienced a prominent gamma-ray outburst in the middle of 2016 and had few follow-up flares. By studying the correlation between the ALMA band 3 and Fermi-LAT lightcurves, we found that the radio flare peaking at 2019.25 and the gamma-ray flare between the end of 2017 and the beginning of 2018 are correlated and the estimated time lag was 1.26 years with the gamma-ray leading the radio flare.

From the VLBA 43 GHz archival data covering the same observation period, we could identify and track four jet components and estimate apparent jet speeds as 4, 4.8, 5.8, and 9.7 c. Also, there was a stationary component detected hovering within 2 mas close to the core. Extrapolating the radial distance of a jet component indicates an interaction with the stationary component at the time of gamma-ray flare at the end of 2017. The outward movement of the stationary component also supports the interaction scenario. Consequently, we suggest that a shock or disturbance propagating through the mm-VLBI core is responsible for the gamma-flare at the end of 2017 to the beginning of 2018.

We also probed the physical information of synchrotron self-absorption region during the flaring activity. From the radio flare rising timescale, we derived the variability brightness temperature, 4.7×10^{10} K, the variability Doppler factor, 0.35, and the emission region size, 0.024 mas. Associated magnetic field strength of 0.11 G was obtained assuming synchrotron cooling of the region.

In Chapter 4, we presented the result of intense KaVA monitoring program. We were able to constrain the jet kinematics of the FSRQ 4C +21.35 spanning from mid-2014 to mid-2016. Observations were performed bi-weekly at 22 and 43 GHz quasi-simultaneously. At 22 GHz, we identified three jet components near the core with apparent speeds ranging from 6.3 to 14.4 *c*. From the extrapolating the position of a newly detected jet component, the ejection time was estimated and coincided with the gamma-ray flare in November 2014. Thus, a diturbance moving through the radio core is suspected to have triggered the gamma-ray flare.

At 43 GHz, we found four inner jet (<3 mas) components with apparent speeds from 3.5 to 6.8 *c*. The estimated jet component speeds are higher with increasing distances from the core. We compared our data with archival VLBA 43 GHz data and the MOJAVE 15.4 GHz data. Whereas MOJAVE data and our data are in good agreement, jet speeds obtained from the BU data in the same time period are about twice as high as the ones we obtained from the KaVA data. The discrepancy at 43 GHz indicates that radio arrays with different angular resolution may beam-average different regions of a jet which may lead to systematic differences in component positions as function of time.

The jet components show exponential decay of flux densities, estimated synchrotron cooling time scale is ∼1 year. Using the known electron Lorentz factor (∼9,000), we estimated the magnetic field strength to be ∼1–3 μT. With a viewing angle of 5°, the estimated intrinsic jet speed is of order $0.99c$.

In summary, we probed the AGN jet properties in parsec scale by dense regular observations. From the studies of multi-wavelength lightcurves, kinematics, and high energy correlations, we could extend our understanding of the jet propagation, acceleration, interaction, and emission processes.

Bibliography

ABdo, A., Ackermann, M., Ajello, M., et al. 2009, ApJ, 699, 31

Abdollahi, S., Acero, F., Ackermann, M. et al. 2020, ApJS, 247, 33

Abramowicz, M. A., Bao, G., Lanza, A., & Zhang, X.-H. 1991, A& A, 245, 454

Ackermann, M., Ajello, M., Allafort, A., et al. 2011, ApJ, 741, 30

Ackermann, M., Ajello, M., Allafort, A., et al. 2014, ApJ, 786, 157

Aharonian, F. A. 2000, New Astronomy, 5, 377

Ajello, M., Atwood, W. B., Baldini, L., et al. 2017, ApJS, 232, 18

Aleksic, J., Antonelli, L. A., Antoranz, P., et al. 2011, ApJ, 730, L8

Aleksic, J., Ansoldi, S., Antonelli, L. A., et al. 2014, A& A, 569, A46

Algaba, J.-C., Lee, S., Kim, D., et al. 2018a, ApJ, 852, 30

Algaba, J.-C., Lee, S., Rani, B., et al. 2018b, ApJ, 859, 128

An, T., Cui, Y., Paragi, Z., et al. 2016, PASJ, 68, 77

Armandroff, T. E. & Da Costa, G. S. 1986, AJ, 92, 777

Arshakian, T. G., León-Tavares, J., Lobanov, A.P. 2010, MNRAS, 401, 1231

Asada, K. & Nakamura, M. 2021, ApJ, 745, L28

Atwood, W. B., Abdo, A. A., Ackermann, M., et al. 2009, ApJ, 697, 1071

Barthel, P. D. 1989, ApJ, 336, 606

Beckmann, V. & Shrader, C. 2012, Active Galactic Nuclei (Weinheim: Wiley VCH)

Benlloch, S., Wilms, J., Edelson, R., Yaqoob, T., & Staubert, R. 2001, ApJ, 562, L121

Bessell, M. S. 1979, Publications of the Astronomical Society of the Pacific, 91, 589.

Blandford, R. D., & Königl, A. 1979, ApJ, 232, 34

Blandford, R. D. & Payne, D. G. 1982, MNRAS, 199, 883

Blandford, R. D. & Znajek, R. L. 1977, MNRAS, 179, 433

Boccardi, B., Krichbaum, T. P., Bach, U., et al 2016, A& A, 585, A33

Boettcher, M., Harris, D. E., & Krawczynski, H. 2012, Relativistic Jets from Active Galactic Nuclei (Weinheim: Wiley-VCH)

Boettcher, M. & Els, P. 2016, ApJ, 821, 102

Cerruti, M., Lenain, J.P., & Prokoph, H. 2017, Proceedings of Science `[arXiv:1708.00658]`

Chidiac, C., Rani, B., Krichbaum, T. P., et al. 2016, A& A, 590, 61

Cho, I., Jung, T., Zhao, G., et al. 2017, PASJ, 69, 87

Connolly, S. D. 2015, arXiv:1503.06676

Cooper, N. J., Lister, M. L., & Kochanczyk, M. D., 2007, ApJS, 171, 376

Costamante, L., Cutini, S., Tosti, G., et al. 2018, MNRAS, 477, 4749

Das, A., Prince, R. & Gupta, N. 2021, ApJ, 920, 117

Davis, S. W., & Tchekhovskoy, A. 2020, ARA& A, 58, 407

Dermer, C. D. & Schlickeiser, R. 1993, ApJ, 416, 458

Edelson, R. A., & Krolik, J. H. 1988, ApJ, 333, 646

Emmanoulopoulos, D., McHardy, I. M., & Papadakis, I. E. 2013, MNRAS, 433, 907

Fanaroff, B. L., & Riley, J. M. 1974, MNRAS, 167, 31

Fomalont, E. B., 1999, in ASP Conf. Ser. 180, Synthesis Imaging in Radio Astronomy II, ed. G. B. Taylor, C. L. Carilli, & R. A. Perley (San Francisco, CA: ASP), 301

Fossati, G., Maraschi, L., Celotti, A., et al. 1998, MNRAS, 299, 433

Fragile, P. C. 2008, Proceedings of Science, `[PoS(MQW7)039]`

Fuhrmann, L., Krichbaum, T.P., Witzel, A., et al. 2008, A&A, 490, 1019

Fuhrmann, L., Larsson, S., Chiang, J., et al. 2014, MNRAS, 441, 1899

Ghisellini, G., Celotti, A., & Costamante, L., 2002, A& A, 386, 833

Ghisellini, G., Tavecchio, F., Foschini, L., et al. 2011, MNRAS, 414, 2674

Ghisellini, G., Tavecchio, F., Maraschi, L., et al. 2014, Nature, 515, 376

Ghisellini, G., Righi, C., Costamante, L., et al. 2017, MNRAS, 469, 255

Giommi, P., Padovani, P., Polenta, G., et al. 2012, MNRAS, 420, 2899

Gupta, A. C., Krichbaum, T. P., Wiita, P. J., et al. 2012, MNRAS, 425, 1357

Hada, K., Park, J. H., Kino, M., et al. 2017, PASJ, 69, 71

Hada, K., Niinuma, K., Sitarek, J., et al. 2020, ApJ, 901, 2

Hargreaves, J. C., Gilmore, G., Irwin, M. J., & Carter, D. 1994, MNRAS, 269, 957

Hervet, O., Boisson, C., & Sol, H. 2016, A& A, 592, A22

Högbom, J. A. 1974, Astronomy and Astrophysics Supplement Series, 15, 417

Homan, D. C., Kadler, M., Kellermann, K. I., et al. 2009, ApJ, 706, 1253

Homan, D. C., Ojha, R., Wardle, J. F. C., et al. 2001, ApJ, 549, 840

Homan, D. C., Ojha, R., Wardle, J. F. C., et al. 2002, ApJ, 568, 99

Hovatta, T., Valtaoja, E., Tornikoski, M., et al. 2009, A& A, 494, 527

Jorstad, S., Marscher, A., Mattox, J., et al. 2001a, ApJS, 134, 181

Jorstad, S., Marscher, A., Mattox, J., et al. 2001b, ApJ, 556, 738

Jorstad, S., Marscher, A., Larionov, V. M., et al. 2010, ApJ, 715, 362

Jorstad, S. G., Marscher, A. P., Lister, M. L., et al. 2005, AJ, 130, 1418

Jorstad, S., Marscher, A., Smith, P., et al. 2013, ApJ, 773, 147

Jorstad, S. G., Marscher, A. P., Morozova, D. A., et al. 2014, Proc. IAU Symposium 313

Jorstad, S. G., Marscher, A. P., Morozova, D. A., et al. 2017, ApJ, 846, 98

Kataoka, J. & Stawarz, L. 2005, ApJ, 622, 797

Karamanavis, V., Fuhrmann, L., Angelakis, E., et al. 2016a, A& A, 590, 48

Karamanavis, V., Fuhrmann, L., Krichbaum, T. P., et al. 2016b, A& A, 586, A60

Kellermann, K. I. & Pauliny-Toth, I. I. K. 1969, ApJ, 155, L71

Kellermann, K. I., Sramek, R., Schmidt, M., et al. 1989, AJ, 98, 1195

Kellermann, K. I., Lister, M. L., Homan, D. C. et al. 2004, ApJ, 609, 539

Kharb, P., Lister, M. L., & Cooper, N. J. 2010, ApJ, 710, 764

Kim, K.-T., Byun, D.-Y., Je, D. H., et al. 2011, JKAS, 44, 81

Kim, J.-Y. & Trippe, S. 2013, JKAS, 46, 65

Kim, J. & Trippe, S. 2014, JKAS, 47, 195

Kim, D., Trippe, S., Lee, S., et al. 2018, MNRAS, 480, 2324

Kino, M., Wajima, K., Kawakatu, N., et al. 2018, ApJ, 864,118

Komissarov, S. S., Barkov, M. V., Vlahakis, N., et al. 2007, MNRAS380, 51

Komissarov, S. S. & Barkov, M. V. 2009, MNRAS, 397, 1153

Kravchenko, E., Gomez, J., Kovalev, Y., et al. 2020, ApJ, 893, 68

Kushwaha, P., Sahayanathan, S., Lekshimi, R., et al. 2014, MNRAS, 442, 131

Kraus, A., Krichbaum, T. P., Witzel, A., et al. 2003, A&A 401, 161

Lee, S.-S., Byun, D.-Y., Oh, C. S., et al. 2011, PASP, 123, 1398

Lee, S.-S., Oh, C. S., Roh, D., et al. 2015, JKAS, 48, 125

Lee, T., Trippe, S., Kino, M., et. al. 2019, MNRAS, 486, 2412

Lewis, T. R., Becker, P. A., & Finke, J. D. 2016, ApJ, 824, 108

Lico, R., Giroletti1, M., Orienti, M., et al. 2014, A& A, 571, 54

Liodakis, I., Romani, R., Filippenko, A., et al. 2018, MNRAS, 480, 5517

Lisakov, M. M., Kovalev, Y. Y., Savolainen, T., et al. 2017, MNRAS, 468, 4478

Lister, M. L., Cohen, M. H., Homan, D. C., et al. 2009, AJ, 138, 1874

Lister, M. L., Aller, M.F., Aller, H. D., et al. 2013, AJ, 146, 120

Lister, M. L., Aller, M. F., Homan, D. C., et al. 2016, AJ, 152, 12

Lister, M., Homan, D., Hovatta, T., et al. 2019, ApJ, 874, 43

Lovell, J. E. J., Rickett, B. J., Macquart, J.-P., et al. 2008, ApJ, 689, 108

Lu, R., Shen, Z., Kirchbaum, T., et al. 2012, A& A, 544, A89

Mahmoud, S. M., Ensor, A., Biem, A., et al. 2011, Studies in Computational Intelligence, 426

Maraschi, L., Ghisellini, G. & Celotti, A. 1992, ApJ, 397, L5

Marscher, A., 1983, ApJ, 264, 296

Marscher, A. P. 2006, in American Institute of Physics Conference Series, Vol. 856, Relativistic Jets: The Common Physics of AGN, Microquasars, and Gamma-Ray Bursts, ed. P. A. Hughes & J. N. Bregman, 1–22

Marscher, A. P., & Gear, W. K. 1985, ApJ, 298, 114

Marscher, A., Jorstad, S., Larionov, V. M., et al. 2010, ApJ, 710, 126

Marscher, A., Jorstad, S., D'Arcangelo, F., et al. 2008, Nature, 452, 966

Max-Moerbeck, W., Hovatta, T., Richards, J., et al. 2014, MNRAS, 445, 428

Mertens, F., Lobanov, A. P., Walker, R. C., et al. 2016, A& A, 595, A54

Meyer, T. E., Fossati, G., Georganopoulos, et al. 2011, ApJ, 740, 98

Meyer, M., Scargle, J., & Blandford, R. 2019, ApJ, 877, 39

Mizuno, Y., Hardee, P., & Nishikawa, K.-I. 2007, ApJ, 662, 835

Nakamura, M., Asada, K., Hada, K., et al. 2018, ApJ, 868, 146

Nalewajko, K., Begelman, M. C., & Sikora, M. 2014, ApJ, 789,161

Niinuma, K., Lee, S., Kino, M., et al. 2014, PASJ, 2014, 66, 103

Oh, J., Trippe, S., Kang, S., et al. 2015, JKAS, 48, 299

Orienti, M., Koyama, S., D'Ammando, F., et al. 2013, MNRAS, 428, 2418

O'Sullivan, S. & Gabuzda, D. 2009, MNRAS, 393, 429

Pacholczyk, A. G. 1970, Radio astrophysics. Nonthermal processes in galactic and extragalactic sources, Series of Books in Astronomy and Astrophysics (San Francisco, CA: Freeman)

Park, J.-H. & Trippe, S. 2012, JKAS, 45, 147

Park, J.-H. & Trippe, S. 2014, ApJ, 785, 76

Petropoulou, M., & Dimitrakoudis, S. 2015, MNRAS, 452, 1303

Piner, B. G., Mahmud, M., Fey, A. L., et al. 2007, AJ, 133, 2357

Pushkarev, A. B. 2001, Astron. Rep., 45, 667

Pushkarev A. B., Kovalev Y. Y., Lister M. L. 2010, ApJ, 722, L7

Pushkarev, A.B., Hovatta, T., Kovalev, Y. Y., et al. 2012, A& A 545, A113

Pushkarev, A. B., Kovalev, Y. Y., Savolainen, T., et al. 2017, MNRAS, 468, 4992

Rani, B., Krichbaum, T. P., Fuhrmann, L., et al. 2013, A& A, 552, A11

Readhead, A. C. S. 1994, ApJ, 426, 51

Rickett, B. J. 1990, ARAA, 28, 561

Rybicki, G. B. & Lightman, A. P. 1979, Radiative Processes in Astrophysics (Weinheim: Wiley-VCH)

Scargle, J. D. 1982, ApJ, 263, 835

Sbarrato, T., Padovani, P., & Ghisellini, G. 2014, MNRAS, 445, 81

Shepherd, M. C., Pearson, T. J., & Taylor, G. B. 1994, BAAS, 26, 987S

Sikora M., Begelman M. C., Rees M. J. 1994, ApJ, 421, 153

Sikora M., Begelman, M. C., Madejski, G. M., et al. 2005, ApJ, 625, 72

Sikora M., Stawarz, Ł., Moderski, R., et al. 2009, ApJ, 704, 38

Sol, H., Pelletier, G., Asseo, E. 1989, MNRAS, 237, 411

Stickel, M., Fried, J. W., Kuhr, H. 1988, A& A, 191, 16.

Tavecchio, F., Becerra-Gonzalez, J., Ghisellini, G., et al. 2011, A&A, 534, A86

Trippe, S., Krips, M., Piétu, V., et al. 2011, A&A, 533, A97

Troitskiy, I., Morozova, D., Jorstad, S., et al. 2016, Galaxies, 4, 72

Uemura, M., Itoh, R., Liodakis, I., et al. 2017, PASJ, 69, 6

Urry, C. M. & Padovani, P., 1995, PASP, 107, 803

Vlahakis, N. Theory of Relativistic Jets. In The Formation and Disruption of Black Hole Jets (eds. Contopoulos, I., Gabuzda, D., & Kylafis, N.) 177-206 (Astrophys. Space Sci. Libr. Vol. 414, Springer, 2015).

Wagner, S. J., & Witzel, A. 1995, ARAA, 33, 163

Wajima, K., Fujisawa, K., Hayashida, M. et al. 2014, ApJ, 781, 75

Wang, J., Luo, B., and Ho, L., 2004, ApJ, 615, L9

Weaver, Z., Jorstad, S., Marscher, A., et al. 2022, `[arXiv:2202.12290v1]`

Wehrle, A., Marscher, A., Jorstad, S., et al. 2012, ApJ, 758, 72

Witzel, A., Heeschen, D.S., Schalinski, C., & Krichbaum, T.P. 1986, Mitt. Astron. Ges., 65, 239

Xiong, D., Zhang, X., Bai, J., et al. 2015, MNRAS, 451, 2750

Yeom, J., Oh, S., Roh, D., et al. 2009, Journal of Astronomy and Space Sciences, 26, 567

Zhang, Y., An, T., Frey, S., et al. 2017, MNRAS, 468, 69

요약

활동성 은하핵은 정말 놀라운 천체이다. 이 천체는 가장 강력하고 밝으며 지속적인 에너지원이고 메가파섹 거리까지 뻗어나가는 제트구조를 보인다. 중심부에는 제트의 에너지원으로 추정되는 초거대블랙홀이 존재하는 것으로 알려져 있다.

활동석 은하핵의 강한 제트는 도플러 효과에 의해 겉보기 초광속 운동을 하는 것처럼 보이고, 에너지의 대부분을 싱크로트론 복사와 inverse Compton 복사의 형태로 방출한다. 제트의 형성과 collimation 및 가속에 대한 연구는 많이 이루어졌으나, 아직도 많은 중요한 질문들이 남아 있다. 활동성 은하핵의 특징들을 연구하는 방법론으로는 시간에 따른 밝기 변화 연구, 운동학 연구, 편광 연구, 다중 파장 활용 연구 등이 있고 많은 경우에 여러 방법들을 동시에 사용한다.

먼저, 활동석 은하핵은 불규칙적인 밝기 변화를 보이는데 그 변화 시간 규모는 작게는 하루 이내 규모에서부터 시작하기도 하며 분에서 시간에 이르는 시간단위 안에서 몇 퍼센트씩 변화하하기도 한다. 그러한 작은 시간 규모에서 아직도 밝혀지지 않은 영역이 존재한다.

본 논문의 첫 장에서는, KVN 단일경 관측으로 실시했던 ‘신속 광도 측정 결과’를 다룬다. 두 개의 안테나에서 반-상관관계를 이루게 설정한 관측 모드를 활용하여서, calibrator를 관측해야 할 때에도 언제나 한 안테나는 목표 천체를 바라보게 하였다. 그 결과 3분 미만의 짧은 시간 해상도를 얻을 수 있었고 spectral 변화를 보기위하여 KVN 에서 관측 가능한 네 개의 파장대인 22, 43, 86, 129 GHz 를 모두 사용하였다.

그 결과, 2013년 4월부터 2012년 5월에 이르는 기간동안 22, 43, 86 GHz에서 3C 111, 3C 454.3, 그리고 BL Lacertae의 고퀄리티 광도곡선을, 86 GHz에서 3C 279의 광도곡선을 얻을 수 있었다. 목표 천체들의 광도 변화 수준과 그에 따른 상방 한계를 구해내기 위하여 자세한 통계 분석을 실시하였으며, 밝기 변화 수치는 약 1.6%에서 약 7.6%에 이른다는 것을 알아냈다.

측정된 밝기온도에 대한 상방 한계는 inverse Compton 한계를 천 배에서 백만 배 정도 넘는 것으로 판명되었다. 본 연구 데이터와 미시건 전파천문학 관측소 (UMRAO)에서 얻은 데이터와의 비교를 통하여, 우리는 목표 천체에서 나오는 의미있는 정도의 밝기변화를

관측하지 못하였다고 결론내렸다.

둘째로, PAGaN (Plasma-physics of Active Galactic Nuclei) 프로젝트의 일환으로 BL Lac 천체중 하나인 1749+096에 대해 2018년 2월부터 2019년 6월까지 1년 반동안 KVN VLBI 관측을 수행하였다. 그 결과, KVN 의 네 개 주파수 영역인 22, 43, 86, 94 GHz 와 ALMA 의 세 개 주파수 영역인 band 3, 6, 7 에 이르기까지 모든 전파영역에서 광도곡선이 동시적 flare 현상을 보이고 있음을 확인하였으며 특징적 시간 규모는 1.4년임을 측정하였다. 목표 천체인 1749+096은 2016년 중반에 전례없는 강한 감마선 폭발현상을 보였으며 그 이후로도 몇 번의 감마선 밝기증가현상을 보였다. 2017년 봄에서부터 2021년 초 까지의 ALMA band 3 에서의 광도변화와 Fermi-LAT 광도곡선을 상관 관계 분석한 결과, 감마선 flare 현상이 전파 flare 현상은 1.26년 더 앞섰다는 것을 발견했다. 기록 보관소에서 얻은 VLBA 43 GHz 관측 데이터에서는 북북동쪽으로 표출되어있는 작은 제트를 확인할 수 있었다. 천체의 코어와 정지해있는 component를 포함하여 모두 여섯 개의 제트 component 를 확인하고 추적할 수 있었으며, 네 개 제트 component의 겉보기 속도가 4, 4.8, 5.8, 그리고 9.7 c로 측정되었다. VLBA 이미지를 이용한 운동학 분석결과, 제트 component가 코어에서 가까운 정지 component와 상호반응했을 시점이 감마선 flare가 나타났던 시점과 일치한다는 것을 확인하였다. 그리하여, 감마선의 발생지역이 mm-코어 부근이라는 것을 확인하였다.

이에 더하여, flare 현상 중 싱크로트론 자기흡수 지역에서의 물리적 정보를 도출하였다. 전파 flare 상승 시간규모 1.4년을 이용하여, 광도변화적 밝기온도를 $4.7 \times 10^{10} K$으로 측정하였고 광도변화적 도플러 상수 0.35를 도출하였다. 또한 전파에너지 방출지역의 겉보기 크기를 0.024 밀리각초로 도출하였고 지역적 싱크로트론 냉각을 가정한다면 관련된 자기장의 세기는 0.11 G로 측정되었다.

마지막으로는, FSRQ 천체인 4C +21.35에 대한 운동학 연구를 수행하였다. 한일 전파 간섭계의 (KVN과 VERA) 공동 집합체인 KaVA 로 간섭계 관측이 이루어졌고 2014년 9월부터 2016년 7월까지 데이터를 얻을 수 있었다. 전체 관측의 66%는 격주라는 짧은 기간마다 22, 43 GHz 에서 거의 동시 관측을 실시할 수 있었다.

22 GHz 에서는 코어에 가까운 곳에서 세 개의 제트 component를 확인 및 추적할 수

있었는데 그 겉보기 속도는 6.3에서 14.4c까지 분포하고 있었다. 2016년에 관측된 새로운 제트 component는 그 위치를 추적한 결과, 코어에서 방출된 시간이 2014년 11월의 감마선 flare 시간과 일치하는 것을 확인하였다. 43 GHz 에서는 네 개의 제트 component를 확인하였고 그 속도는 3.5에서 6.8c까지 분포하는데 코어에서 멀어질 수록 속도가 빨라지는 경향이 있었다. 같은 43 GHz 에서 행해지는 보스턴 대학의 VLBA 기록보관소 데이터와 15.4 GHz 에서 행해지는 MOJAVE 추적프로그램의 기록보관소 데이터도 입수, 분석할 수 있었다. MOJAVE 데이터는 KaVA 데이터 분석결과와 잘 부합하는 반면에, 보스턴 대학의 데이터에서 얻은 제트 속도는, 같은 기간에 속했음에도 불구하고, KaVA 데이터에서 얻은 속도보다 두 배 정도 빠른 것으로 나타났다. 43 GHz 에서의 이런 차이가 의미하는 바는, 다른 각분해능을 가진 전파 간섭계는 같은 기간 같은 주파수에서 관측을 하더라도 서로 다른 제트 형상을 확인하고 추적할 수 있다는 것이다. 한편, 제트 component 들의 밝기 밀도는 기하급수적으로 줄어들었으며 싱크로트론 냉각 시간규모는 거의 1년에 가까웠다. 알려진 전자 로렌츠 인자 값 9000을 이용하여 얻은 자기장의 세기는 $\sim$1–3 μ T에 이른다. 제트와 시선방향간의 각도 차이를 5° 로 취하면, 제트의 고유 속도는 0.99c 수준이다.

정리하면, 우리는 밀도높은 정기 관측을 수행하여 파섹 스케일에서의 활동성 은하핵 제트에 대해 연구하였다. 이 강력하고 지속적인 제트에 대한 주요 핵심 질문들은 여전히 존재하지만, 다파장 밝기변화 분석과 운동학 및 고에너지 상관관계 분석 연구를 통해 제트의 전파, 상호작용, 그리고 에너지 방출 과정 등에 대한 이해를 한층 높일 수 있었다.

주요어: galaxies: active – galaxies: jets – radio continuum: galaxies – individual: 4C +21.35, PKS 1749+096 – techniques: interferometric

학 번: 2012-20399

감사의 글

How can you not be romantic about astronomy.

2022년 7월
이태석